Delivery and safety of gold nanorods for photothermal restoration of vision in blindness

by

Hafithe M. AlGhosain حافظ محمد آل غصين

B.S.E, University of Hartford, 2017

M.Sc., Brown University, 2019

A dissertation submitted in partial fulfillment of the requirements for the degree of Doctor of Philosophy in the Biomedical Engineering program, a joint program in the Division of Biology and Medicine and the School of Engineering at Brown University

Providence, Rhode Island

October 2025

The dissertation by Hafithe M. AlGhosain is accepted in its present form by the Biomedical Engineering program, as satisfying the dissertation requirements for the degree of Doctor of Philosophy.

Date_____ _____

Jonghwan Lee, Ph.D., Advisor

Recommended to the Graduate Council

Date_____ _____

Eric Darling, Ph.D., Reader

Date_____ _____

Kareen Coulombe, Ph.D., Reader

Date_____ _____

Tao Liu, Ph.D., Reader

Approved by the Graduate Council

Date_____ _____

Janet A. Blume, Ph.D., Interim Dean of the Graduate School

CURRICULUM VITAE

Hafithe M. AlGhosain | alghosain@brown.edu

Education

Doctor of Philosophy, Ph.D., Biomedical Engineering *October 2025*

Brown University, Providence, Rhode Island

Master of Science, M.Sc., Biomedical Engineering *May 2019*

Brown University, Providence, Rhode Island

Bachelor of Science in Engineering, B.S.E *May 2017*

University of Hartford, Hartford, Connecticut

Publications

1. **AlGhosain H,** Nie J, Liu T, Lee J. *Systemic toxicity of intravitreally injected gold nanorods in mice: Effects of size, surface conjugation, and post-injection period* Toxicological Research, 2025
2. Nie J, Eom K, **AlGhosain H**, Neifert A, et al. *Intravitreally injected plasmonic nanorods activate bipolar cells with patterned near-infrared laser projection* ACS Nano, 2025

Presentations

1. **AlGhosain H**, Nie J, Lee J. *Intravitreal Delivery of Gold Nanorods to the Retina for Plasmonic Retinal Prosthetics*, ARVO 2023

Research Experience

Graduate Fellow

Department of Biomedical Engineering, *Brown University,* September 2017-October 2025

- Lead research on targeted delivery of gold nanoparticles to retinal ganglion cells and bipolar cells in the rodent retina

- Developed, tested, and established novel delivery mechanisms for drug delivery in the retina
- Pioneered a novel method to cross-reference cellular layer information by correlating confocal imaging data with two-photon microscopy data from fluorescently and non-fluorescently tagged retinae using AuNRs
- Designed an *in-vivo* toxicity experiment in accordance with ISO10993-11 standards and FDA class II regulatory guidelines
- Led one of the first *in*-vivo studies investigating systemic toxicity following IVT injection of gold nanorods challenging assumptions of ocular compartmentalization and addressing a critical blind spot in nanomedicine safety literature

Undergraduate Researcher

University of Hartford, College of Engineering, Technology and Architecture, September 2015 – May 2017

- Determined the viability of Tilapia fish-skin as a biomaterial skin analog and treatment for burn victims
- Microscopically analyzed particle degradation to support viability data
- Mechanically tested the strength of tissue at manually induced fracture sites

Professional Experience

Medtronic Laparoscopic Specimen Removal Bag Enhancement Project
Medtronic, Fall 2016 – Spring 2017

- Led team on concept design, prototype development, and mechanical testing for a laparoscopic specimen removal device
- Developed a final working prototype showcased at a design expo, leading to adoption by Medtronic and anticipated market launch within six months

New England Medical Innovation Center (NEMIC)'s Med Tech Leadership Program *CranioFix,* Fall 2021– Spring 2022

- Served as CSO of CranioFix, a medical device startup, focusing on innovation in medical technology and participated in the NEMIC accelerator program
- Negotiated a partnership agreement with Brown University and Rhode Island Hospital for IP usage
- Developed an enhanced design for extra-ventricular drainage devices by directly consulting with physicians and stakeholders

Community Engagement

Graduate Biomedical Engineering and Biotechnology Advisory Board (BMEB) *Cohesion Committee* Summer 2019 – Fall 2020

- Actively represented biomedical engineering graduate students, enhancing student-faculty communication and program cohesion

Brown Refugee Youth Tutoring and Enrichment (BRYTE) Spring 2020 – Spring 2021

- Chosen from a competitive applicant pool to mentor a high school senior
- Assisted with various STEM related assignments and successfully assisted with collegiate applications

PREFACE AND ACKNOWLEDGEMENTS

First and foremost, all praises and thanks are due to Allah. I dedicate this pursuit of knowledge for the sake and pleasure of Allah and His final messenger Muhammad, peace and prayers be upon him.

I extend my deepest gratitude to my family for their unwavering support throughout my academic journey. Their love and encouragement have been essential to maintaining my mental and emotional stability. To my mother, Dr. Amira Rehaimi, and my father Mohammed AlGhosain, I can never fully express the gratitude you deserve, but I will never stop trying, Insha'Allah. My brother, AbdulAziz AlGhosain, has been my closest friend and confidant since before I graduated high school. We have always leaned on each other, and I ask Allah to preserve our bond.

I am grateful to the members of the Lee Lab, who have been a constant source of support and guidance, beginning and ending with Dr. Lee. His patience, mentorship, and respect have been instrumental to my development as a researcher, and I am deeply thankful for his guidance. Dr. Jiarui Nie, my close collaborator on the plasmonic retinal prosthesis (PRP) project, was indispensable to the success of my experiments and the maintenance of my schedule. Her willingness to assist and support me at every step is something I truly appreciate. I am also thankful to Dr. Kyungsik Eom, whose foundational instruction enabled me to begin this work and who played a vital role in my early training in the lab.

To Dr. Ahbid Zein-Sabatto, the finest friend, roommate, and brother in Islam a man could ever ask for, may Allah reward you for your sincerity, support and companionship.

I would also like to thank the staff members at Brown University Environmental Health & Safety (EH&S), who consistently did their best to accommodate the shipment of our biological samples. Geoff Williams for training me to use the imaging systems at the Leduc Bioimaging facility. Additionally,

members of the stockroom at Barus and Holley and BioMed. Special thanks to Christen Owen who trained me in cardiac stick blood collection and was essential to the success of my systemic toxicity experiments.

I thank the broader Muslim community in Rhode Island, and especially the members of the Islamic Center of Rhode Island, Masjid Al-Kareem. Your presence and fellowship provided me with a spiritual and emotional foundation throughout my time at Brown.

Finally, I thank my thesis committee, Dr. Eric Darling, Dr. Kareen Coulombe and Dr. Tao Liu, for their time, effort, and thoughtful engagement with my work. Their feedback and encouragement have been invaluable in elevating the quality of both this thesis and my defense presentation

Table of Contents

List of Tables

List of Figures

1. Chapter 1: Background and Overview

1.1. Vision Restoration

Vision is not only central to human perception, but it also defines autonomy, mobility, and identity. Yet, its loss remains one of the most feared sensory deficits worldwide. Blindness, whether partial or complete, results from a wide range of causes including genetic mutations, developmental defects, trauma, or progressive degenerative diseases. While causes vary, the loss of visual perception remains a public health challenge with profound implications for quality of life. Diseases that result in the degeneration of photoreceptor (PR) cells, such as retinitis pigmentosa (RP) and age-related macular degeneration (AMD), are currently irreversible and lack curative treatments.

Visual information is first transduced in the retina, a multilayered neuronal tissue lining the back of the eye. Photons are focused by the lens onto the retina and detected by PR cells, which convert light into electrical signals. These signals propagate through a series of retinal interneurons, including bipolar, horizontal and amacrine cells, before reaching the retinal ganglion cells (RGCs). RGCs transmit the encoded visual information to the brain via the optic nerve (ON). This complex synaptic circuitry, tightly regulated by neurotransmitters and intracellular signaling pathways, underlies the mechanism of human vision. The organization of the neural retina is shown in Figure 1.

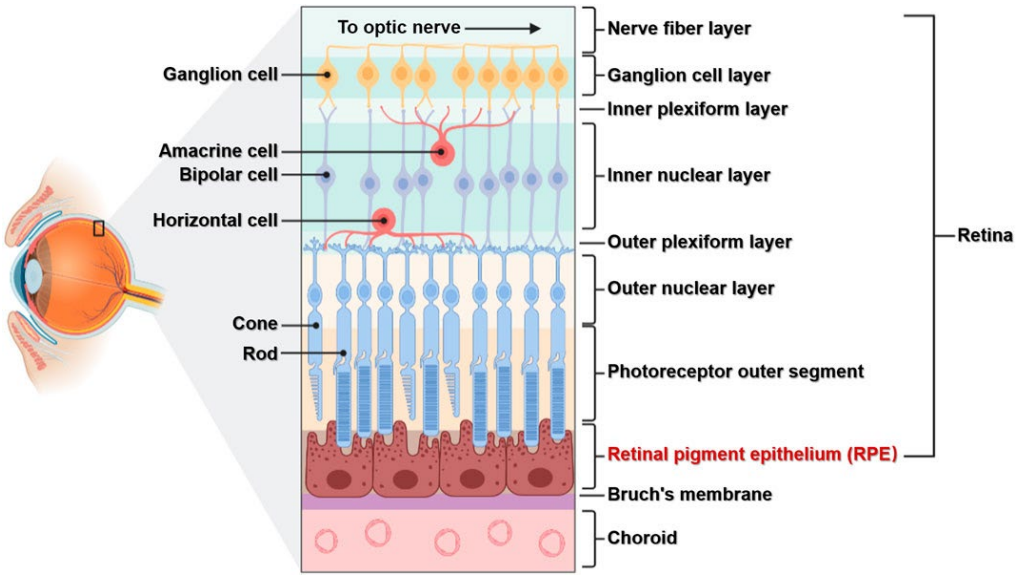

Figure 1 Schematic representation of a retinal cross section displaying the cellular layers of the retina. Adapted from Yang et al., 2021 [1].

In retinal degenerative diseases such as RP, this cascade of visual sensory information is disrupted by the progressive loss of PR cells. Early in the disease course, the degeneration is slow, and surviving PRs may compensate for the loss. However, as degeneration advances, patients experience narrowing of the visual field (tunnel vision), often concluding in complete blindness. Critically, although PRs are lost, much of the inner retinal architecture, including bipolar and ganglion cells, can remain anatomically intact, offering a potential target for prosthetic intervention.

RP and AMD are leading causes of irreversible blindness worldwide. The socioeconomic burden is substantial: AMD alone is estimated to incur global healthcare costs of approximately $300 billion annually, with $250 billion attributed to direct medical expenses[2,3]. While gene therapy is being actively explored for

inherited retinal diseases, its clinical application remains limited by the complexity of genetic heterogeneity, delivery barriers, and regulatory challenges.

This thesis addresses a complementary approach, the development of a plasmonic retinal prosthesis (PRP) capable of bypassing lost PRs and stimulating inner retinal neurons using targeted gold nanorods (AuNRs). Specifically, we investigate the biophysical and biochemical behavior of intravitreally (IVT) delivered AuNRs, focusing on factors such as size, conjugation strategy, and delivery method. By evaluating their ocular biodistribution, cellular targeting, and safety profile, including systemic hematological and biochemical markers, we aim to provide foundational data for the clinical translation of gold nanoparticle-based vision restoration technologies.

1.1.1. Retinal Prostheses

The global number of people with visual impairment is steadily rising and is projected to exceed 280 million people. Age-related macular degeneration AMD and RP are among the two most prevalent diseases that can lead to irreversible blindness [2–7]. Both involve the progressive degeneration and eventual loss of PR cells in the retina. Once these cells are lost, patients lose their ability perceive light and are considered legally blind, which drastically reduces their quality of life. Current treatments do not directly treat the diseases and merely delay the onset of symptom severity [8–11]. Electrical retinal prosthetics (ERPs), which are presently the most prominent technological intervention, suffer from serious limitations, principal among them is poor visual acuity (VA), and the benefits they offer do not outweigh their many shortcomings [12–16].

For patients with advanced stages of retinal degenerative diseases, gene therapies are less viable because the cells these therapies target are often already lost. In such cases, true vision restoration is not yet achievable. The most realistic goal is to delay disease progression and preserve any remaining viable cells. However, the current standard of care raises concerns. Most electrical prosthetics approved or in development require highly invasive and costly surgical procedures. Despite this they still fall short of restoring vision to a level above legal blindness. Other strategies, such as micronutrient supplementation, fail to tackle the root causes and at best offer a temporary delay in disease progression.

Despite their early promise, these first-generation electrical prosthetics revealed critical limitations that have shaped the trajectory of the field. Mainly their low spatial precision and dependence on direct electrode-neuron contact [17], both of which constrain the quality and stability of restored vision. The ARGUS II, shown in Figure 2, targeted the ganglion cell layer from the epiretinal side, and the Alpha-IMS is shown in Figure 3, later replaced by the Alpha-AMS, which positioned electrodes subretinally between the neural retina and the retinal pigment epithelium (RPE). While these designs pursued different anatomical targets, neither approach overcame the inherent issue of current spread within retinal tissue, which leads to nonspecific activation and poor VA.

The clinical performance of both systems was limited; visual acuity gains remained below the legal blindness threshold (20/200) [18], and adverse events were frequent. Patients experienced conjunctival erosion, hypotony, dehiscence, retinal detachment, and elevated intraocular pressure (IOP), a particular concern given its direct association with glaucoma-related vision loss [14,16]. Several individuals ultimately required explantation of their devices due to minimal perceptual gains and surgical complications.

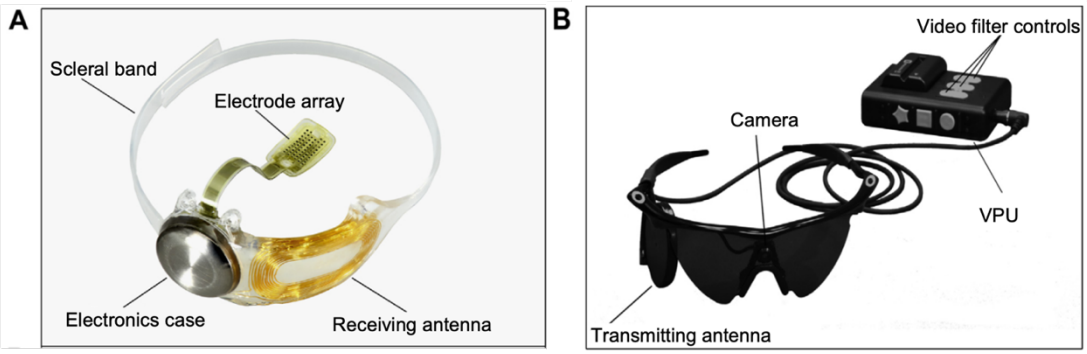

Figure 2 (A) Image depicting the implantable portion of the ARGUS II electrical retinal prosthetic consisting of the electronics case, electrode array, scleral band, and receiving antenna, (B) an image of the external portion consisting of the camera, antenna and video processing unit. Adapted from da Cruz, et al.,2006 [14].

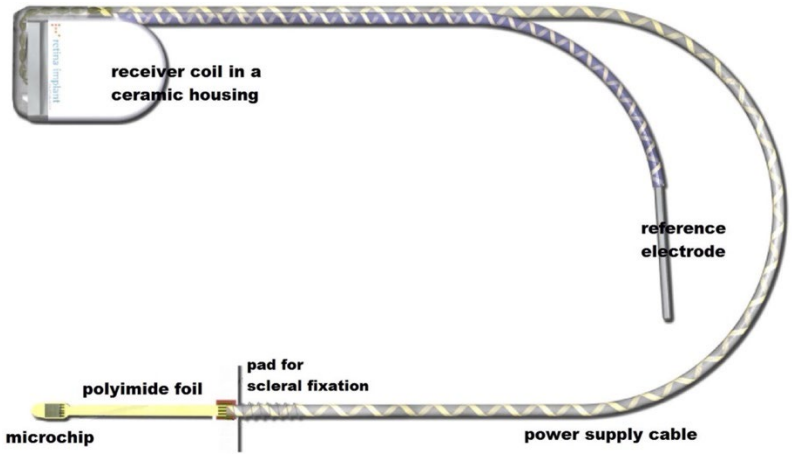

Figure 3 Image of the Alpha IMS electrical retinal prosthetic consisting of the microchip, fixation pad, power supply cable, receiver coil and reference electrode. Adapted from Stingl et al., 2015 [16].

Additionally, the ARGUS II faced a device longevity of approximately five years, further complicating the overall benefits it could provide patients [19]. These risks, coupled with the high surgical burden and lack of meaningful restoration, ultimately led to both the ARGUS II and Alpha series implants being withdrawn from the market by 2019 [20].

Beyond surgical risks and poor acuity, other technical and biological limitations continue to challenge the viability of ERPs, mainly material-related toxicity and the long-term *in-vivo* stability of electrode arrays [14,20,21]. Because electrical stimulation relies on proximity, neurons not directly adjacent to the electrodes often remain unaddressed, reducing the efficacy of retinal network activation [22]. Furthermore, the conversion of visual scenes into interpretable electrical stimuli remains an unresolved bottleneck, limiting the value and usability of perceived visual input. While novel strategies such as transorbital electrical stimulation have reported modest improvements in retinal sensitivity, peripheral field detection, and visual field stability lasting up to three months post-intervention, these studies remain preliminary due to small sample sizes and limited follow-up[23].

Among newer generation devices, the Intelligent Retinal Implant System II (IRIS II), an epiretinal device resembling the ARGUS II, was approved in Europe but failed to demonstrate sufficient clinical benefit. Approximately four patients experienced severe adverse events (SAEs), and the device ceased functioning within 9 to 12 months post-implantation, prompting its discontinuation in 2018 [20]. Development has since shifted toward cortical approaches, such as the ORION

system, intended as a successor to the ARGUS II, shown in Figure 4. However, concerns remain regarding device serviceability, specifically the lack of upgrade or repair options once implanted; a critical shortcoming noted in discontinued platforms like the ARGUS II.

Figure 4 (A) Image of the external portion of the ORION cortical implant shown alongside the cortical implant in the right corner of the image, (B) location of the ORION implant in the visual cortex. Adapted from Ramirez et al., 2023 [20].

Epiretinal implants

More recent retinal prosthetic devices have explored a variety of implantation sites, including epiretinal, subretinal, suprachoroidal, cortical and even optic nerve-based configurations. Among the newer systems is the 256-Channel Intelligent Micro Implant Eye (IMIE 256), also known as the Theia α Implantable Retinal Stimulator. The IMIE 256 consists of an internal implantable component, comprising an episcleral implant, trans-scleral cable, and a contoured electrical array with 256 electrodes. The external wearable unit includes a camera, video processing unit, and configuration system, shown in Figure 5. Initial results

showed that patients performed better on visual tasks with the device powered on compared to when it was off, although subjects required a 90-day rehabilitation period, and the sample size remained small. Larger scale clinical trials with longer follow-up durations are currently underway.

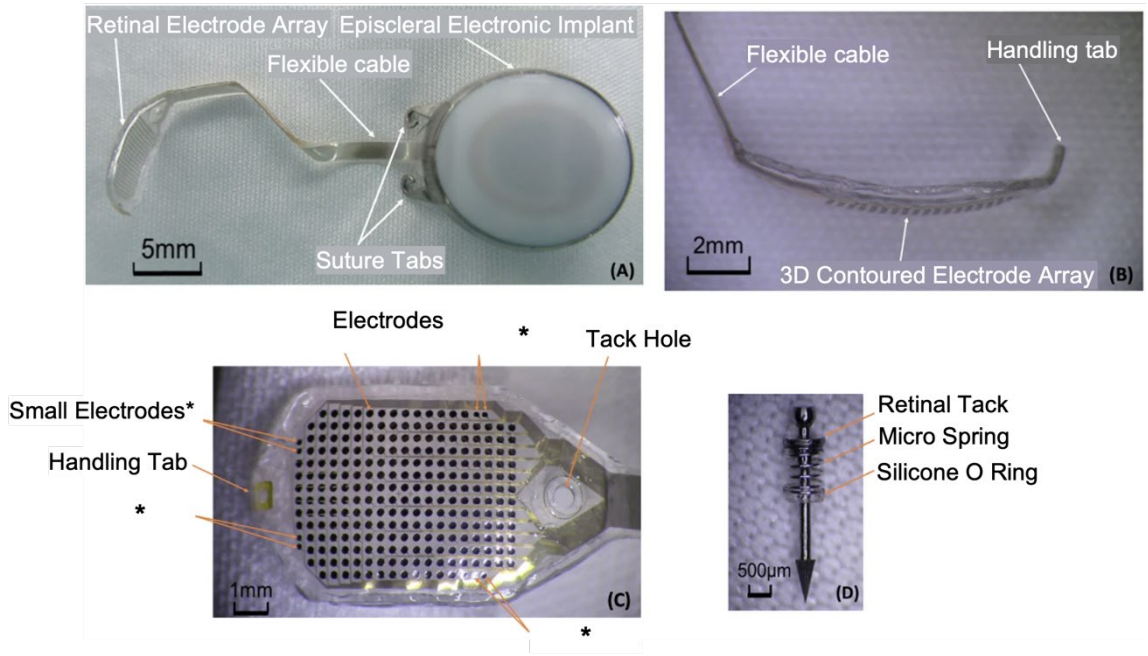

Figure 5 Image of the IMIE 256 retinal prosthetic (A) displays the implantable contoured electrode array, (B) shows a side view of the implantable contoured array, (C) details of the electrode array, (D) retinal tack used to fix the array. Adapted from Xu et al.,2021 [24].

Another notable epiretinal platform is POLYRETINA, a foldable hemispherical photovoltaic device made from polydimethylsiloxane (PDMS), shown in Figure 6. Its conformal shape allows for enhanced retinal coverage via a minimally invasive scleral incision. Preclinical evaluations in rats demonstrated good biocompatibility and stability for up to two years, with no signs of cytotoxicity [25]. *In-vivo* studies in Göttingen minipigs further showed restoration of light-evoked

cortical responses for up to two weeks post-implantation, without exceeding safe stimulation thresholds [26].

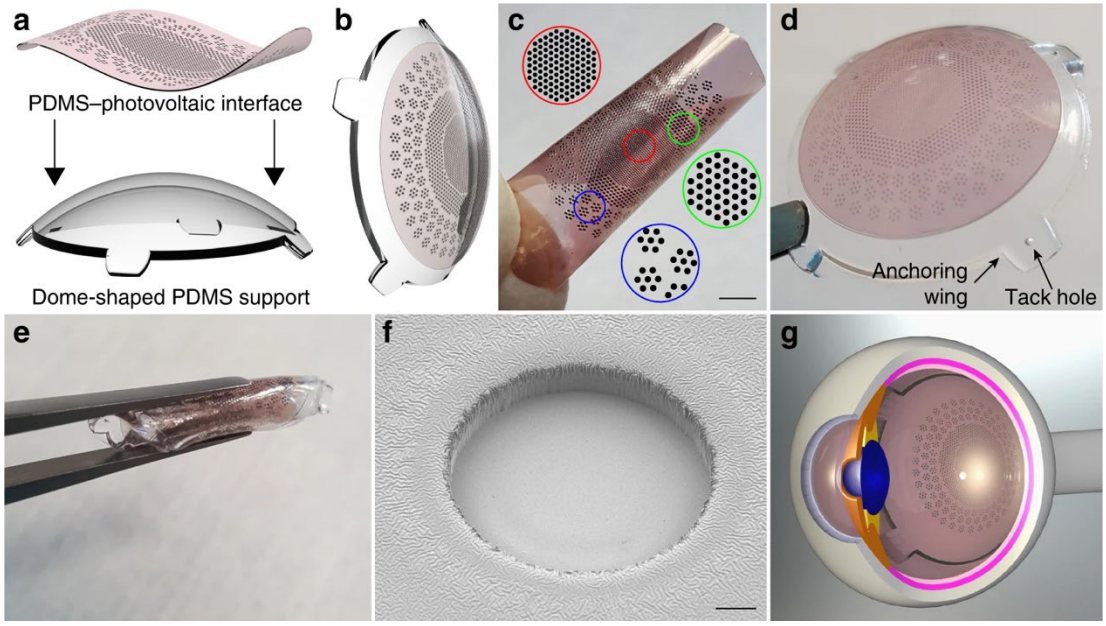

Figure 6 Schematic of the POLYRETINA electrical implant (a) PDMS photovoltaic interface and the dome shaped PDMS support, (b) image showing the PDMS photovoltaic interface coupled to the dome, (c) photovoltaic pixels arranged in three areas of different densities: central area (red) hexagonal arrangement, electrode diameter 150 µm, first ring (green) hexagonal, electrode diameter 130 µm, second ring (blue), 130 µm; (d) picture of POLYRETINA with anchoring wings and tack holes, (e) folding prior to injection, (f) SEM image of a single photovoltaic pixel, (g) representative diagram after epiretinal placement of POLYRETINA. Adapted from Ferlauto et al., 2018 [25].

The EPI-RET3, another epiretinal system, also incorporates both internal and external components. The body of the internal array is coated in parylene C for biocompatibility while electrodes are coated in iridium oxide for enhanced charge transfer [27], shown in Figure 7. The external unit houses a camera and visual processor responsible for wirelessly transmitting spatiotemporal stimulation

patterns. A key design feature is the elimination of physical trans-scleral cables, which may reduce the risk of infection or tissue erosion. However, during clinical testing the device was implanted only temporarily, up to one month, and explanted afterwards. Reported visual responses ranged from no light perception to detection of simple hand movements.

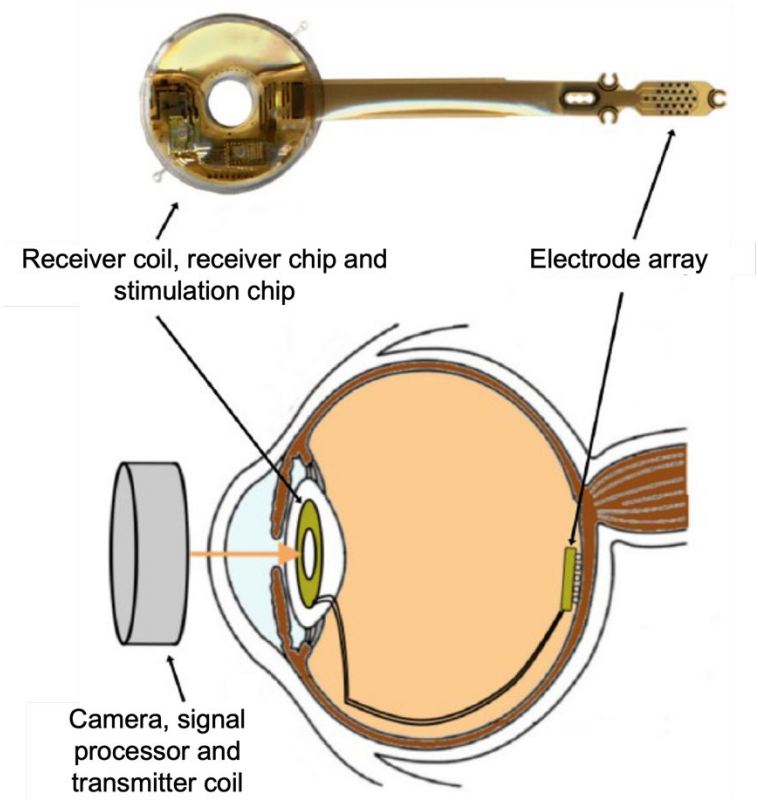

Figure 7 Schematic image of the EPI-RET 3 prosthetic, top image shows the implantable electrode, bottom shows a diagram representing placement and function. Adapted from Bloch et al., 2019 [28].

Subretinal implants

Subretinal implants are positioned beneath the retina, closer to the location of native PRs [29]. This anatomical placement enables direct access to the inner retinal circuitry, specifically bipolar, amacrine and horizontal cells, offering the

potential to leverage more of the natural visual processing pathway. However, surgical implantation in this delicate subretinal space carries notable risks, including elevated IOP, conjunctival erosion, and retinal complications such as detachment or hemorrhage.

One notable subretinal device is the Photovoltaic Retinal Implant (PRIMA), a wireless implant composed of photovoltaic pixels that convert incident light into electrical stimulation [30,31]. The system uses an external wearable, glasses fitted with a camera to capture visual input, which is processed and projected into the eye using near-infrared (NIR) light, the PRIMA is shown in Figure 8. The implant then transduces this light into localized electrical signals to stimulate remaining inner retinal neurons. In a 48-month follow-up study, patients exhibited functional visual improvement in the implanted eye. While some adverse events were reported, such as ocular hypertension, macular neovascularization, and retinal detachment, these were attributed to surgical complications rather than the device itself [32].

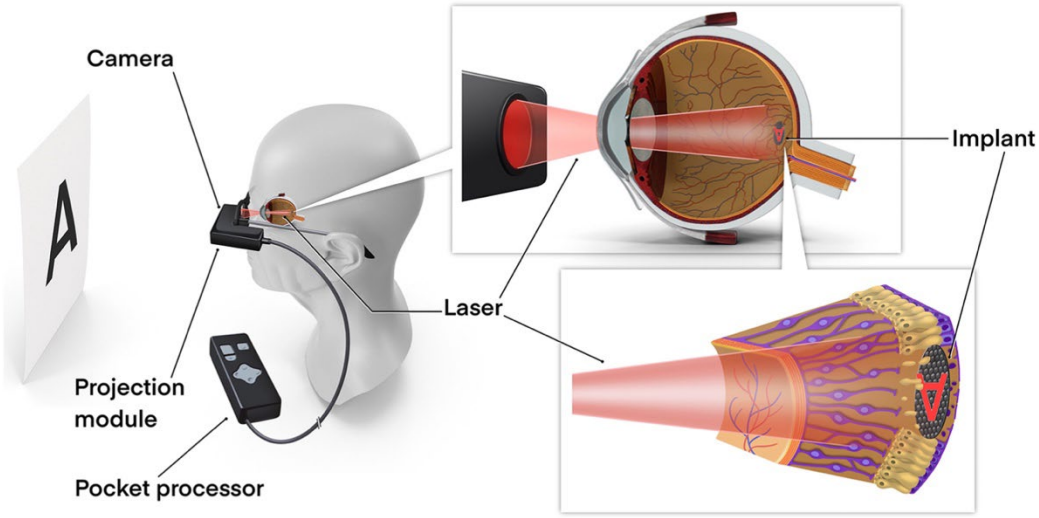

Figure 8 Schematic of the PRIMA electrical prosthetic system and its components, (left) schematic image showing external portions of the device, (top right) NIR beam interfacing with the eye and reaching the implant, (bottom right) implant located in the neural retina receiving NIR beam. Adapted from Muqit et al., 2024[32].

The Boston Retinal Implant Project (BRIP) is another prominent initiative that pioneered subretinal electrical stimulation. Conceptually similar to the ARGUS II, BRIP's device places the electrode array in the subretinal space to take advantage of the preserved inner retinal layers [33]. Early proof-of-concept studies demonstrated that even a single electrode could elicit reproducible visual percepts in human subjects. Building on this foundation, the group has since developed a 256-channel prototype and is currently conducting preclinical evaluations in preparation for phase I clinical trials [34].

Suprachoroidal implants

Suprachoroidal (SC) implants are positioned between the choroid and the sclera. This location allows for less invasive surgical procedures compared to subretinal or epiretinal approaches and offers potential advantages for device maintenance and replacement, since it avoids direct vitreoretinal (VR) access.

However, the high vascularity of the choroid introduces a significant risk of hemorrhage, during or after implantation. Additionally, due to the increased distance from the retinal neurons, these implants require higher stimulation currents to evoke perceptible visual responses, posing challenges in power consumption and heat dissipation [28].

An example of this class is the Generation 2 device by Bionic Vision Australia. It consists of a 44-channel platinum disk electrode array paired with external components, including a headpiece, glasses with a mounted camera, and a body-worn image processing unit. Electrical stimulation is powered by two current sources implanted post-auricularly beneath the scalp. In Phase II clinical trials, four participants received the device and reported no SAEs, alongside measurable improvements in visual performance [35]. Further development is ongoing to enhance the resolution and visual acuity achievable with this platform.

The Phoenix-99 represents a newer generation of fully implantable SC devices. It comprises 98 stimulation sites distributed across a SC electrode array, coupled with an integrated visual stimulator and telemetry system. In a recent preclinical study, nine passive prototypes were implanted in sheep and monitored for up to three months [36]. The devices showed no signs of infection, neovascularization, or histological damage in the surrounding ocular tissues. Additionally, the RGC layer was found to be preserved, supporting the device's biocompatibility. While these early results are promising, human clinical trials are still needed to evaluate the efficacy of visual stimulation and the long-term stability of the device *in-vivo*.

Optic nerve stimulation and passive implants

Optic nerve stimulation has emerged as a less commonly explored but promising approach for visual stimulation in patients with severe retinal degeneration. One such device, the Artificial Vision by Direct Optic Nerve Electrode (AV-DONE), consists of an electrode array implanted at the optic disk. Clinical follow-ups conducted at 9- and 23-months post-implantation demonstrated the consistent perception of phosphenes by patients during stimulation sessions. Notably, routine ophthalmic evaluations conducted over a 25-month follow-up period reported no major complications suggesting a favorable safety profile [37].

The Artificial Silicon Retina (ASR), developed by Optobionics (Glen Ellyn, IL, USA), represents an early effort in the development of passive retinal prosthetics. This device measured 2 mm in diameter and 25 μm in thickness and was composed of approximately 5,000 micro-photodiodes. Unlike active implants, the ASR was designed to harness ambient light to generate stimulation without the need for external power sources or imaging systems [38]. In a clinical study involving ten patients, four reported localized phosphene perception corresponding to the site of implantation. However, extended follow-up in six patients revealed that the observed perceptual improvements were likely due to neuroprotective effects rather than direct photic stimulation. These findings ultimately led to the conclusion that ambient light alone was insufficient to drive functional retinal activation [39].

Despite differences in anatomical placement and design, nearly all the subtypes of electrical retinal prosthetics share a fundamental limitation: their

inability to replicate the resolution clarity of natural vision. Among currently evaluated devices, the Alpha IMS has demonstrated the highest visual acuity to date, reaching approximately 20/546. The ARGUS II follows with reported acuity near 20/1262, while the IMIE 256 ranges between of 20/800 and 20/1200 [24] , and the PRIMA between 20/438 to 20/565 [32]. For context, a visual acuity of 20/200 defined the clinical threshold for legal blindness. None of these devices, therefore, restore vision to a level that exceeds that benchmark.

The theoretical resolution of current electrode arrays remains approximately 12 fold lower than a healthy human retina [40] . Furthermore, electrical stimulation efficacy is often compromised by suboptimal contact between electrode array and the targeted retinal neurons. While increasing proximity can enhance stimulation precision, it simultaneously raises the risk of mechanical complications such as hemorrhage, retinal degeneration, and detachment [28]. This tight anatomical integration also complicates the device repositioning or removal, further limiting the practicality of these systems.

In summary, despite decades of development, ERPs remain inadequate in fulfilling their primary goal, restoring meaningful vision. They continue to face substantial limitations, including invasive and costly implantation procedures, substandard visual acuity, risks of retinal damage, limited device longevity, and poor long-term reliability, particularly with respect to device maintenance and servicing after implantation [24,28,32,40]. These limitations underscore the urgent need for alternative strategies that can overcome the inherent drawbacks of

electrical stimulation and provide safer, more effective restoration of visual function.

1.1.2. Other Approaches

Alternate strategies for vision restoration include optogenetic therapies, chemical photoswitches, cell-based therapies, and novel stimulation modalities. Optogenetics involves genetically modifying retinal neurons to express light-sensitive proteins, enabling light-driven neuronal activation. Chemical photoswitches, by contrast, are synthetic molecules that confer light sensitivity to endogenous retinal proteins in a dose dependent and reversible manner. Cell-based therapies aim to replace lost PRs using stem-cell-derived retinal cells . Novel stimulation techniques under exploration include ultrasound, magnetic field stimulation, and sensory substitutions. While each of these approaches offer distinct advantages, most remain theoretical, or are still in the pilot or early proof-of-concept stages.

Optogenetics

Optogenetics specifically targets surviving retinal neurons modifying them to express opsins. These light-sensitive proteins originally found in microbial or animal systems. These opsin act as either light-gated ion channels or pumps (type I, microbial opsins) or as G-protein-coupled receptors involved in vertebrate vision (type II, animal opsins) [41]. Among the most studied microbial opsins are channelrhodopsins (ChRs), halorhodopsins (NpHRs), and archeorhodopsins (Archs).

Channelrhodopsin-2 (ChR2), was the first microbial opsin used for vision restoration; its expression in the RGCs of blind mice restored light-evoked responses, though not behavioral vision [42]. This limitation led to targeting second-order neurons. By employing cell type specific promoters, later studies successfully expressed ChR2 in ON-bipolar cells (ON-BCs), resulting in measurable behavioral improvements [43–46]. However, ChR2 requires blue light stimulation at intensities near 10^{15} photons/cm^2/s [42], which approaches the maximum permissible ocular exposure under safety standards defined by the International Commission on Non-ionizing Radiation Protection [47].

To mitigate the risks associated with the high-intensity blue light required to activate ChR2, several alternative opsins have been developed. CatCh, a calcium-permeable ChR2 variant, was tested in macaque retinas and demonstrated approximately half the firing efficiency of ChR2 when stimulated at intensities within the safe exposure limits [48]. To further reduce phototoxicity, attention moved towards red-shifted opsins with activation spectra in the longer wavelengths (>580 nm), which are less damaging to ocular tissues. Among these, ReaChR [49,50], and ChrimsonR [51] have emerged as promising candidates. ChrimsonR, in particular, is currently undergoing clinical evaluation using stimulation goggles in combination with intravitreal (IVT) delivery (NCT03326336) [52].

In addition to excitatory opsins, inhibitory microbial opsins such as halorhodpsins (NpHRs) have been investigated. NpHR enables light driven inhibition of neuronal activity by hyperpolarizing the membrane [53]. An improved version, eNpHR2.0, was expressed in cone PRs of mouse models of retinitis

pigmentosa (RP), a condition characterized by progressive photoreceptor degeneration. Notably, in humans with RP, cone cell bodies can persist even after photosensitivity is lost [54]. Expression of eNpHR2.0 in mouse cones restored light responses in both ON and OFF RGCs, elicited light-evoked activity in the visual cortex, and enabled behaviors in mice [55].

'Jaws', a red shifted NpHR derived from *Halobacterium salinarum* (Halo57), showed membrane localization and light-induced hyperpolarization with high temporal resolution when expressed in RP mouse cones, live macaques, and postmortem human retinal explants [56]. Both eNpHR 2.0 and Jaws are activated by orange light, offering potential for human use, though their effective stimulation still requires high intensity illumination [55,56].

Animal opsins offer several theoretical advantages over microbial opsins, particularly regarding immunogenicity. Although animal opsins are found across a wide range of non-mammalian and mammalian species, their structural similarity to endogenous proteins makes them more likely to be tolerated in the mammalian retina [53]. Optogenetic approaches using animal derived light-activated G protein coupled receptors (GPCRs) have been investigated for restoring visual function in blind mice. One such strategy involved engineering a molecule, Opto-mGluR6, comprising mouse melanopsin and the mGluR6 receptor. When expressed in ON-BCs using the GRM6/SV40 promoter to ensure cell-type specificity, the modified cells responded to light by mimicking OFF-cell behavior. This was due to the glutamate-sensitive nature of mGluR6, which is active under dark conditions. Functional expression was confirmed by the presence of an inverted b-wave in the

electroretinogram (ERG) recordings compared to control animals. Moreover, opto-mGluR6 mediated light responses were observed in ON-BCs, RGCs, and the visual cortex, and were accompanied by measurable behavioral responses [57].

Type II (animal) opsins encompass a diverse group of nearly 1000 proteins, broadly classified into three main groups, ciliary opsins (c-opsins), rhabdomeric opsins (r-opsins), and other opsin subtypes [58,59]. These opsins are found in a wide range of species, including arthropods, mollusks, cephalochordates, and vertebrates [58]. In vertebrates, c-opsins have evolved from functioning as bright-light detectors, to enabling dim-light vision through the specialization of rod PRs[60]. Vertebrate c-opsins include rod opsin (OPN1), and the cone opsins (OPN2), tmt-opsin, encephalopsin (OPN3), pinopsin, parapinopsin, VA opsin, and parietopsin [58]. OPN1 has been successfully expressed in ON-BCs using specific promoters [61,62], and also observed under non-selective expression throughout the retina [62]. Both studies demonstrated restoration of light responses in *ex-vivo* retinal explants, and visual evoked potentials (VEPs) in the visual cortex. When targeted to BCs, OPN1 expression led to behavioral improvements in blind mice, including light avoidance, and memory recall during fear conditioning tests [61].

A more recent study demonstrated that virally delivered medium-wavelength cone opsin (MW-opsin) to RGCs could achieve light sensitivity comparable to rhodopsin, the native light-sensitive protein found in rod PRs, while exhibiting a 10-fold increase in kinetics [63]. Behavioral comparisons between MW-opsin and rhodopsin-treated blind animals showed no significant difference in outcomes, suggesting similar efficacy. Moreover, MW-opsins restored the ability to

discriminate between flashing and constant light, and between line patterns with different orientations.

Notably, the authors claimed that the MW-opsin enabled RGCs to adapt across a broad range of ambient light conditions, such as transitions between over indoor and outdoor environments, mimicking aspect of natural vision. Behavioral assessments further indicated that object and pattern recognition are possible in the RP mouse model. However, this study did not include cortical or VEP recordings to corroborate functional vision restoration at the central level. Instead, *ex-vivo* whole-cell patch clamp recordings constituted the primary mode of functional analysis. While these findings are promising, future *in-vivo* electrophysiological validation will be critical to substantiate the claims regarding real-world visual performance.

Photopharmacology (chemical photoswitches)

Another strategy for vision restoration is photopharmacology, which involves replacing the endogenous chromophore retinal with synthetic molecules that enhance the light sensitivity of otherwise non-photosensitive channels [64]. This approach is subdivided into one- and two- component systems. In the one-component system, synthetic photoisomerizable compounds, most notably azobenzene derivatives, act as reversible ligands (azobenzene-ligands). They can activate ion channels or GPCRs in response to light. In the two-component system, the target protein is genetically engineering to contain a specific anchoring site for a tethered azobenzene-based ligand, known as a photo-switchable tethered ligand (PTL). The engineered channel can then be selectively expressed in desired retinal

cell populations using genetic targeting approaches like those employed in optogenetics. These photopharmacological interventions offer precise, light-dependent control over neural activity, with the potential to bypass degenerated PRs and modulate downstream circuits.

The PTL approach was exemplified by the photo-agonized kainite receptor, LiGlUR, which was expressed in RGCs or ON-BCs in the degenerating (*rd1*) mouse retina. This intervention led to light-evoked spiking activity resembling that observed in wild-type (WT) mice [65,66], and healthy human retinas [67,68]. LiGluR expression restored sufficient light sensitivity to support visually guided navigation and pattern discrimination in RP mouse models [69,70]. Furthermore, the therapeutic relevance of LiGluR was extended to a large-animal model of inherited retinal degeneration (*Rcd1*), where it significantly increased light sensitivity in affected canines [70]. These results underscore the translational promise of PTL-based strategies for vision restoration beyond rodent models.

Despite these encouraging outcomes, PTL-based methods face several limitations. A key issue is off-target labeling, as LiGluR relies on cysteine residues which are prevalent in many native proteins. This non-specificity compromises target precision and may introduce unintended effects. Moreover, the efficacy of PTL-based stimulation is transient, with functional effects typically persisting for only around ten minutes post-application [71–73]. The commonly used azobenzene-derived moieties are also prone to hydrolysis, requiring higher local concentrations and more frequent administrations to maintain therapeutic efficacy. These

requirements introduce additional complexity and elevate the risk of adverse effects such as inflammation or toxicity due to repeated intraocular injections.

To address some of the limitations of conventional PTLs, a modified strategy was developed using different linkers and promoters, enabling the attachment of the photoswitch to a protein tag via biorthogonal chemistry [74]. This platform, referred to as photoswitchable orthogonally remote tethered ligands (PORTLs), improves targeting and stability. However, PORTLs introduced a new limitation, reduced light sensitivity, similar to earlier optogenetic constructs [75]. This necessitates the use of external light amplification devices, such as goggles or glasses, to ensure sufficient retinal stimulation while remaining within the phototoxicity thresholds defined for ocular safety. Although PORTLs can persist in the ocular environment for up to six weeks [76], repeated injections are still required to maintain therapeutic activity. Ongoing efforts are directed at developing sustained-release reservoirs to mitigate the burden of repeated dosing.

Advocates of photopharmacology often highlight a key advantage over optogenetics: the reversibility of treatment. Unlike gene therapies used in optogenetics, photoswitch molecules can, in principle, be cleared from the ocular environment, offering patients the possibility to discontinue or transition to newer treatments. However, this perceived benefit is undermined by the lack of precise control or reliable characterization of photoswitch disengagement kinetics.

Inconsistent clearance rates between patients could result in unpredictable vision fluctuations or abrupt therapeutic lapses, necessitating unplanned re-injections. Furthermore, patients may not be aware when disengagement occurs,

potentially compromising visual function and safety. These factors emphasize the importance of achieving more predictable pharmacokinetics and user-monitorable dosing strategies in future iterations of pharmacological therapies.

Ultrasound neuromodulation

Ultrasound (US) stimulation has emerged as a promising approach for neuromodulation, including applications in vision restoration. It can influence neuronal activity through three primary physical mechanisms: thermal effects, cavitation (bubble formation), and acoustic radiation force [77]. High-intensity US can increase local temperatures, enhancing neuronal excitability and action potential firing [77,78]. However, even low-intensity US, absent of the significant temperature increase, has been shown to modulate neural activity, thereby reducing concerns over thermal damage [79,80]. Among the proposed mechanisms, acoustic radiation force is widely regarded as the most plausible basis for US neuromodulation. This force deforms neuronal membranes, activating mechanosensitive ion channels through membrane stretch or curvature changes [81–83].

In an *in-vivo* study, researchers compared VEPs elicited by US retinal stimulation to those induced by conventional light flashes in anesthetized rats [84]. Light flashes were delivered via a high-intensity blue LED, while the US transducer was coupled to the rat's eye using a custom-built conical interface. VEPs were successfully recorded following US stimulation, although responses to light were significantly larger and more variable. Short-term safety was assessed using electroretinography (ERG) recordings and histological analysis in separate

animals. Neither ERG recordings nor histology revealed damage to retinal layers. The same group also explored patterned stimulation capabilities. However, further studies, including *in-vivo* testing in awake animals, are required to validate functionality under naturalistic conditions involving movement and ambient auditory interference.

Gene replacement therapy

Gene replacement therapy for vision restoration, whether by replacing or protecting retinal neurons, is an increasingly active area of research. As of April 13th, 2025 approximately 329 genes and 358 loci have been implicated in retinal degeneration [85]. The first FDA approved gene therapy for an inherited retinal disease is Luxturna (Spark Therapeutics), which targets RPE65, the gene mutated in Leber congenital amaurosis type 2 (LCA2), a severe juvenile-onset retinal dystrophy [86–88]. While not curative, Luxturna has demonstrated clinical benefit and safety, enabling some patients to regain the ability to navigate dimly lit obstacle courses (NCT00999609) [89].

Other clinical programs focus on the restoration of PR function. Many PR-related mutations often affect the phototransduction cascade. For example, achromatopsia, a cone dysfunction disorder characterized by the color blindness and visual acuity loss, affects approximately 1 in 30,000 individuals, and is commonly caused by a mutation in CNGA3 and CNGB3, which encode subunits of cone-specific cyclic nucleotide-gated (CNG). Adeno-associated viral vector (AAV)-mediated gene replacement therapy strategies have successfully restored cone function in rodent models [90] , and several clinical trials are currently ongoing.

X-linked RP, accounting 15-25% of RP cases, is frequently caused by mutations in RPGR, a gene encoding GTPase regulator essential for PR function. AAV-based gene therapy has demonstrated the ability to slow PR degeneration in both rodents and canines [91–94]. Although, this therapy does not halt degeneration entirely, phase I/II clinical trials are in progress. Similarly, mutations in PDE6B, which encodes the β-subunit of rod cGMP phosphodiesterase critical for phototransduction, result in severe RP. A clinical trial is currently underway to correct the PDE6B coding sequence using gene therapy.

Stargardt macular dystrophy, a juvenile-onset form of inherited macular degeneration, is caused by mutations in the ABCA4 gene, a PR-specific flippase. Dysfunction of ABCA4 leads to the accumulation of cytotoxic retinoid byproducts and progressive PR death. The condition affects approximately 1 in 8,000 to 1 in 10,000 individuals and results in severe central vision loss from early life [95]. Due to the large size of the ABCA4 coding sequence, it is delivered using an equine infectious anemia virus (EIAV)-based lentiviral vector, rather than AAV. A phase I/II dose-escalation trial is ongoing.

Additionally, RS1 which encodes retinoschisin—a protein secreted from PRs and BC essential for retinal cellular organization. Mutations in RS1 cause X-linked retinoschisis, a juvenile macular dystrophy characterized by splitting of the inner retinal layers and progressive vision loss. Two phase I/II trials are currently investigating gene replacement therapy for RS1 [95].

1.2. Plasmonic Retinal Prosthesis (PRP)

Each of the previously outlined approaches has several drawbacks. Regarding electrical retinal prosthetics, the gold standard for retinal prosthetics, the issues are very concerning. In summary, the current state-of-the-art approach suffers from potential toxicity of the electrodes utilized, the short-term longevity of the electrodes prior to corrosion and decreased stimulation efficacy, poor visual outcomes that may only afford light perception, the invasive nature of the implantation and excision surgeries, increased risk of SAEs with some of the mentioned examples, a potential lack of access to maintenance after implantation, and a high overall cost to the procedure and device (*see above for more details, section 1.1.1*).

Optogenetic approaches while seemingly promising, also suffer from major drawbacks. For instance, once a therapeutic effect is achieved and the channel has been expressed in the patient's retina, any advancements in the field are inaccessible to that patient. A patient cannot decide to discontinue treatment; thus, it makes it very difficult to navigate which optogenetic approach a patient should consider. While electrical prosthetics have risks during surgery, a patient could decide to excise their current device and replace it with the latest technology. Furthermore, some optogenetic approaches suffer from a lack of sensitivity to light and may require glasses/goggles to intensify light but increase the risk of retinal damage in doing so. Furthermore, optogenetic approaches are still being studied and understood, with few approaches undergoing clinical trials.

US stimulation may offer a new technological approach to vision restoration but is still in its infancy. Further research is required to fully understand and devise proper stimulation techniques to lead to the clinical adoption of this technology. Not to mention, the potential for interference from other sound waves should a patient use them in conditions with loud noise around them. Proper thresholds need to be defined to exert stimulatory effects, without causing any disruption to the tissue of the eye. Current research was conducted while the animal was anesthetized, and more clinically relevant conditions are necessary to further validate the technology.

Gene replacement therapy, while often regarded as the future of vision restoration, faces substantial scientific, regulatory, and clinical barriers. To date, 329 genes and 358 loci have been associated with various forms of visual impairment. It would be difficult to test and determine all of these without the use of advanced clinical software, likely coupled with artificial intelligence (which poses its own clinical and regulatory hurdles). Moreover, currently approved gene therapies such as Luxterna, primarily slow down degeneration rather than restore vision, offering limited hope for patients already affected by early-onset or rapidly progressive forms of blindness. Compounding these limitations are socioeconomic and access-related barriers that disproportionately affect patients in low-resource settings. These challenges cast doubts on gene therapy's ability to become the universal standard of care for treating irreversible vision loss.

Building on the limitations of current approaches, the next section introduces an emerging modality in neural stimulation that may redefine strategies for vision restoration.

1.2.1. Photothermal stimulation

Optical stimulation of neural cells is an artifact free, contactless and relatively damage-free method whereby modulation is achieved through the delivery of light waves in visible and infrared bands to the target area [96]. Infrared neural stimulation (INS) offers certain advantages, including an increased penetration depth and a high spatial selectivity [97,98]. This was exemplified by the selective stimulation of neurons that lay directly within the optical path and have the potential to enhance cochlear implant systems [99,100]. INS is typically accompanied by a localized temperature elevation within the vicinity of the applied beam, within the context of neurons this involves the heating of the plasma membrane to fire action potentials [96]. It is believed that this mechanism of activating neuronal cells by transient heat, relies on the activation of temperature sensitive ion channels (such as TRPV channels), and/or the change of membrane capacitance or conductance [101–104]. To further enhance this phenomenon, and increase the efficiency of infrared mediated temperature induced neural stimulation, gold nanoparticles have been used to exploit their unique optical property, known as localized surface plasmons (LSPs) [105,106].

Gold nanoparticles (AuNP) illuminated at their resonant frequency offer enhanced energy absorption and a refined generation of heat energy [107]. Nanoparticle plasmons confine the electron oscillations to the nanoscale volume and offer the ability to manipulate this light interaction. Plasmonically triggered localized heat can activate temperature sensitive ion channels to cause an influx of calcium ions, effectively stimulating the neurons with a high degree of spatial

precision [96]. Infrared-AuNP coupled repetitive irradiation has been associated with potential tissue damage and constraints regarding repeated use.

Eom et al, was able to demonstrate the effective generation of compound nerve action potentials (CNAPs) through the use of gold nanorod (AuNR) near-infrared (NIR) stimulation of nerve axons [96], a schematic of this approach is shown in Figure 9. AuNRs are preferred for this approach due to an increased efficiency in energy absorption and heat transduction associated with the rod shape, and the association between resonant frequency and aspect ratio.

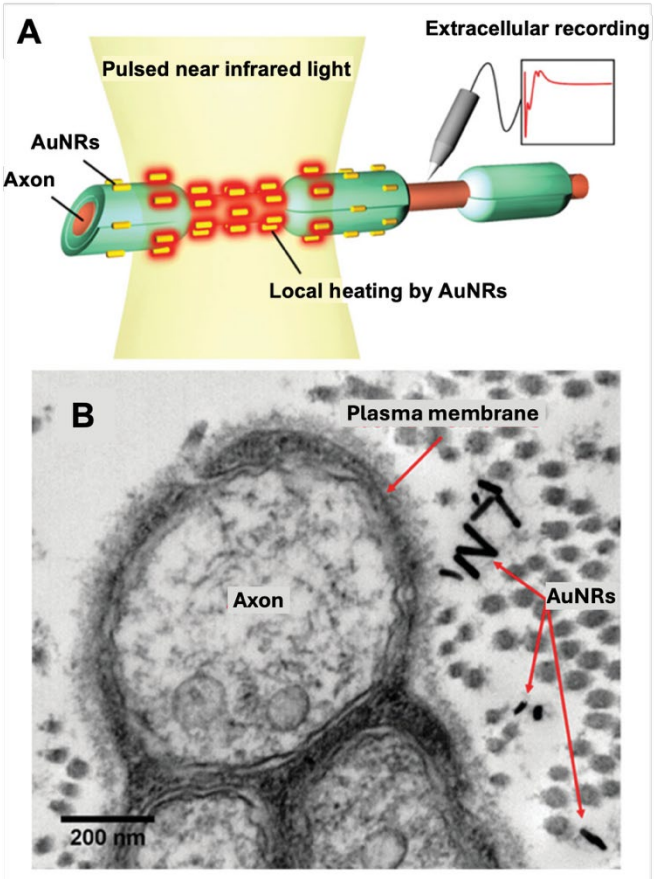

Figure 9 (A) Schematic diagram depicting NIR stimulation of a nerve axon using AuNRs, pulsed NIR light absorbed by AuNRs generates local heat to activate temperature-sensitive ion channels, (B) TEM image showing a cross section of rat sciatic nerve axons with AuNRs in the vicinity of the plasma membrane. Adapted from Eom et al., 2014 [96].

In their study, AuNRs were located near the plasma membrane of rat sciatic nerve axons and irradiated with an NIR laser at a frequency of 980-nm, the AuNRs were approximately 80-nm long and 15-nm wide (aspect ratio of 5.3). A variety of laser powers were used to test the hypothesis that AuNR-mediated stimulation may circumvent the associated tissue damage of INS without AuNRs. Furthermore, preliminary experiments examined the transient heat with and without AuNRs and showed that with the use of AuNRs in a solution of water, a laser power of 3.24×10^{-3} J/pulse led to a temperature increase by more than 6°C, and a solution of water lacking AuNRs had no notable change in temperature. CNAPs in exposed rat sciatic nerves with and without AuNRs demonstrated that AuNRs facilitated an increased response.

A sham negative control receiving no stimulation was compared to a sample that received stimulation energy levels of approximately 2.2 J/cm^2 showing that high energy levels can lead to irreversible tissue damage. This highlights the importance of striking a balance between generating a high temperature increase and managing tissue safety. The high level of 2.2 J/cm^2 was well above the threshold (typically around 1.0 J/cm^2) required for biologically relevant stimulatory effects and was used to exemplify the potential for tissue damage when excess energy levels are applied.

This approach was further exemplified by several other researchers, where stimulating a cell with AuNRs led to a calcium ion influx. It was demonstrated in neuronal cells *in-vitro* [108], in cultured rat hippocampal neurons [109], and dorsal root ganglion neurons [110]. Recently, astrocyte stimulation has been explored by means

of NIR-AuNRs [111]. This method was preferred over electrical or mechanical methods, due to the minimally invasive nature of AuNR coupled NIR stimulation strategies.

They were able to show that AuNR assisted NIR stimulation led to an elevation of the influx of calcium ions, while the lack of AuNRs did not induce a significant change in calcium. Additionally, this was demonstrated *in-vivo* where AuNRs were directly injected to the vibrissae motor cortex of a rat after a scalp incision was made [109]. The AuNRs were tagged with an anti-Thy 1.1 antibody, and whisker movement was measured. Results demonstrated successful responses with whisker oscillations, and this response was not observed in the absence of AuNRs. Some of the challenges of utilizing this approach, aside from the safety concerns of irradiation related tissue damage, are ensuring the gold nanorods arrive at the target cell, remain bound to plasma membranes, avoid endocytosis, and maintain a biocompatible safety profile.

1.2.2. Photothermal activation of retinal neurons

The mechanism of photothermal neuron activation depends on temperature sensitive ion channels that respond to transient increases in membrane temperature while remaining within physiologically safe limits. Nakatsuji et al. demonstrated that in the presence of AuNRs, neurons could be activated by thermally stimulating transient receptor potential vanilloid type 1 (TRPV1) channels with NIR irradiation at 780-nm [112]. TRPV1 activation was assessed through Ca^{2+} flux assays using fluorescent indicators, and neurons expressing TRPV1 displayed irradiation time-dependent increases in fluorescent intensity, whereas cells lacking

the channel showed no response. This AuNR-mediated thermal effect was confined to the resonance absorption peak around 780-nm, with greatly suppressed responses at off-resonance wavelengths, underscoring the specificity of the approach. However, TRPV1 channels require relatively high temperatures (>43°C) to activate [113], which may constrain their direct applicability in the retinal environment. The TRPV1 approach is outlined in Figure 10.

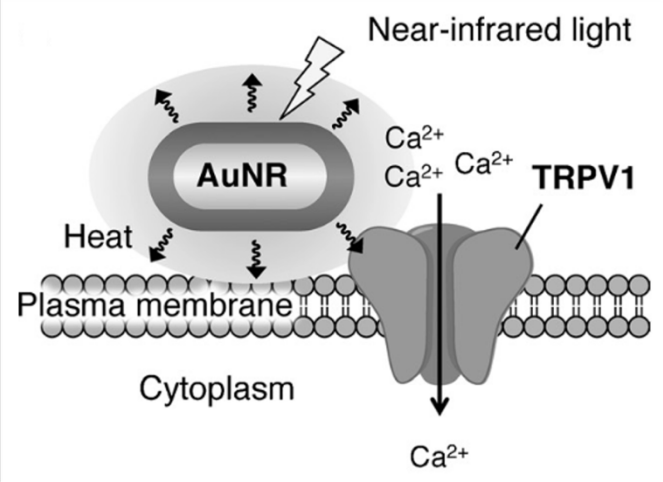

Figure 10 Schematic of TRPV1 channels expressed in plasma membranes of neurons with AuNRs in their vicinity. Near-infrared light irradiates the AuNR, leading to a temperature fluctuation that activates temperature sensitive ion channels, depolarizing the cell and allowing an influx of Ca^{2+} ions. Adapted from Nakatsuji et al., 2015 [112].

Among thermosensitive TRP channels, TRPV4 emerges as particularly relevant to photothermal stimulation because it is active within the physiological temperature range (~30-37°C) and responds to lower, localized increases near baseline body temperature. In contrast, TRPV1 requires a higher activation threshold (>43°C), making its contribution to neuronal signaling less significant in situations below this threshold. Changes in capacitive membrane current may also

contribute to activation of TRPV4 channels, through rapid membrane depolarization. Albert et al. investigated mid-infrared (1875-nm) stimulation in rodent retinal ganglion cells (RGCs) and vestibular ganglion cells (VGCs) using patch-clamp recordings and showed reproducible responses dominated by TRPV4 activity [114].

Irradiation at 230 mW for 7-10 ms produced local temperature elevations of ~10°C ± 2°C , corresponding to the TRPV4 activation range [115,116]. Importantly, repeated stimulation over several minutes produced no cellular damage. Supporting these findings, Wells et al. reported that optical stimulation in peripheral nerves could trigger neuronal responses with temperature increases as low as ~6°C, and that repeated pulses did not yield additive thermal loading, with complete dissipation back to the baseline occurring within ~70 ms [103]. These results highlight both the sensitivity of TRPV channels to transient photothermal changes, and the safety margin provided by rapid dissipation dynamics.

TRPV4 is a voltage-gated calcium channel, as demonstrated by the loss of signal upon calcium channel blocking. Both mouse and human RGCs express TRPV4 (Figure 11), providing a scalable and clinically relevant target for vision restoration. By exploiting the efficiency of AuNR energy absorption, laser power requirements can be substantially reduced, confining heat generation to the nanoscale and lowering the risk of irreversible tissue damage.

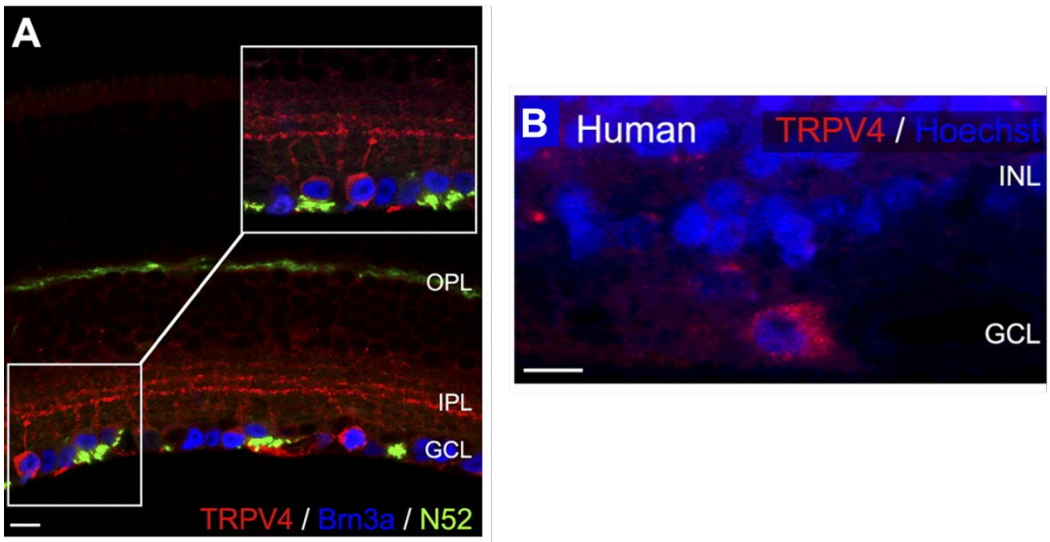

Figure 11 (A) Immunolabeling of TRPV4 channels in mouse RGCs, TRPV4 channels visualized in red, and Brn3a indicating RGCs in blue. (B) Human expression of TRPV4 in RGCs, TRPV4 channel shown in red, cells visualized using in blue using a Hoechst stain. TRPV4 visualized in red, Brn3a indicating RGCs in blue, and mouse anti-neurofilament in green. GCL: ganglion cell layer, OPL: outer plexiform layer, IPL: inner plexiform layer. Scale bar: 10 µm. Adapted from Albert et al. 2012 [114].

Our own functional study further validated this mechanism: AuNR-assisted NIR stimulation of retinal neurons produced Ca^{2+} influx and changes in membrane capacitance consistent with TRPV-mediated activation [117]. Temperature transients during stimulation were modest (3-8°C), sufficient to activate TRPV1 channels yet fully dissipate between pulses, preventing cumulative heating. To directly test the contribution of specific channels, we applied selective blockers: inhibition of TRPV1 markedly decreased Ca^{2+} responses, whereas TRPV4 blockade had little effect. These results support TRPV1 as the dominant mediator of neuronal activation under our stimulation conditions.

These findings demonstrate that the photothermal model relies on efficient delivery and safety of AuNRs within the retina. The findings from our experiments demonstrated that the capacitive currents and thermal effects together mediated

neuronal activation, without inducing thermal damage. This mechanism provides a foundation for developing safe and effective retinal prosthetic strategies.

1.2.3. Towards a high-resolution non-invasive retinal prosthesis

A photothermal plasmonic retinal prosthesis offers a novel approach to vision restoration that may overcome several critical limitations observed across current strategies, including gene therapy, optogenetics and conventional retinal prosthetics . While these methods have achieved varying levels of success, they each face challenges related to spatial precision, invasiveness, and long-term stability. Central to this approach is the use of AuNRs, which exhibit unique plasmonic properties enabling precise neural stimulation through photothermal mechanisms. By leveraging the LSPR of AuNRs, particularly within the NIR window, it becomes possible to activate retinal neurons with high spatial resolution and minimal invasiveness.

The primary advantage of this technique lies in its precision. Unlike electrode-based prosthetics, which are limited by the physical dimensions of the electrode arrays and the spread of electrical currents, photothermal stimulation via AuNRs targets neurons in direct proximity to the nanoparticles. With efficient targeting strategies, such as conjugation to ligands or antibodies specific to retinal neurons, this system has the potential to stimulate a broader and more relevant population of cells. This increased coverage could, in turn, improve the biological relevance of the artificial visual signal.

Moreover, compared to current subretinal or epiretinal electrode implants, the AuNR based approach offers a markedly less invasive installation method. AuNRs can be administered via intravitreal (IVT) injection, a routine outpatient procedure that avoids the need for invasive and costly surgical implantation. Once injected, the AuNRs can diffuse through vitreous humor and be directed towards the neural retina, where targeted binding and stimulation can occur. When the targeting moiety is efficient, a larger number of neurons can become stimulated by the NIR laser and subsequently enhance spatial precision and visual acuity. The tunability of AuNR optical properties, governed by their aspect ratio, allows precise control over their absorption peaks, ensuring that stimulation is triggered selectively by the NIR light without affecting surrounding tissue, a schematic of the PRP is shown in Figure 12.

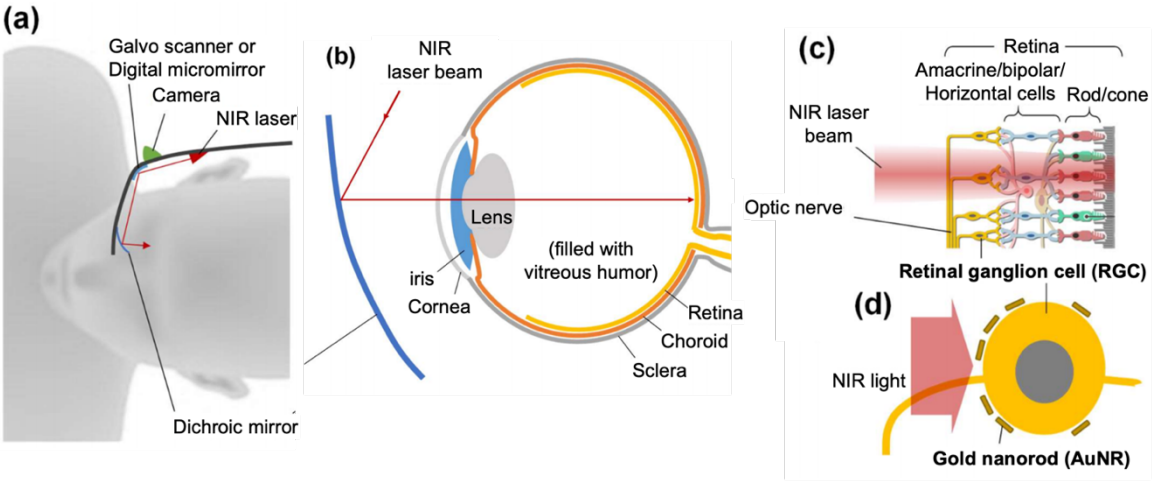

Figure 12 Schematic depiction of PRP, (a) displaying the external wearable portion consisting of a camera, NIR laser, galvo scanner, and mirrors to direct the NIR beam, (b) NIR beam entering the eye through the lens and reaching the retina, (c-d) NIR beam reaching inner retinal neurons and stimulating neurons with AuNRs attached to their plasma membranes.

An additional key benefit is the potential for single-neuron stimulation. The localized heating effect from NIR-induced plasmonic activation is confined to sub-micrometer regions [107], raising the theoretical possibility of stimulating individual neurons. Such resolution exceeds the limits of existing electrode-based methods, potentially enabling significant improvements in visual acuity in retinal prosthetic systems.

However, translating this theoretical advantage into a clinically viable prosthesis depends on two unresolved challenges: (1) achieving efficient and targeted delivery of AuNRs to the inner retina, and (2) establishing the long-term biosafety of ocularly administered AuNRs. Although gold is generally considered bioinert, the unique physiochemical properties of nanorods necessitate rigorous evaluation of their safety and potential systemic circulation following ocular administration. To advance the development of plasmonic retinal prostheses, it is therefore essential to characterize both their delivery efficiency and systemic impact.

1.3. Objectives of this thesis

The goal of this thesis is to explore the delivery efficiency and biosafety of IVT-delivered AuNRs in the context of plasmonic retinal prostheses. Specifically, my work aims to:

i. **Evaluate the efficacy of the intravitreal injection of AuNRs in mice** to determine its suitability to target inner retinal neurons for photothermal activation

ii. **Assess the systemic toxicity of IVT delivered AuNRs in mice** to determine their pre-clinical safety profile

2. Chapter 2: Intravitreal delivery of gold nanorods in mice[1]

2.1. Introduction

Intravitreal (IVT) delivery is one of the most common ocular delivery routes utilized. It directly deposits substances within the vitreous cavity. Utilizing it for the retinal delivery of AuNRs depends on their ability to diffuse to the retina. The vitreous humor (VH) is comprised of hyaluronan and collagen, and it is separated from the retina by a barrier known as the inner limiting membrane (ILM). The ILM is composed of fibronectin, proteoglycans, collagen, and laminin [118,119], a diagram of the vitreoretinal interface is shown in Figure 13. Subretinal delivery (SR), is also widely utilized to deliver substances to the retina wherein it deposits deliverables beneath the neural retina near the retinal pigmented epithelium (RPE). To reach their desired target site, substances must diffuse through the neuronal layers of the retina; a diagram depicting delivery routes is shown in Figure 14.

[1] A concise paper detailing the findings of this chapter can be found in DOI: 10.1021/acsnano.4c14061. H.A conducted all microscopic imaging (confocal and two-photon) and analyses, and co-designed delivery experiments

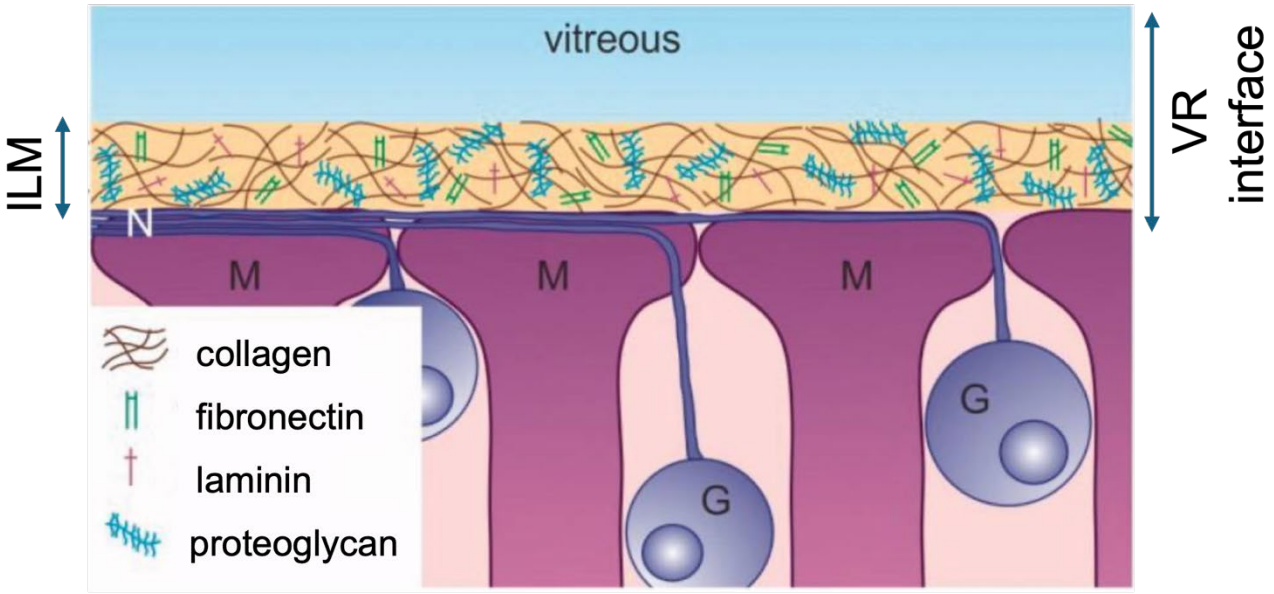

Figure 13 Diagram depicting the vitreoretinal interface, inner limiting membrane (ILM) and its components. M: Müller cells, G: retinal ganglion cells. Adapted from Peynshaert et al., 2017 [120].

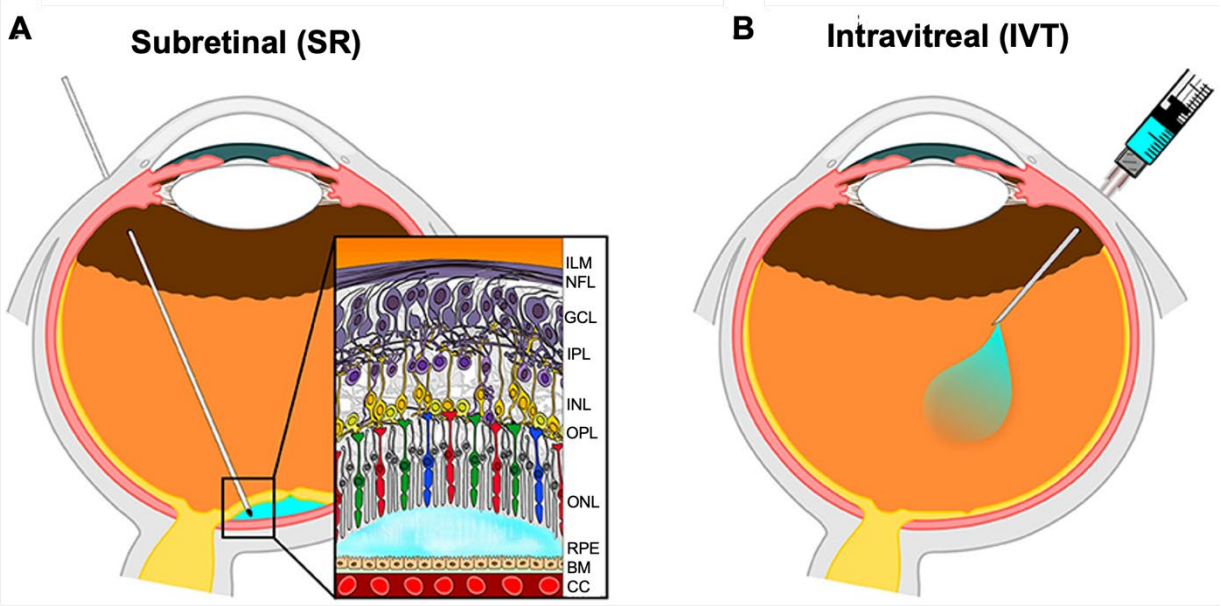

Figure 14 (A) Schematic of subretinal injection displaying the location of the injected material beneath the neural retina, (B) Intravitreal injection (IVT) which deposits injected material in the vitreous cavity. Adapted from Ochakovski et al., 2017 [121].

2.1.1. Approaches to ocular nanoparticle delivery and functional efficacy

Non-metallic nanoparticle (NP) delivery to the retina has been studied extensively, and their delivery profiles have been thoroughly characterized. Junnuthula et al, delivered polymeric nanoparticles of several formulations and sizes to the retina via the IVT route in rabbits and studied their retention time in the optic nerve head region [122]. The nanoparticles were characterized as polymersomes and polymeric micelles, with mean diameters of about 100-nm and 30-50 nm respectively. Their analysis indicated that polymersomes were found in the vitreous at least 92-days after the dose, and fundus imaging revealed that they had accumulated near the optic nerve head and remained until 111 days post-injection.

Elbedwehy et al, IVT delivered mesoporous silica NPs in efforts to reduce oxidative stress in an mouse model of optic nerve crush[123]. The nanoparticles were approximately 100-nm in diameter, and had a negative surface charge, they were detected in the vitreous at 7-days post injection (DPI) and had released their encapsulated drug facilitating its diffusion to the retina.

Ottoneli et al, injected a hydrogel containing hyaluronic acid (HA) coated NPs to achieve controlled release, and target the retina [124]. NPs were coated in HA to facilitate their movement throughout the vitreous and prevent protein corona formation. The nanoparticles were roughly 240-nm in size and negatively charged. Confocal microscopy conducted 24h later showed that uncoated NPs were mainly

localized at the injection site and were hindered by the positively charged components of the VH. In contrast, HA coated NPs with a negative charge were found distributed in retinal layers, namely the outer plexiform layer (OPL) and the inner nuclear layer (INL).

Previous examples of non-metallic nanoparticles suggest a size-dependent retention of NPs within the eye, specifically in the VH. However, studies utilizing non-metallic NPs are concerned with drug-release where the particles are designed to disassemble over time releasing their contents in a time-dependent manner. Conversely , gold-nanoparticles (AuNPs) may either diffuse to the retina or become cleared through the VH clearance pathways.

Sandrian et al. IVT delivered gold-nanorods (AuNRs) in mice, to examine their use as photo-contrast agents, and determine their suitability for radiotherapy use [125]. They observed AuNRs in the vitreous at 30m post-injection, and at 24h they located them at the vitreoretinal (VR) interface. Through TEM analysis, they identified AuNRs that had been phagocytosed at the VR interface, and others that had not diffused to the retina at the ILM, as shown in Figure 15. AuNPs in this study were rod-shaped, and were conjugated with a Thy-antibody, yet their size was not disclosed. Although, this study sheds light on the prominence of the ILM, and the potential for AuNPs to become detected and engulphed by the reticuloendothelial system (RES) even as early as 24h post-injection.

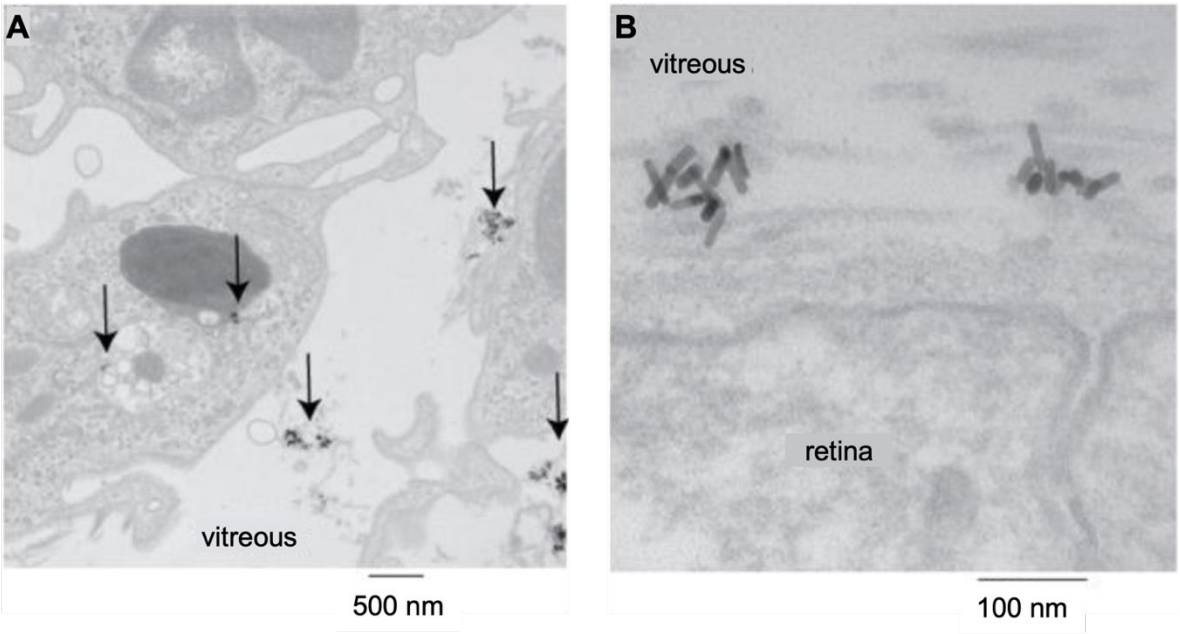

Figure 15 TEM images of mouse retinas injected with Thy-AuNRs. (A) shows phagocytosed AuNRs, and (B) shows AuNRs at the ILM junction. Adapted from Sandrian et al., 2012 [125].

Roh et al. determined the ability of 20-nm AuNPs to reduce choroidal neovascularization (CNV), a hallmark of neovascular AMD leading to the severe irreversible reduction of vision loss, they IVT delivered their NPs 24h after experimentally inducing CNV [126]. They sacrificed their animals at 7 DPI and examined retinal flat mounts; results indicated a significant reduction of the extent of CNV compared to controls. This study did not provide further information regarding the migration of the particles past the ILM, nor any further characterization of delivery dynamics. Similarly, Kim et al. demonstrated the ability of IVT delivered 20-nm AuNPs in suppressing the vascular endothelial growth factor (VEGF) pathway to reduce retinal neovascularization (RNV) [127]. They did not provide any further information about particle shape, nor delivery dynamics. Yet, they concluded that the IVT method was sufficient for retinal delivery.

Batabyal et al. IVT delivered light-sensitive opsins enhanced by AuNRs to the retinas of *rd10* mice [128]. They utilized the properties of localized surface plasmon resonance (LSPR) to exploit localized heating to enhance membrane permeability of molecules. The AuNRs in this study were 10-nm in diameter and 40-nm in length and conjugated with Concanavalin A (ConA), a lectin that irreversibly binds to glycoproteins on the cell surface. They delivered their opsin and AuNRs via the same IVT injection and compared the transfection of retinal areas that received near infrared (NIR) irradiation to those that did not. Results showed a significant difference between the irradiated and non-irradiated zones.

Retinal explant imaging showed transfection and expression of the opsin in the GCL layer 7-days after intravitreal injection. This study examined the benefits of exploiting the LSPRs of AuNPs in enhancing cellular delivery through optoporation techniques. The AuNRs were not visualized through confocal analysis, as they were not fluorescently tagged, and no further characterization of delivery dynamics nor cellular distribution was provided. It is unclear whether AuNRs reached the retina, or if the NIR irradiation itself improved the penetration of vectors to the cells without the assistance of AuNRs.

Wilson et al., similarly, utilized LSPRs of AuNPs to enhance retinal permeation, with modifications to the approach by Batabyal et al. They utilized antibody-conjugated AuNPs that would enhance the targeting of RGCs, and demonstrated the attachment of target AuNPs compared to non-targeted (bare) AuNPs [129]. They conjugated 100 nm AuNPs (likely spherical shaped, unspecified in the study), to K_v1.1 antibodies (Ab) and delivered IVT, optoporation experiments

were conducted *in-vivo* and confocal imaging optoporation examination was conducted 1-week after IVT injection and irradiation. Experiments concerning the localization of AuNPs within the RGC line were conducted *ex-vivo* on retinal explants. Briefly, they applied 5µL of bare AuNPs or K_v1.1-AuNPs on retinal explants and incubated them for up to 5h, before washing and conducting confocal microscopy.

This type of experimental procedure while successful in highlighting the theoretical binding capability of the K_v1.1 Ab, does not clearly indicate the performance of this Ab in conjunction with AuNPs *in-vivo*. The *in-vivo* data obtained merely provided insights into the optoporation efficiency and safety but did not provide enough details regarding layer specific distribution, nor whether particles diffused through the ILM. The research provides a proof-of-concept for optoporation techniques, and an RGC targeting moiety, yet still lacks relevant *in-vivo* targeting and layer related information.

Song et al. intravitreally delivered gold nano-disks (AuNDs) to evaluate their anti-angiogenic effects in inhibiting RNV [130].They used 160-nm sized AuNDs and imaged the vitreous using optical coherence tomography (OCT) post-injection. Results from the AuND group were compared to eyes that received saline, they showed high levels of OCT signal while the saline group showed minimal OCT signal. Interestingly, their results also indicated that AuNDs did not accumulate at the ILM at any of the time points examined (6h, 2, 7 and 14 DPI).

At 14 DPI, no AuNDs were detectable in the VH, whereas they were dispersed throughout the vitreous at 6h. By 2 DPI, retinal clearance of the AuNDs

was observed as very few remained within the vitreous. There are two pathways for clearance, the anterior relies on aqueous flow to the trabecular meshwork, while the posterior elimination pathway relies on diffusion through the retina to the choroid because of hydrostatic and osmotic pressure changes within the posterior segment of the eye [131].

Ocular clearance strategies are closely related to particle size and surface chemistry [132–134]. Raju et al. showed that 50-nm magnetic NPs were undetectable after IVT injection when examined at 5 weeks post-injection, while 4-μm particles remained detectable [133]. The 50-nm particles were detected on the adjacent surface of the retina and lens at 1 DPI, gradually decreasing by 1-week and became undetectable even with magnetic resonance imaging (MRI) of organs. Koo et al. demonstrated a clearance pattern dependent on surface chemistry when IVT delivering 200 to 330-nm-sized polymeric NPs [134]. They delivered a total of seven particle types each with different surface chemistries but with comparable sizes and fluorescent tags to visualize them confocally.

Of the particles used, HA coated particles (213-nm) were seen in all retinal layers, with a significant reduction after 72h, with only sparse particles found at the ganglion cell layer GCL and inner plexiform layer (IPL). Human serum albumin (HSA) coated particles (326-nm) also experienced this enhanced retinal penetration, and authors conducted additional staining procedures to label Müller cells, and observed co-localization of particles and Müller cells, suggesting that particles may use them as a pathway to penetrate the ILM, depicted in Figure 16. Interestingly, glycol-chitosan (GC) coated NPs with a size of 230-nm and a positive charge were not able to penetrate the ILM and remained at the VR before gradually being cleared from the ocular space at around 72h. Evidence from this study suggests that while size and physical characteristics can play an important role in distribution and clearance, retinal penetration may rely more on surface chemistry.

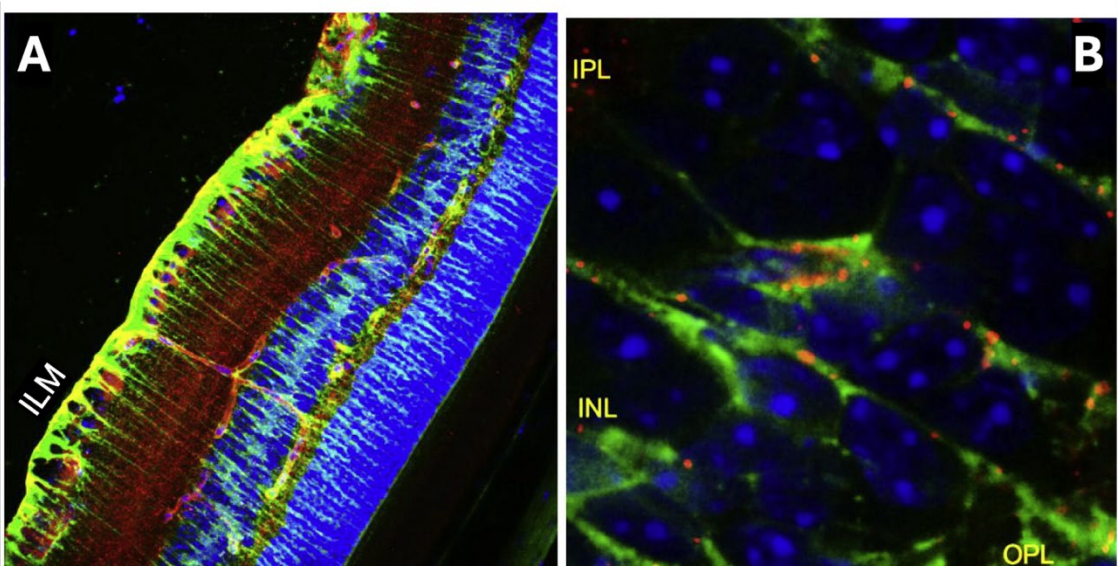

Figure 16 Vitreal and retinal distribution of IVT administered HSA nanoparticles, (A) co-localization of IVT HSA particles (red) and Müller cells (green) in the whole retina. (B) detailed co-localization following retinal penetration of HSA nanoparticles (red) and Müller cells (green) around the INL and OPL. ILM: inner limiting membrane, INL: inner nuclear layer, IPL: inner plexiform layer, OPL: outer plexiform layer. Figure adapted from Koo et al., 2012 [134].

Some studies that have delivered AuNPs to the eye have not provided adequate details of their NP characteristics, regarding shape, size and chemical properties. The data concerning distribution of the particles in the ocular space, and their visualization is still severely lacking. Partly due to the differing scope of each study, and the focus when it comes to AuNPs towards the inhibition of CNV and RNV [126,127], optoporation techniques [128,129], or theranostic/imaging applications [125–127,130], rather than characterizing delivery and retinal distribution. Yet, AuNPs offer an exciting new stimulation modality due to the LSPR phenomenon, beckoning further investigation of its efficient retinal penetration and distribution to support the development of a photonic retinal prosthetic (PRP).

2.1.2. Unanswered questions

While the previous examples provide worthy insights into the efficacy of IVT injection, and the feasibility of AuNPs to distribute within the VH, there has been a lack of data that would suggest AuNPs can definitively diffuse through the ILM and disperse within relevant retinal neuronal cell lines. For the purposes of our PRP, we require that (1) AuNRs diffuse through the VH and ILM, (2) reach relevant retinal neurons, (3) bind to the plasma membranes of retinal neurons, and (4) remain bound for as long as possible post-injection, as this can reduce the need for frequent re-injection.

Related to these requirements, Sandrian et al.[125], was able to show that as early as 24h post-injection, AuNRs were found at the VR interface and were blocked from diffusing past the ILM. Beyond that information, no other study has directly characterized nor visualized AuNPs within the retina. Song et al, showed

that AuNDs were dispersed within the VH, but then began to clear out and none remained within the VH after 14 DPI. They did not provide further information regarding retinal penetration. Other studies have provided indirect evidence, that would suggest that AuNPs managed to diffuse through the ILM and exerted their effects within the retinal space.

For example, studies concerned with CNV and RNV suggested that AuNPs reduced the extent of neovascularization [126,127,130], optoporation studies managed to show retinal expression of the delivered vectors, without characterizing AuNP presence [128,129]. And NP clearance studies have suggested potential clearance pathways of NPs more generally [132–134], and have provided a potential conduit for diffusion through the ILM via Müller cells [134]. Yet, ILM circumvention methods such as mechanical or chemical could be utilized in improving ILM penetration. Furthermore, it is unclear how the size of AuNPs may harm or enhance their retinal diffusion abilities.

Recently, a study has shown improved ILM penetration and viral vector gene transfection using glycosidic enzymes [135]. Cehajic-Kapetanovic et al. examined the use of various enzymes that work to degrade either components of the VH, or components of the ILM. Their results indicated that the combination of two, hyaluronan lyase and heparinase III, led to significantly improved viral transfection rates throughout the entire retina. Hyaluronan lyase exerts its effects on components of the VH, while heparinase III can exert its effects on heparin sulfate, heparin and the proteoglycans within the ILM. The safety of this approach was demonstrated up to 12-months post-injection in mice. Utilizing this strategy, might

maximize the retinal diffusion of AuNRs, and mitigate the rapid clearance effects that were observed by Song et al. in the delivery of their AuNDs[130].

Batabyal et al. suggested the efficacy of Ab-conjugated AuNPs in improving specificity to retinal neurons, they utilized K_v1.1 Ab and demonstrated its efficacy *ex-vivo* in labeling the RGC layer [128]. Thy-1 is an antigen known to localize to the surface of several retinal neurons located within the RGC layer, and the IPL [136,137], allowing the targeting of bipolar cells (BCs), further enhancing the biological relevance of the artificial vision signal initiated by the PRP. Therefore, it is possible to conjugate Thy Ab to AuNRs and potentially lead to their preferential binding to plasma membranes, a core need for the PRP. Thy distribution in the retina is shown in Figure 17.

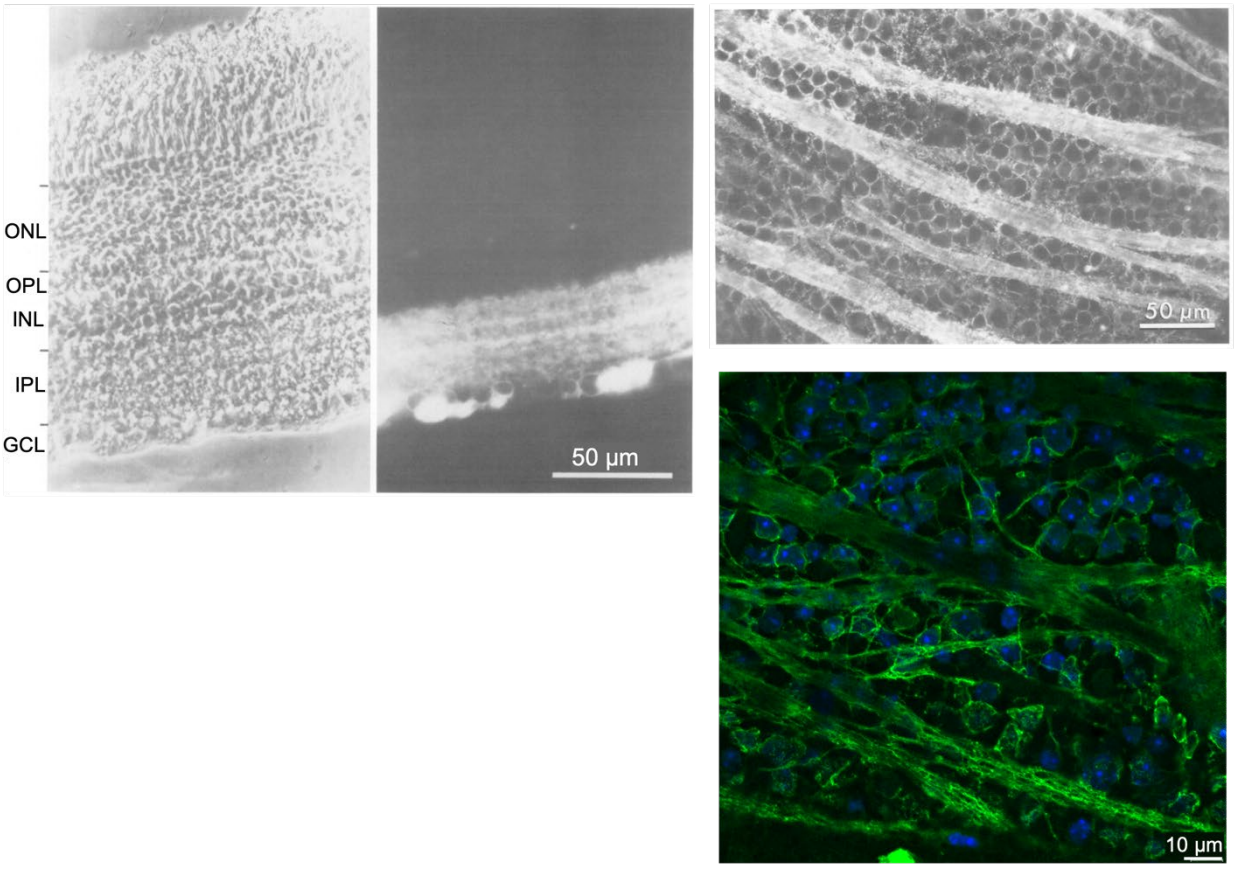

Figure 17 Fluorescent labeling of adult mouse retina showing Thy-antigen localization in the retina in the IPL and GCL (top left), cross sectional image taken at the GCL layer showing membrane labeling and nerve fiber bundles by Thy-antibody (top right), fluorescent confocal en-face image showing the GCL labeling of Thy-antibody; conducted to verify Thy localization demonstrated by Barnstable and Dräger. (bottom right) We utilized biotinylated Thy-antibody and FITC-streptavidin dye (green), cell nuclei stained with DAPI (blue). ONL: outer nuclear layer, OPL: outer plexiform layer, INL: inner nuclear layer, IPL: inner plexiform layer, GCL: ganglion cell layer. Figures adapted from Barnstable and Dräger [136].

Taken together, the information has prompted the development of the following hypotheses to investigate the unanswered questions for the development of the PRP:

1a) IVT injection effectively delivers AuNRs to the retina through the VH and ILM

1b) Enzymes degrade the ILM and enhance AuNR diffusion to the retina

1c) Anti-Thy conjugation increases the amount of AuNRs in the retina

1d) The size of AuNRs does not alter the retinal diffusion of AuNRs

1e) IVT delivered amount of AuNRs decreases with days post injection (DPI)

1f) IVT injected Thy-AuNRs are distributed both in the GCL and IPL

My research and experiments were specifically designed to test these hypotheses.

2.2. Materials and methods

2.2.1. Gold nanorods (AuNRs)

Gold nanorods (AuNRs) were obtained from Nanopartz (Loveland, CO, USA; Lot # N1970), synthesized via the company's proprietary method. Three types of AuNRs were acquired: 10 nm and 25 nm variants conjugated to Thy-1 antibodies, as well as 25 nm bare AuNRs with no surface functionalization. Nanopartz supplied comprehensive characterization data, which included physical dimensions, surface plasmon resonance (SPR) spectra, zeta potential values, and antibody conjugation metrics. Additional validation of the AuNRs was performed using transmission electron microscopy (TEM), dynamic light scattering (DLS), and UV-visible spectroscopy. Antibody conjugation (Anti-Thy-1) was performed in-house by the supplier and verified prior to shipment. AuNR suspensions were kept at 4°C

in light-protected containers until use. All experimental work was carried out using consistent batches.

Specifically, the 25 nm Thy-1 AuNRs exhibited an SPR peak between 975–995 nm, had a neutral pH of 7, a zeta potential of –23 mV, and a particle concentration of 3 × 10^{12} nanorods/mL (5 nM), with an average of 105 Thy-1 molecules per nanorod. The 10 nm Thy-1 AuNRs had an SPR range of 985–990 nm, zeta potential of –26 mV, identical Thy-1 loading (105 per particle), and a higher concentration of 2.3 × 10^{12} nanorods/mL (39 nM). The unmodified 25 nm AuNRs had an SPR peak between 970–990 nm, zeta potential of –18 mV, and the same particle concentration as the larger Thy-1 conjugated AuNRs.

2.2.2. Intravitreal injection

Commercial gold nanorod (AuNR) solutions were obtained from Nanopartz (Loveland, CO, USA; Lot # N1970) and used for intravitreal injection. Each mouse eye received 0.5 µL of solution (1.0 µL per animal), corresponding to doses of 150 µg/kg for females and 100 µg/kg for males, based on a working concentration of 5 nM. Injections were performed using a modified version of established intravitreal protocols [138,139]. Mice were anesthetized using isoflurane (1–5%), and pupils were dilated with 1% atropine drops. Lubricating ointment was applied as needed to protect the cornea. With the eye gently stabilized using forceps, a 28-gauge needle was used to make a limbal puncture under a microscope. Through this entry site, a blunt 33-gauge sub-microliter injector delivered 0.5 µL of either AuNR solution or sterile PBS at a 45° angle into the vitreous.

The 5 nM AuNR concentration represents the highest formulation reliably supplied by Nanopartz that is suitable for intravitreal use and was selected to ensure consistent performance across experimental runs. This concentration is currently being used in parallel studies focused on targeted neuronal interaction and photothermal activation in the retina. Using the manufacturer's highest available concentration enables maximal exposure and offers a stringent model for evaluating potential systemic toxicity.

According to supplier characterization, each Thy-1–conjugated AuNR carries approximately 105 antibodies per particle. Given that a typical IgG has a molecular weight of ~150 kDa, this increases the total nanoparticle mass by only 2–3% relative to the gold nanorod core (estimated at 6.8×10^8 Da for the 25 nm variant). As such, the effective dose for Thy-1-conjugated AuNRs was calculated to be 150 µg/kg for females and 100 µg/kg for males, while the bare (unconjugated) AuNRs were administered at slightly lower mass to account for the absence of antibody.

To standardize intraocular exposure across sexes, both male and female mice received the same injection volume. Although males tend to have greater body mass, the functional target—retinal surface area—does not differ significantly between sexes in adult mice, as previously reported by Zhou and Williams [140]. Therefore, fixed ocular volumes better reflect clinically relevant dosing strategies, which are typically based on eye anatomy rather than systemic weight.

2.2.3. Funduscopy examination pre-, and post-injection

To assess for post-injection hemorrhage, fundus images were acquired both prior to and following intravitreal administration using the Phoenix Micron 5 fundus imaging system (Phoenix, Bend, OR). A 3 mm cover glass was placed over the eye, and any signs of vitreous hemorrhage were assessed. Any animals presenting with observable hemorrhage were excluded from subsequent analyses. Animals were kept on a heated pad during and after the procedure to maintain body temperature.

2.2.4. Enzyme solution

Heparinase III and Hyaluronan lyase were commercially sourced (Millipore Sigma, Burlington, MA) and reconstituted in sterile PBS solution. We extracted approximately 0.125 sigma units per enzyme (0.25 µL each) and combined them prior to the IVT injection. We administered a combination of 0.5 µL of the enzyme solution and 0.5 µL of the AuNR solution for a total of 1.0 µL.

2.3. Quantitative assessment of the delivered amount with two-photon luminescence microscopy

2.3.1. Two-photon luminescence: physical concept and phenomena

Two-photon luminescence (TPL) has become an increasingly valuable tool for visualizing AuNPs. This technique leverages the same optical resonance principle used in photothermal stimulation: when gold nanostructures are irradiated at their

localized surface plasmon resonance (LSPR) frequency they can emit optical signals. There is still debate in the literature regarding the origin of this signal. One hypothesis suggests the emission arises from enhanced scattering and absorption by the AuNPs, while another proposes that gold exhibits intrinsic photoluminescence under resonant excitation. Regardless of the underlying mechanism, luminescence occurs only upon absorption of photons at sufficient intensity [141]; this luminescence phenomenon is depicted in Figure 18.

Two-photon microscopy (TPM) offer significant advantages over conventional confocal microscopy, particularly for deep-tissue imaging. It improves image contrast by eliminating out-of-focus excitation and does so without requiring a physical pinhole. Instead, the fluorescence arises from superlinear (quadratic) dependence on excitation light intensity, allowing for spatially confined excitation in three dimensions [142].

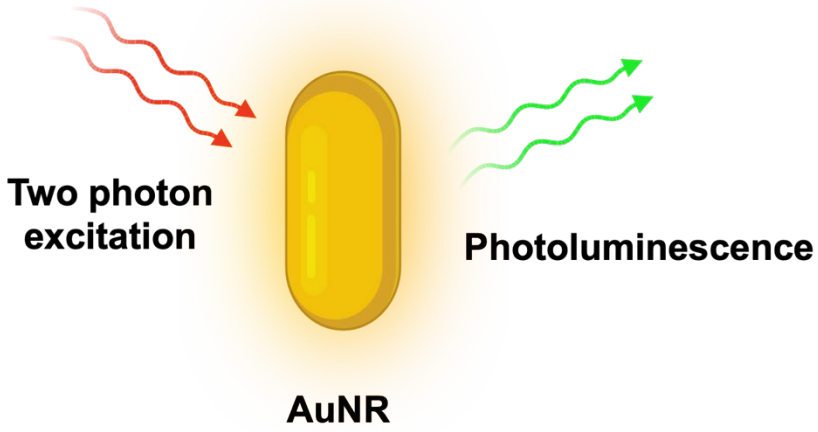

Figure 18 Schematic representation of two-photon luminescence of a gold nanorod.

TPL is typically excited using femtosecond pulsed lasers, such as a Ti:Saphire source tuned to near-infrared wavelengths suitable for two-photon absorption. Z-scan techniques can be used in parallel to quantify nonlinear optical properties such as absorption and refractive index [143].

AuNRs are especially well-suited for TPL imaging due to their high two-photon (2p) absorption cross section. Their photoluminescent signal can be over 50 times more intense than conventional fluorophores such as rhodamine [144]. TPL microscopy enables the detection and quantification of AuNRs in retinal tissue following IVT injection. Due to the intrinsic photoluminescent signals of AuNRs, no external labeling or fluorophores are required, which can allow for more targeting molecules to bind to the surface of AuNRs without competing for space with other labeling molecules. The spatial confinement of the signal translates into a potential for cell-layer specific quantification.

2.3.2. TPL imaging of gold nanorods: previous studies

AuNRs have been utilized in two-photon microscopy for their high-resolution imaging, and cross functionality in photothermal applications. In one example, Li et al. developed ~10 x 36 nm AuNRs functionalized by polyethylene glycol (PEG) for biocompatibility and conjugated with transferrin (Tf) to enable targeting of cancer cells via transferrin receptor-mediated uptake [145]. These targeted AuNRs produced two-photon luminescence signals with a 100-fold higher excitation-cross section than the commonly used fluorophore fluorescein isothiocyanate (FITC), significantly enhancing spatial resolution. Upon femtosecond laser irradiation (800 nm wavelength, 50 mW power) apoptosis was selectively induced in cells

containing Tf-AuNRs, while no such effect was observed in cells lacking these nanoparticles under identical conditions. Although their work focused on tumor models, it underscores the utility of 2p imaging for precise localization of AuNRs in tissue, supporting our use of two-photon microscopy in retinal applications.

In a separate study, Suarasan et al. investigated the intracellular tracking of gelatin coated AuNPs with varying shapes and sizes, specifically Au spheres (AuNS) 69-nm diameter, rods measuring 12 nm x 41 nm, and triangular AuNTs with edge lengths of 172-nm, in ovarian cancer cells. Using TPL and fluorescence lifetime imaging microscopy (FLIM), they demonstrated the feasibility of imaging and tracking AuNPs within different microenvironments. Scattering signals were observed within the cytosol but outside nuclei, confirming internalization and extranuclear localization. Notably, high-quality imaging was achieved with low laser intensities (~0.5 mW), highlighting the potential for minimally invasive visualization. This work reinforced the utility of TPL for label-free tracking of plasmonic nanostructures under biologically safe near infrared (NIR) irradiation.

While both representative studies are centered on oncologic applications, they collectively demonstrate the precision and sensitivity of two-photon imaging for detecting AuNPs in complex biological environments. This supports our rationale for employing TPM to localize AuNRs in retinal tissue, where anatomical complexity and spatial specificity are equally paramount.

2.3.3. Establishment of imaging protocols

The previous studies demonstrate that TPL imaging can effectively detect AuNPs by utilizing their intrinsic photoluminescent signals. However, these studies also highlight the technique's sensitivity to imaging parameters such as laser power and alignment. Excessive excitation can result in photothermal artifacts or nonlinear scattering, complicating signal interpretation. Moreover, the nonlinear nature of TPL signal generation necessitates consistent imaging settings to enable reliable comparisons across samples.

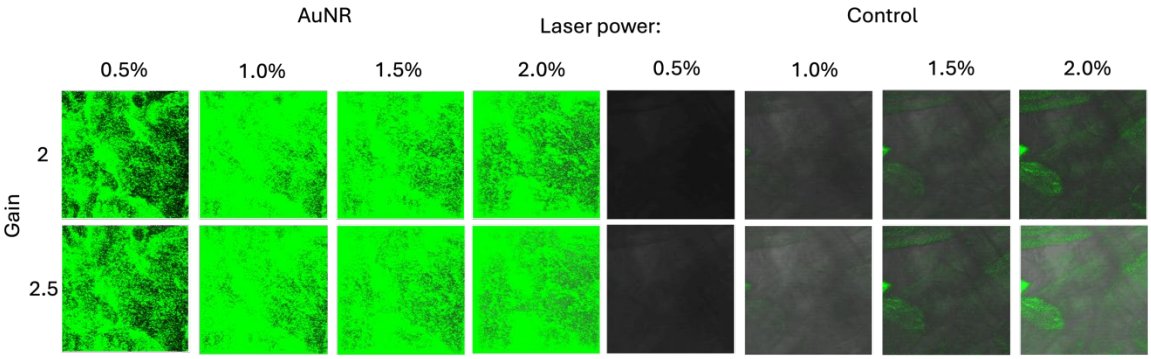

Figure 19 TPL imaging parameter optimization on filter paper samples containing 1µL of AuNR solution. Laser power is displayed above the column of images and gain is displayed per row of images, (top row) 2.0 digital gain setting, (bottom row) 2.5 digital gain setting. Laser power displayed as a percentage of 3.06W.

To address these limitations, we conducted multiple iterative rounds of signal optimization to establish a robust and reproducible set of imaging parameters for quantifying AuNR TPL signals in retinal tissues following IVT administration. We began our optimization experiments to determine laser power and detector gain. As part of our optimization, we evaluated multiple laser powers and detector gain settings using two sample types: filter paper loaded with AuNR

solution and filter paper without AuNRs as a control. A representative result from this comparison is shown in Figure 19.

Next, we examined signal intensity at the LSPR band specified by the manufacturer (780-nm), using the AuNR-loaded filter paper. We systematically varied excitation wavelength above and below the resonant frequency while keeping detector gain constant, to assess how off-resonant excitation affects signal output. These results are presented in Figure 20.

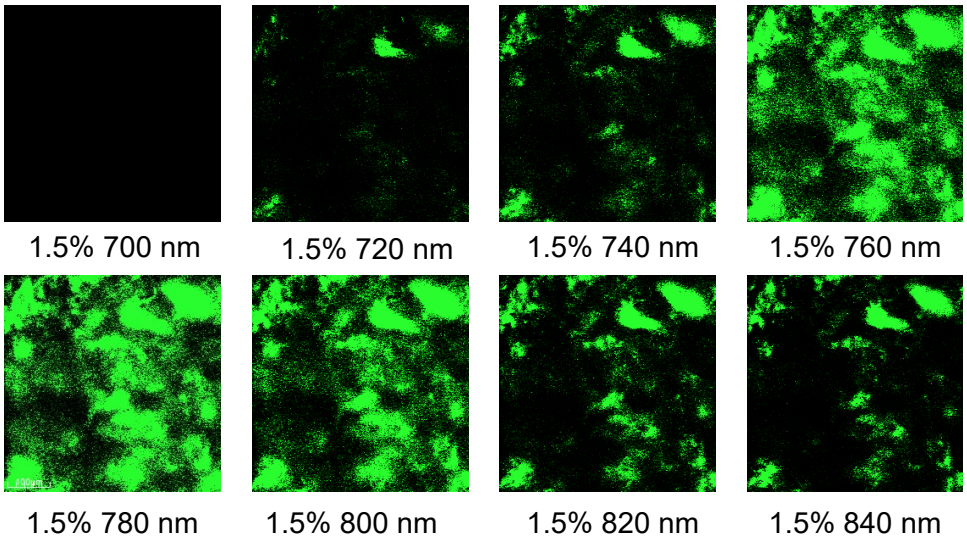

Figure 20 Exemplar images displaying the off-resonant TPL signal intensity of filter paper samples containing 1µL of AuNR solution, with laser power similar to that in Figure 19.

We then compared AuNR, and control samples imaged at the resonant excitation wavelength (780 nm) and at a longer, non-resonant wavelength (1080 nm). Comparative images illustrating this wavelength-dependent signal behavior are shown in Figure 21.

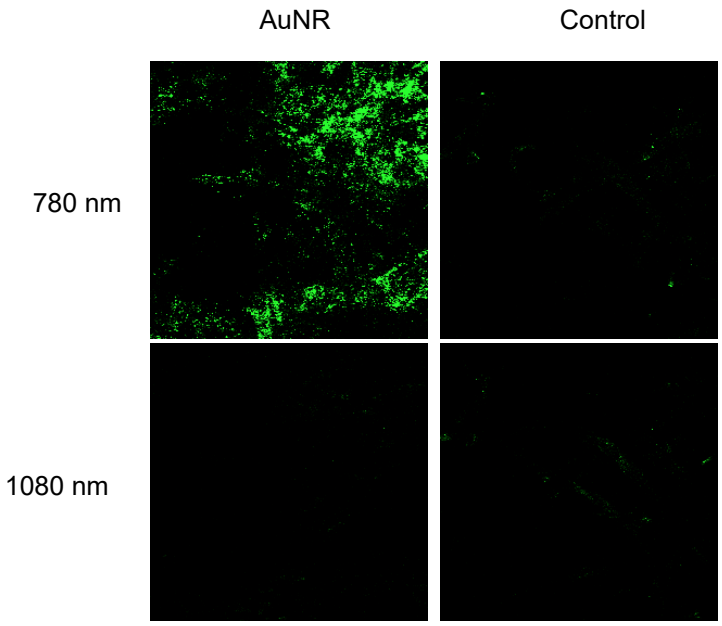

Figure 21 Exemplar images displaying the off-resonant TPL signal intensity of filter paper samples containing 1µL of AuNR solution, laser power of 1.5%.

Upon reviewing the results acquired from the optimization trials, we determined that a laser power of 1.5% (0.045W), and detector gain of 700 (Hv value; digital gain of 2.0) provided the best balance between signal intensity and background noise for TPL-based AuNR quantification. With these parameters established, we proceeded to finalize the retinal imaging protocol. This included performing unstitched tile scans and optimizing the field-of-view (FOV) to ensure consistent spatial coverage and reliable signal acquisition across the retinal surface.

Initially, we acquired 49 tiles in total (256 μm x 256 um per tile) spanning a total area of approximately 1.7 mm x 1.7 mm, with a 256-μm depth (Z-step: 1 μm). This process required approximately 3 hours per retinal sample. To improve throughput and enable imaging of multiple samples within a practical timeframe, we reduced the tile count to 25, adjusting the FOV to 1.3 mm x 1.3 mm, reducing acquisition time to approximately 2 hours. The 1-μm Z-step was retained to satisfy Nyquist sampling criteria, ensuring adequate axial resolution for resolving fine retinal features and accurately localizing AuNRs distributed across layered microenvironments. Representative images resulting from this process are shown in Figure 22 and in Figure 23.

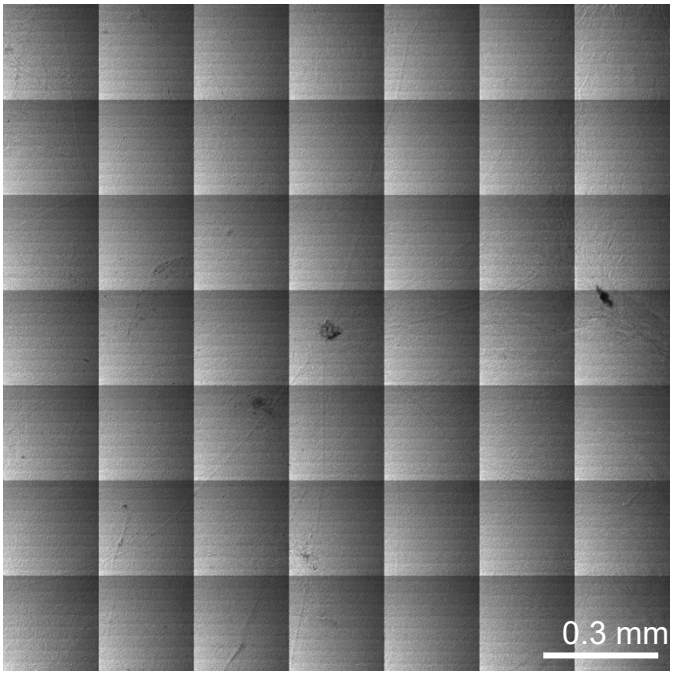

Figure 22 TPM brightfield image of initial retinal imaging protocol, a 7x7 grid spanning 1.7 mm x 1.7 mm.

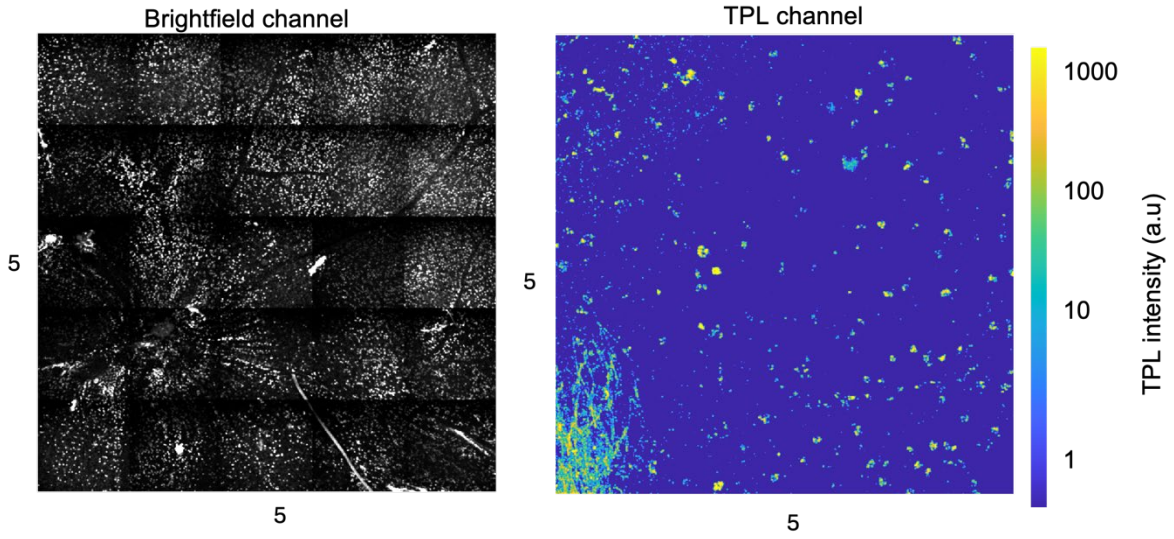

Figure 23 Exemplar image of final TPL imaging protocol, (right) shows TPL intensity map, (left) shows greyscale brightfield TPM image, 5 x 5 grid, 1.3 mm x 1.3 mm; TPL intensity legend displayed in arbitrary units.

2.3.4. Study design to evaluate our hypotheses

Hypotheses 1a-1b

With the imaging parameters and acquisition settings established, we next designed a systematic study to evaluate AuNR localization and signal distribution in retinal tissue following IVT injection. We first hypothesized that IVT injection delivers AuNRs effectively to the retina through the VH and ILM, and that enzymatic degradation of the ILM enhances AuNR diffusion into retinal tissue. To test these hypotheses, we conducted two experimental comparisons. In the enzyme group (n=8 retinas), 25-nm AuNRs conjugated to the Thy-1-antibody (henceforth: Thy-AuNRs) were co-injected with a combination of heparinase III and hyaluronan lyase to degrade the ILM. In the AuNR-only group (n=8 retinas) 25-nm Thy-AuNRs were injected without enzymes. A third sham group (n=8 retinas) only received phosphate-buffered saline (PBS). Animal numbers per group were determined based on a power analysis where previously published literature values were utilized to estimate the minimum detectable standardized difference in response. All groups were analyzed at a common timepoint of 8 days-post-injection (DPI). A schematic of the overall design is presented in Figure 24.

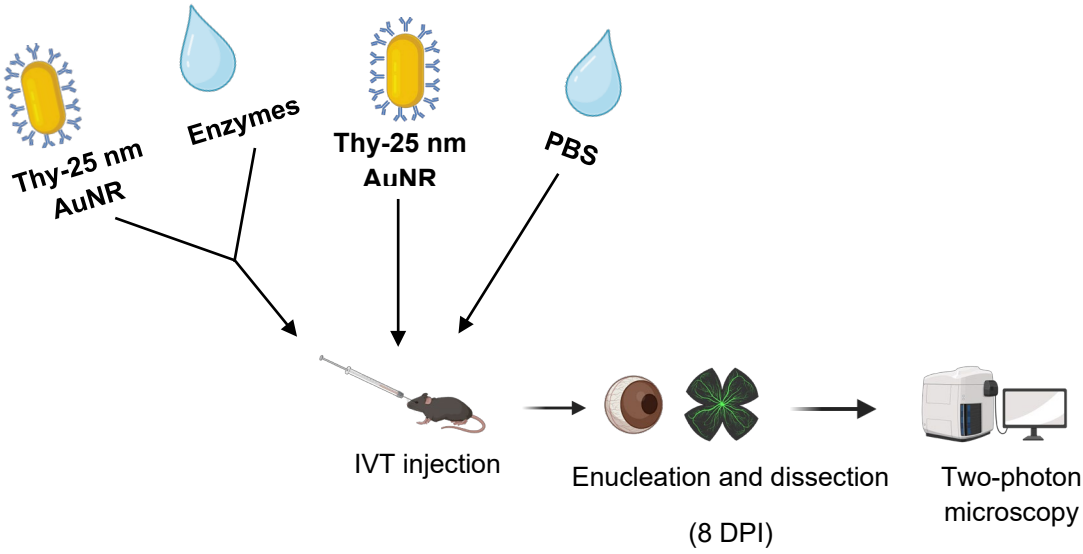

Figure 24 Schematic representation of the study design to examine hypothesis 1a and 1b, effect of enzymes on retinal accumulation of AuNRs. Each arrow represents a separate injection for individual groups, 25-nm Thy-AuNRs were co-injected with enzymes for the enzyme group.

Hypotheses 1c-1d

Next, we designed a set of experiments to evaluate whether Thy-antibody conjugation enhances AuNR accumulation in the retina as a function of Thy-conjugation and size. We also assessed the specificity of Thy-mediated targeting by including a validation control group. In the default AuNR group (n=8 retinas) 25-nm Thy-AuNRs were IVT injected. In the bare-AuNR group (n=8 retinas) 25-nm bare-AuNRs with no surface conjugation were injected. Both groups were analyzed at 32 DPI to evaluate the contribution of Thy-conjugation to retinal accumulation.

To assess the effect of AuNR size and validate Thy-targeting specificity, three additional groups were evaluated at 8 DPI: (1) the small-AuNR group (n=8

retinas), which received 10-nm Thy-AuNRs, (2) the default-AuNR group (n=8 retinas) which received 25-nm Thy-AuNRs, and (3) the Thy-antigen blocking control group (n=8 retinas), in which 25-nm Thy-AuNRs were pre-incubated with soluble Thy-antigens prior to injection, reducing their binding availability *in-vivo*. TPL signal intensity served as the quantitative metric for AuNR accumulation. This full experimental layout is summarized in Figure 25.

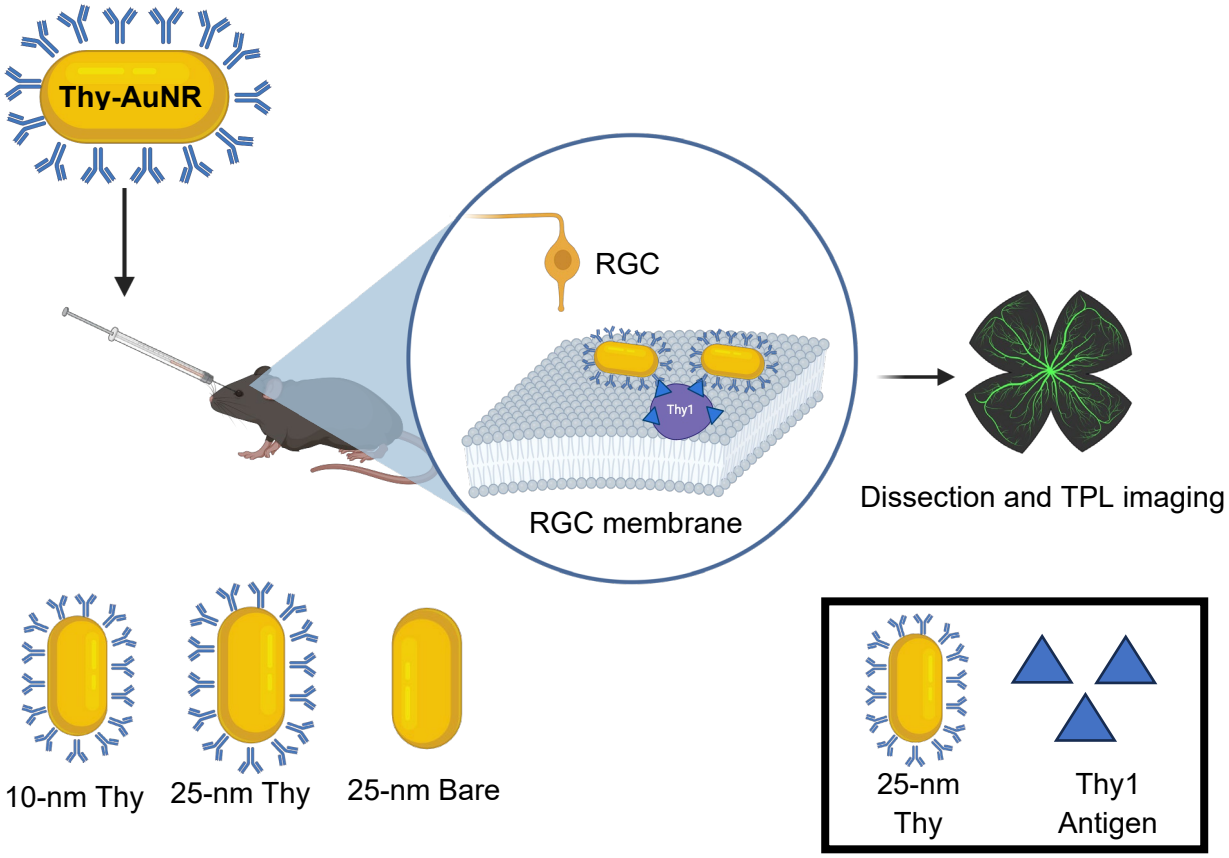

Figure 25 Schematic of study design for hypothesis 1c-1d, effects of size and conjugation on retinal accumulation of AuNRs; Thy-antigen validation control was a separate group.

Hypothesis 1e

To determine the persistence of AuNRs in the retina over time, we conducted a longitudinal experiment measuring TPL signal intensity across a 134-day period. A single experimental group received 25-nm Thy-AuNRs via IVT injection, with retinal tissues collected and analyzed at 2, 8, 31, and 134 DPI (n=8 retinas per time point). This time course enabled us to assess changes in TPL signal intensity and estimate the effective half-life of AuNR-associated TPL signal in the retina. A schematic of this experimental design is shown in Figure 26.

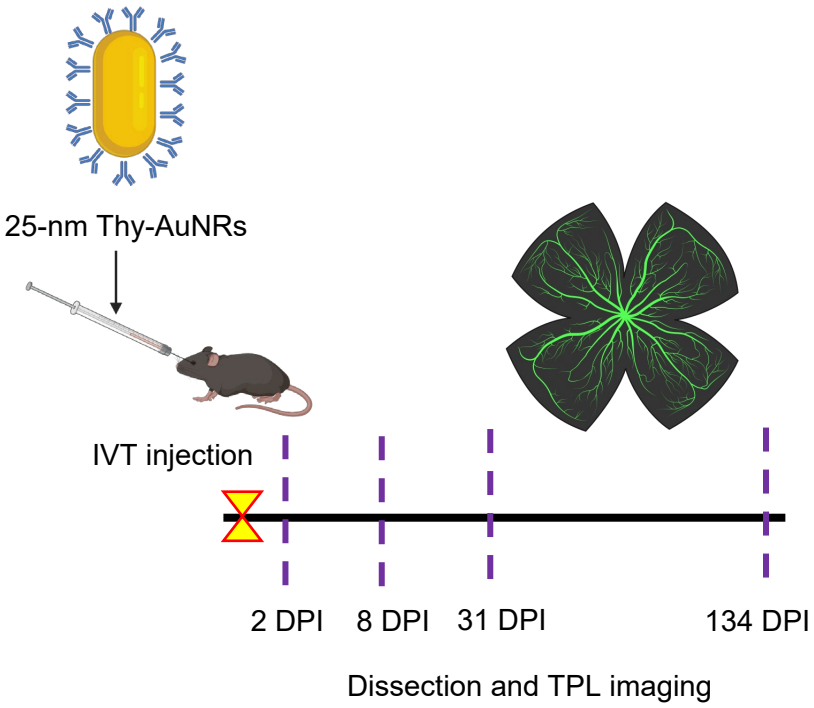

Figure 26 Schematic of study design to evaluate hypothesis 1e, effect of DPI on AuNR accumulation in the retina.

Hypothesis 1f

To evaluate the spatial distribution of AuNRs within the retina and confirm their localization within specific retinal sublayers, we employed 25-nm Thy-AuNRs conjugated with a fluorescent tag (Alexa fluorophore 488) to enable high-resolution visualization. Following IVT injection, eyes were collected at 8 DPI and DAPI was applied to dissected retinae for cellular visualization, we then performed confocal microscopy on retinal flat mounts. Imaging was conducted across multiple z-planes to assess the vertical distribution of fluorescence within the retinal architecture. Particular attention was given to the ganglion cell layer (GCL) and the inner plexiform layer (IPL) where Thy-antigens are predominantly expressed. A representative schematic of this methodology is shown in Figure 27.

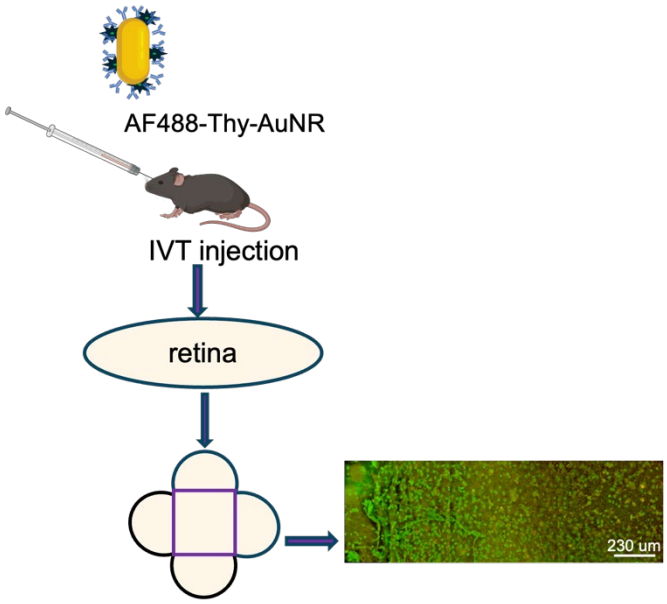

Figure 27 Schematic representation of the study design to evaluate hypothesis 1f, distribution of Thy-antigen in the retina.

2.3.5. Results

Effect of enzyme

Hypothesis 1a**:** IVT injection effectively delivers AuNRs to the retina through the VH and ILM**.**

Hypothesis 1b**:** Enzymes to degrade the ILM enhance AuNR diffusion to the retina.

To evaluate hypotheses 1a and 1b, we quantified TPL signal intensity in retinal flat mounts at 8 DPI. Three groups were analyzed: Thy-AuNRs only (n=8 retinas), Thy-AuNRs + enzyme (n=8 retinas), and PBS sham (n=8 retinas). Results are shown in Figure 28.

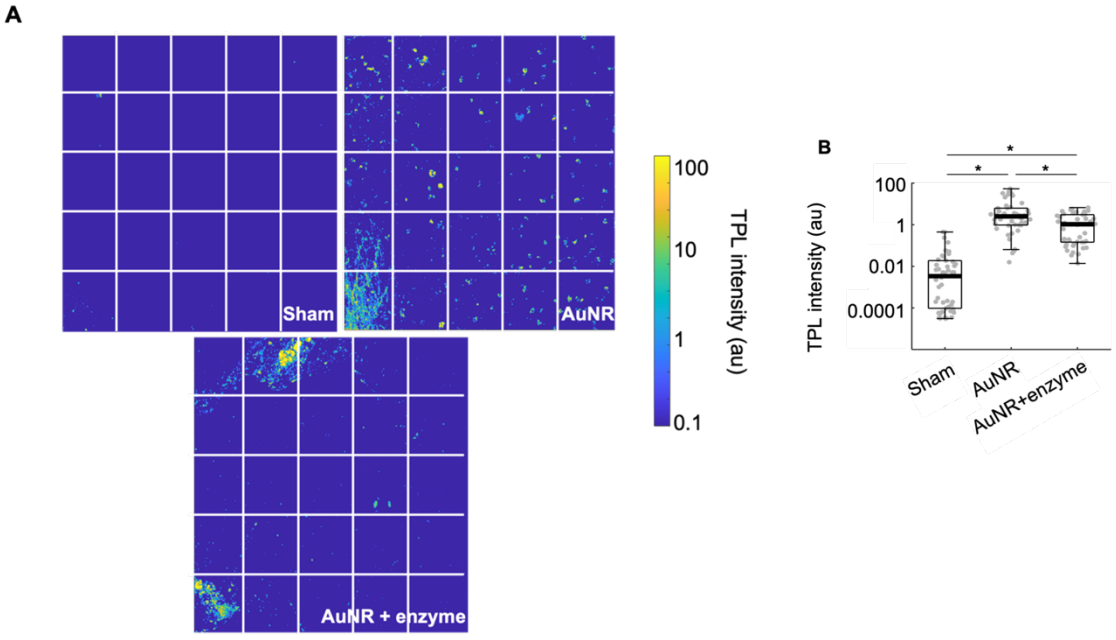

Figure 28 (A) TPL intensity maps displaying representative images of retinas from Sham, 25-nm Thy-AuNR, and 25-nm Thy-AuNR-enzyme groups analyzed at 8 DPI, images are MIPs (B) box-and-whisker plots for average TPL intensity, individual grey dots are ROIs from each group, ROIs are individual tiles. Post-hoc pairwise comparison using Tukey's HSD showed significant differences indicated by an asterisk (*) ($p < 0.05$). Each TPL intensity map spans an area of 1.3 × 1.3 mm.

As shown in the box-and-whisker plot (Figure 28-B), both AuNR-injected groups displayed elevated signal distribution compared to the sham, confirming the successful delivery of AuNRs to the retina. One-way ANOVA analysis revealed a significant overall difference in TPL intensity across groups ($p < 0.001$). Post-hoc pairwise comparisons using Tukey's HSD test confirmed significant differences between:

- Sham versus AuNR-only ($p < 0.05$, Cohen's $d = 0.72$)
- AuNR only versus AuNR + enzyme ($p < 0.05$, Cohen's $d = 0.03$)
- AuNR + enzyme versus sham ($p < 0.05$, Cohen's $d = 0.76$)

Contrary to our expectation regarding the second hypothesis (1b), enzymatic treatment did not enhance AuNR delivery. In fact, the AuNR-only group exhibited slightly higher TPL signal intensity compared to the enzyme assisted group (mean difference: 5%). The effect size between these groups was minimal (Cohen's $d = 0.03$), falling well below the threshold commonly considered clinically relevant ($d \approx 0.2$ in biomedical contexts). Suggesting that ILM permeability may not be a limiting factor for 25-nm Thy-AuNRs under these conditions.

Effects of conjugation and size

Hypothesis 1c**:** Anti-Thy conjugation increases the amount of AuNRs in the retina

Hypothesis 1d**:** The size of AuNRs does not significantly alter the retinal diffusion of AuNRs

To test hypothesis 1c, we compared retinal TPL intensities between mice injected with 25-nm Thy-AuNRs (n=8 retinas), and those injected with 25-nm bare-

AuNRs lacking surface conjugation (n=8 retinas), with analysis performed at 32 DPI . As shown in Figure 29, box-and-whisker plots indicate that 25-nm Thy-AuNRs exhibited markedly higher TPL signal intensities (mean intensity: 0.69; 95% CI: 0.55 to 0.89) than bare-AuNRs (mean intensity: 0.10; 95% CI: 0.063 to 0.18). A one-way ANOVA indicated a significant difference between these two groups ($p < 0.01$), supporting the role of anti-Thy conjugation in enhancing AuNR accumulation in the retina.

To test hypothesis 1d and validate specificity of Thy-mediated targeting, we analyzed three additional groups: 25-nm Thy-AuNRs (n=8 retinas), 10-nm Thy-AuNRs (n=8 retinas), and a validation control group in which 25-nm Thy-AuNRs were pre-incubated with Thy-antigens to block antibody binding (n=8 retinas). All samples were analyzed at 8 DPI. Box-and-whisker plots and TPL intensity maps (Figure 29-B) show that 25-nm AuNRs produced higher retinal TPL signals (mean intensity: 0.88; 95% CI: 0.82 to 0.93) than smaller 10-nm Thy-AuNRs (mean intensity: 0.079; 95% CI: 0.05 to 0.11). Both AuNR sizes showed substantially greater signals than the validation control (mean intensity: 0.005; 95% CI: 0.004 to 0.006), indicating the retention of targeting specificity in both cases.

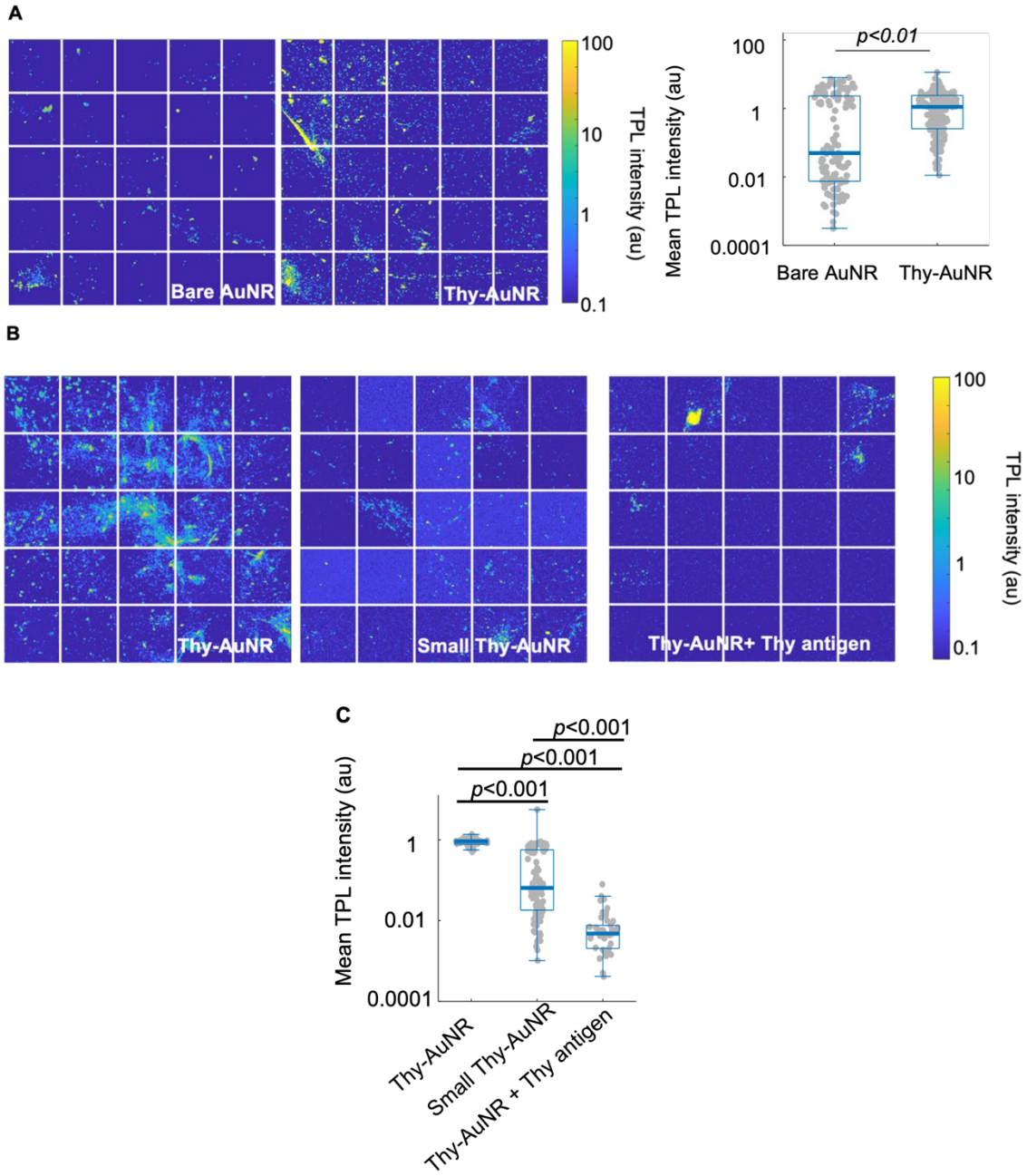

Figure 29 Representative TPL intensity maps for retinas from (A) 25-nm bare AuNRs and 25-nm Thy AuNRs analyzed at 32 DPI, statistical analysis figure shows grey dots as individual ROIs from tiles, ANOVA showed significant a difference ($p < 0.01$) (B) retinas analyzed at 8 DPI, (C) box-and-whisker plot showing analysis of ROIs, Games-Howell revealed significant differences ($p < 0.001$). Each TPL intensity map spans an area of 1.3 × 1.3 mm.

A Welch's ANOVA detected significant differences among the three groups ($p < 0.001$), and a post-hoc comparisons using the Games-Howell test confirmed the following pairwise differences:

- 25-nm Thy AuNRs and 10-nm Thy-AuNRs ($p < 0.001$)
- 25-nm Thy AuNRs and validation control ($p < 0.001$)
- 10-nm AuNRs and validation control ($p < 0.001$)

Together, these results suggest that anti-Thy conjugation significantly enhances retinal AuNR accumulation, and that particle size plays a meaningful role in retention or diffusion, with larger AuNRs showing higher TPL signals under otherwise identical conditions.

Effect of DPI: Half-life

Hypothesis 1e: The IVT delivered amount of AuNRs decreases with DPI

To evaluate this hypothesis, we injected one AuNR type, 25 nm Thy-AuNRs, and quantified retinal TPL signal intensity from flat-mounted retinas at 2, 8, 32, and 134 DP (n=8 retinas per time point). These timepoints were selected to approximate a quasi-logarithmic scale to characterize both early and long-term AuNR retention in retinal tissue. The resulting decay pattern yielded a half-life of ~98 days (95% CI: 80 to 126).

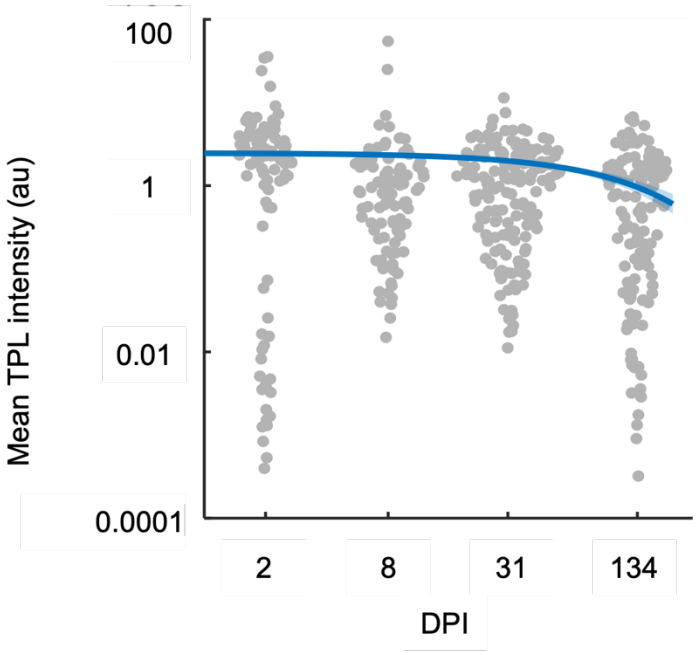

Figure 30 GLM modeling of AuNR half-life using Poisson distribution and log-link function. Grey dots represent individual ROIs, and the thin blue shading represents the 95% CI.

To model signal decay over time, we utilized a generalized linear model (GLM) using a Poisson distribution and a log-link function, graphically represented in Figure 30. Although Poisson regression is conventionally applied to count-data, it was selected here due to the right-skewed nature of TPL intensity values. The log-link linearized the expected exponential decay trend, simplifying estimation of the decay rate and evaluation of model fit. The fitted model is described by the equation:

$$(TPL) = 2.5e^{-0.0071(DPI)}$$

Equation 1 Equation describing the fit model for TPL signal intensity

This model captures an exponential decline in AuNR-associated TPL signal with increasing DPI, consistent with a first-order elimination profile. While not designed for predictive modeling, this framework effectively characterizes the temporal dynamics of AuNR persistence in the retina following a single IVT dose.

2.3.6. Discussion

Effect of enzyme

We examined the effects of enzyme assisted IVT delivery of 25-nm Thy-AuNRs on retinal TPL intensity to quantify the degree of AuNR accumulation following a single injection (Figure 28). Co-injection with glycosidic enzymes did not enhance TPL signal intensity ($p < 0.05$; Cohen's $d = 0.03$), indicating no substantial increase in AuNR diffusion to the retina. This result contrasts with the findings of Cehajic-Kapetanovic et al. who demonstrated improved adeno-associated viral (AAV) vector transfection rates following enzyme-assisted IVT delivery in mice[135]. In our study, the enzyme-free group exhibited marginally higher signal intensities (~5% higher), though the effect size was well below the threshold of biomedical clinical relevance ($d \approx 0.2$). These findings suggest that enzymatic ILM disruption may not be necessary for AuNR retinal delivery in mice.

This discrepancy with Cehajic-Kapetanovic et al. may reflect differences in NP size, shape, and biophysical properties. AAV vectors are roughly spherical (~25-30 nm capsids [146]), whereas AuNRs used in our study measured (25 nm × 119 nm). Although AAVs are not NPs, they share similar size schemes. The larger aspect ratio of AuNRs could affect their diffusion, and the pores created by

glycosidic enzymes which act on ILM proteoglycans and vitreous hyaluronic acid, may have been insufficiently large to enhance AuNR transport.

It is also possible that both enzyme and non-enzyme AuNRs utilized similar cellular conduits for retinal access. Koo et al. reported that large (200-300 nm) polymeric NPs with surface modifications (e.g., hyaluronic acid or human serum albumin), localized to Müller cells, suggesting that NP diffusion requires at least partial ILM penetration [134]. Given the ILM's structure as a dense extracellular matrix, even this scheme likely necessitates traversal of the ILM. Therefore, our findings do not support an ILM-independent mechanism for AuNR diffusion. Rather, they suggest that AuNRs may be small and surface-functionalized enough to traverse the ILM passively without requiring enzymatic assistance in mice.

Species-specific ILM properties should also be considered. In rabbits, enzymatic pretreatment has been shown to improve retinal delivery of therapeutics [147]. Thus, while enzyme co-administration may be unnecessary for AuNR diffusion in mice, it may still be relevant in larger animals or humans, where the ILM is thicker and more structurally complex [148].

Our results confirm that IVT-injected AuNRs can reach the retina and accumulate there by crossing the VH and ILM barriers. The significant difference in TPL signal intensity between the sham injected (PBS) group and the Thy-AuNR injected group ($p < 0.05$; Tukey's HSD) supports this conclusion. Previous studies examining IVT delivery of AuNPs showed that after 24h AuNRs were either found at the vitreoretinal (VR) interface [125], or that they began to experience retinal clearing as early as 48h and showed complete clearance at 14 DPI [130]. Sandrian

et al. utilized Thy-AuNRs (unknown size) and examined ocular tissue using TEM 24h after administration [125], and only qualitatively examined the VR distribution of particles, while Song et al. reported gold nano disk (AuND) clearance by 14 DPI using OCT imaging [130]. Differences in imaging modality, particle geometry, and DPI likely account for these discrepancies. Notably, TPL offers deep axial resolution (> 250 μm) and fluorophore-independent detection, providing a more sensitive tool for AuNR quantification.

In summary we have systematically characterized the ability of antibody-conjugated AuNRs to penetrate the VH and ILM and reach the retina following IVT injection. To our knowledge, this is the first qualitative study of its kind using TPL microscopy to assess retinal AuNR distribution over time.

Effects of conjugation and size

We investigated the effect of surface conjugation and NP size on the retinal accumulation of AuNRs, as measured by TPL signal intensity following a single IVT dose. Mice were IVT injected with either 25-nm Thy-AuNRs or unconjugated bare-AuNRs, and retinal flat mounts were analyzed at 32 DPI (Figure 29). Thy-conjugated AuNRs exhibited significantly higher retinal TPL signal intensities than bare-AuNRs ($p < 0.01$), confirming that surface conjugation enhances post-IVT retinal accumulation. These *in-vivo* results align with Wilson et al. who showed *ex-vivo* RGC targeting efficacy of antibody-conjugated AuNPs compared to bare particles [129], but extend those findings by demonstrating *in-vivo* diffusion through the VH and ILM. Sandrian et al. also used Thy-conjugated AuNRs *in-vivo*, but their

TEM analysis at 24h post-injection was limited to qualitative localization at the VR interface and did not quantify retinal localization[125].

To isolate the effect of nanoparticle size, we compared 10-nm and 25-nm Thy-AuNRs administered at equivalent molar concentrations (4 nM) and injection volumes (0.5 μL) and measured TPL intensity at 8 DPI. The smaller 10-nm AuNRs produced significantly lower retinal TPL signal intensity ($p < 0.01$) with an average percent difference of (~170%). This discrepancy may partly reflect the smaller absorption cross-section of the 10-nm AuNRs, as well as differences in optical and particle-number related properties at a constant molar dose. However, the magnitude of the observed signal difference exceeds expectations based on geometric area alone, consistent with nonlinear scaling of two-photon absorption cross-sections.

An additional contributing factor could be differential clearance kinetics. Smaller AuNRs may be cleared more rapidly from the vitreous prior to retinal diffusion. Song et al. reported that larger gold AuNDs (~160 nm) were entirely cleared within 14 DPI when tracked by OCT [130]. While their study examined a different shape and imaging modality, and our tissues were analyzed earlier (8 DPI), this suggests that size-dependent clearance may outpace diffusion for smaller particles. Thus, the markedly low signal from 10-nm AuNRs likely reflects a combination of optical properties and increased susceptibility to early clearance.

Importantly, both the 25-nm and 10-nm Thy-AuNRs produced significantly higher TPL intensities than the antigen-blocked validation control group ($p < 0.01$), reinforcing the role of Thy-conjugation in promoting retinal accumulation post-IVT

injection. Taken together, these results suggest that both surface conjugation and nanoparticle size substantially influence the efficiency of retinal transduction following IVT administration. While size may increase clearance prior to diffusion, Thy-conjugation enhances specific accumulation within retinal tissue. The comparisons between 25-nm Thy-AuNRs and bare 25-nm AuNRs yielded an average percent difference of (~150%), further emphasizing the importance of targeted conjugation in enhancing retinal uptake.

Effect of DPI: Half-life

To determine the half-life of AuNRs and model their decay, we IVT injected 25-nm Thy-AuNRs and evaluated retinal TPL signal intensity at 2, 8, 32, and 134 DPI. We modeled signal decay over time using a GLM with a Poisson distribution and log-link function, as the TPL signal was right-skewed and exhibited exponential decay characteristics.

From this model, we estimated a retinal half-life of approximately 98 days. To our knowledge, this is the longest post-injection interval evaluated for AuNPs delivered IVT, as prior studies rarely exceeded 7 DPI. Notably, Song et al. assessed AuNDs up to 14 DPI and reported complete clearance from the vitreous by that time, but did not evaluate retinal accumulation [130]. Differences in geometry between AuNDs and AuNRs could partly explain this discrepancy; however, as discussed in the previous section, surface conjugation is likely a more decisive factor in determining retinal retention and accumulation.

In the context of photothermal retinal neuromodulation, this long half-life suggests that a second dose may only be needed 2-3 months after an initial dose, supporting the feasibility of sustained therapeutic activity from a single IVT injection. Considering that IVT administration is a widely used, minimally invasive outpatient procedure with a well-established safety profile, this delivery route further strengthens the translational potential of AuNR based interventions.

Cellular turnover within the mammalian retina is unlikely to account for the observed decrease in AuNRs, as measured by TPL signal intensity. Photoreceptor turnover occurs almost exclusively in the outer segments, where newly formed discs are continually added at the base and displaced discs are removed at the distal tips in contact with the RPE. These displaced discs are phagocytosed by the RPE, a process well-documented in both rats and humans as this process largely occurs in the outer segments of photoreceptor cells [149–151]. By contrast, our AuNRs were primarily localized within the GCL, IPL and OPL layers (Figure 31), for which no evidence of cellular turnover has been reported.

The limited structural evidence addressing turnover in the inner retina, such as the study conducted by Bonnin et al., pertains specifically to protein synthesis and replacement rather than cell or membrane turnover [152]. While this indicates low protein turnover, it does not exclude receptor recycling or phagocytic processing of membrane-bound nanoparticles, both of which could contribute to TPL signal changes. Additionally, Neufeld et al. reported that in adult mice, RGCs loss occurs at approximately 2.3% per month, and in humans the cumulative loss across the lifespan is similar, suggesting overall low turnover [153]. Importantly, this

RGC decline is primarily attributed to aging and does not necessarily imply a potential future loss of stimulatory efficacy due to RGC-bound AuNR depletion.

A more plausible mechanism may involve receptor turnover or recycling of surface antigens to which AuNRs are bound. Although this has not been extensively characterized in RGCs, Thy-1 belongs to the class of glycosylphosphatidylinositol (GPI)-anchored proteins, which are known to undergo clathrin-independent endocytosis. While Thy-1 itself is not directly associated with the immune response, its recycling could theoretically result in the internalization and re-presentation of AuNRs. By analogy, GPI-anchored proteins on dendritic cells (DCs) can be recycled in ways that initiate humoral immune responses [154]. This raises the possibility, albeit speculative, that AuNRs bound to Thy-1 might be subject to uptake by monocytes, glial cells, or immune pathways involving DC-B cell interactions [155–157]. Additionally, Müller cells could play a role by releasing signaling molecules that recruit glial cell or monocyte activity in the vicinity of AuNRs.

Even a theoretical recycling of Thy-bound AuNRs can be tolerated given the estimated half-life of 98 DPI. The gradual decrease in TPL signal could reflect slow clearance or redistribution of AuNRs, rather than cell turnover. Future dosing schemes can consider whether AuNRs are internalized when receptors are potentially recycled by neurons. As described in our previous work [117], confocal imaging combined with image segmentation can distinguish membrane-bound versus internalized AuNRs. Given this prolonged retention, it will also be important to assess whether the sustained AuNR presence influences downstream cellular

processes, including reactive oxygen species (ROS) generation and potential cytotoxicity.

Furthermore, although photoreceptor outer-segment renewal occurs continuously under normal conditions, this process is not relevant to disease models such as AMD and RP, where photoreceptor cell death dominates [2–7]. In these contexts, photoreceptors are progressively lost, and the contribution of outer segment turnover becomes negligible. Thus, the decrease in TPL signal over time in our study is unlikely to result from normal photoreceptor renewal and more plausibly reflects receptor recycling or other clearance pathways for AuNRs.

In the next section we will examine the cell-layered specific distribution of AuNRs in the retina, supported by evidence from confocal microscopy imaging of fluorescently tagged AuNRs in retinal flat mounts.

2.4. Qualitative assessment of layered pattern of delivery with confocal fluorescence microscopy

2.4.1. Confocal microscopy: How it enables 3D imaging

In light microscopy, light passes through a sample as uniformly as possible over the field-of-view (FOV). With thicker samples, when the objective lens does not have sufficient depth of focus, light is detected from sample planes above and below the focal plane. This light adds blur to the image and reduces resolution, in fluorescence microscopy any dye molecules in the FOV are stimulated, including those in the out-of-focus planes, like thick samples in light microscopy. Confocal

microscopy delivers a means to reject the out-of-focus light from the detector so that it does not contribute blur to the images being acquired, allowing for high-resolution images from thick tissues.

Basic components of modern confocal microscopes are the pinholes, objective lenses, detectors, fast scanning mirrors, filters that enable wavelength selection, and laser illumination [158]. Resolution is determined by the numerical aperture of the objective lens, the index of refraction as it applies to the properties of the sample, and the wavelength of light. Resolution is improved when the pinhole is closed to the minimum size, with a best obtainable lateral resolution of ~0.2 μm, and axial resolution of ~0.6 μm.

In laser scanning confocal microscopes, a laser beam sweeps over the sample with the help of galvanometer mirrors. The laser is typically directed onto mirrors that sweep the beam in the x- and y-directions of a single FOV, and then incrementally moved across the entire sample to produce an image of that optical section. When collecting a z-stack, the focal point is changed, and this process of scanning the sample with the laser beam is repeated over a new optical section. Upon completing the collection of optical sections, a 3D image of the sample can be reconstructed.

2.4.2. Confocal fluorescence imaging of fluorescently tagged nanoparticles: Previous studies

Laser scanning confocal microscopy (LSCM) has been widely utilized to visualize the localization of fluorescently labeled nanoparticles (NPs) in ocular

tissues. For instance, Koo et al. employed LSCM to track polymeric NPs in rodent eyes following IVT injection, revealing their accumulation at the ILM, their retinal diffusion, and subsequent clearance 72h post-injection [134]. Their data also demonstrated co-localization with Müller cells, suggesting a potential route for retinal diffusion. Similarly, Ottoneli et al. used LSCM to examine the retinal distribution of Cy5-labeled hyaluronic acid-coated NPs showing their presence across several retinal layers, specifically the outer plexiform layer (OPL), inner nuclear layer (INL) and inner plexiform layer (IPL) [124].

For our investigation under hypothesis 1f, which seeks to determine the intraretinal localization of AuNRs relative to Thy-antigen expression, LSCM represents a viable platform provided the AuNRs are fluorescently tagged. Additionally, nuclear counter staining with DAPI enables structural orientation within retinal tissue, allowing us to correlate AuNR distribution with specific cellular layers. When performed on retinal tissues, these complementary techniques allow precise spatial mapping of AuNR accumulation and enhance our understanding of their tissue-level localization following IVT delivery.

2.4.3. Establishment of imaging protocols

As confocal microscopy is widely utilized in biomedical research, we adhered to typical imaging protocols. In detail, we utilized a 3 × 4 unstitched tile scan, to achieve a total imaging area of approximately 1.5 mm × 2.0 mm , with an axial depth of 290-µm. This configuration allowed for volumetric visualization across the full thickness of the retina.

2.4.4. Results

Following optimization, confocal imaging enabled successful visualization of AuNR localization in intact whole-mount retinas. As shown in Figure 31, AuNR signal was observed in the GCL, IPL and OPL. This pattern aligns with known Thy expression in the GCL and IPL as reported by Barnstable and Dräger [136], and Beale and Osbourne [137]. Additionally, the signal observed in the OPL suggests deeper penetration of Thy-conjugated AuNRs in agreement with the OPL Thy-labeling observed by Perry et al. [159]. Given the whole mount imaging approach and the preserved retinal architecture, these findings suggest effective intraretinal transport of AuNRs post-IVT injection.

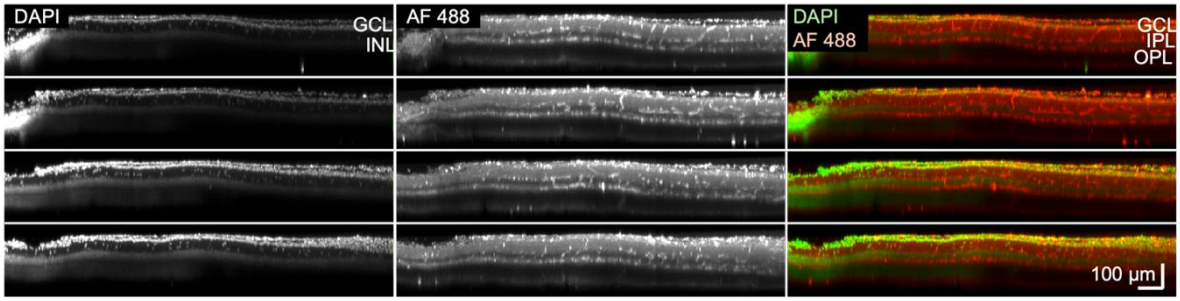

Figure 31 Representative confocal image for AF488 tagged 25-nm Thy-AuNRs. DAPI shown in green, AF488 AuNR signal shown in red Images are shown as 4 slabs corresponding to tiles from the area of imaging, total area 1.5 mm x 2.0 mm, axial depth of 290-µm. GCL: ganglion cell layer, IPL: inner plexiform layer, OPL: outer plexiform layer

2.4.5. Discussion

Our confocal imaging results support prior reports of Thy-antigen distribution in the GCL, INL and OPL consistent with earlier studies [136,137,159]. These findings reinforce the rationale for Thy-mediated targeting to enhance retinal neuronal delivery. Notably, the observed localization pattern suggests that both ganglion cells and bipolar cells (BCs) are accessible targets following IVT administration of

Thy-AuNRs. This is particularly relevant in the context of near-infrared neuronal stimulation, where bipolar cells have emerged as viable targets, as demonstrated by Nie et al.[117]. Moreover, our targeting strategy aligns with recent advancements in retinal prosthetic design, such as subretinal voltaic arrays which also focus on bipolar cell activation to restore vision [104].

2.5. Conclusion

We demonstrated the feasibility of intravitreal (IVT) injection as an effective strategy for delivering gold nanorods (AuNRs) to the retina, and we quantitatively assessed their retinal accumulation using two-photon luminescence (TPL) imaging. In contrast to prior assumptions in the literature, our findings indicate that the inner limiting membrane (ILM) does not represent a major barrier to IVT trafficking of AuNRs. This was evident in our enzymatic co-injection experiments, where degradation of the ILM did not enhance AuNR delivery; in fact, TPL of enzyme-assisted AuNRs was marginally lower than the non-enzymatically assisted group. These results suggest that, at least for AuNR of this size and conjugation profile, passive diffusion or cell-mediated uptake across the ILM is sufficient for retinal access.

Our data also support the conclusion that surface conjugation plays a more pivotal role than particle size in promoting retinal accumulation. Conjugation of AuNRs with Thy antibodies significantly enhanced their retention and localization within retinal layers, as compared to bare (unconjugated) AuNRs, which likely undergo more rapid clearance from the vitreous. This effect was further validated

using antigen-blocked AuNRs which behaved similarly to bare AuNRs and exhibited low TPL signal intensities, underscoring the specificity and functional importance of Thy targeting.

Although smaller AuNRs (10 nm) were delivered at the same molar dose as 25-nm particles (4 nM), they produced a significantly lower TPL signal intensity, likely reflecting differences in optical properties, particle number, and potentially more rapid clearance dynamics. These findings indicate that while surface conjugation governs the extent of intravitreal accumulation, nanoparticle size may have a stronger influence on the pharmacokinetics and biodistribution of AuNRs following IVT injection.

Importantly, we established an *in-vivo* clearance profile and estimated the half-life of Thy-conjugated AuNRs as approximately 98 days. To our knowledge this is the longest reported post-injection interval for tracking AuNRs delivered via IVT injection. This extended half-life suggests that AuNRs can persist in the ocular environment long enough to support sustained therapeutic applications, such as photothermal neuromodulation, for up to three months following a single dose. Considering that IVT injections are routinely performed in clinical ophthalmology with minimal recovery time, this approach offers a clinically translatable platform for sustained retinal stimulation.

3. Chapter 3: Systemic toxicity of intravitreally delivered gold nanorods[2]

3.1. Introduction

Retinal delivery of AuNRs has revealed certain clearance dynamics that occur from two different ocular chambers. The anterior portion which includes the vitreous humor (VH), and follows an aqueous clearance pathway, namely through regeneration of VH, and the regular flushing of the anterior chamber via tear ducts. The posterior chamber is vascular and thus can either clear items through lymphatic drainage (upon detection by the reticular endothelial system), or through choroidal vascular pathways through the blood-retinal-barrier (BRB).

Examples in *Chapter 2*, exhibited complete vitreal clearance of gold nano-disks (AuNDs) [130], or the accumulation of gold nanorods (AuNRs) as early as 24h post-injection at the inner limiting membrane (ILM) [125], and our own study which demonstrated a half-life of 98 days [117]. It is unclear what may happen to these particles if they were to utilize the clearance pathway of the posterior chamber and potentially distribute systemically. Kim et al. demonstrated that intravenously (IV) administered gold nanoparticles (AuNPs) crossed the BRB and distributed in almost all retinal layers [160], which leads us to question whether particles that are

[2] Results in this chapter are found in the following two published articles [1] DOI: 10.1021/acsnano.4c14061; and [2] https://doi.org/10.1007/s43188-025-00295-y. H.A co-designed the study, conducted rodent phlebotomy and analyses, and conducted statistical analysis of the data.

accumulated in the retina diffuse to the systemic circulation. This chapter will examine the systemic toxicity of AuNRs following intravitreal (IVT) delivery and attempt to answer this overarching question.

3.1.1. Prior studies on systemic toxicity of gold nanoparticles

Zhang et al. investigated the *in-vivo* toxicity profile of polyethylene glycol (PEG)-functionalized gold nanospheres (AuNSs) of various diameters (5-, 10-, 30-, and 60-nm) to evaluate their potential for photothermal and radiotherapeutic applications [161]. The nanoparticles were administered to mice via intraperitoneal (IP) injection. Biodistribution analysis revealed pronounced size-dependent accumulation patterns: smaller particles (5- and 10-nm) predominantly accumulated in the liver, while the intermediately sized 30-nm particles were sequestered mainly in the spleen. In contrast, the 60-nm AuNSs exhibited negligible accumulation in these organs, possibly due to reduced permeability across biological barriers or enhanced systemic for larger nanoparticles (NPs).

Transmission electron microscopy (TEM) further confirmed the presence of all four particle sizes in circulating blood and bone marrow cells. Notably, both 5-nm and 60-nm particles were prone to aggregation within blood cells, which could have implications on their vascular stability, circulation time and immunogenicity. Evaluation of organ indices further indicated that exposure to 5-, 10- and 30- nm AuNSs induced immunological responses. Specifically, the 10-nm group exhibited elevated white blood cell (WBC) counts, consistent with a pro-inflammatory response, whereas both 5-nm and 30-nm particles led to reductions in WBC and

red blood cell (RBC) counts, potentially indicating hematotoxic effects or suppression of hematopoiesis.

Biochemical assays revealed that 10-nm and 60-nm particles caused statistically significant elevations in serum alanine transaminase (ALT) and aspartate transaminase (AST) levels, enzymatic markers indicative of hepatocellular stress. Interestingly, while the 10-nm particles demonstrated high liver accumulation and immune activation, the 60-nm particles induced hepatotoxicity despite limited hepatic accumulation. This finding highlights a potentially size-dependent coupling between biodistribution and toxicity, emphasizing the need to evaluate not only where particles accumulate, but how their physical and surface properties may elicit cellular responses at low concentrations.

In contrast to Zhang et al. Isoda et al. investigated the toxicity of PEG-coated AuNSs (10-, 50- and 100-nm) administered via the tail-vein injection [162]. They reported no overt toxicity from the AuNSs alone. However, nephrotoxic effects emerged when AuNSs were co-administered with known nephrotoxic agents such as cisplatin or paraquat. This observation underscores the potential for NP-drug interactions to exacerbate organ-specific toxicities, particularly in the kidneys, and raises concerns about the combinatory effects of AuNPs with systemic therapeutics.

Similarly, Cho et al. administered 13-nm PEG coated AuNSs IV and tracked tissue accumulation and toxicity at multiple time points (5m to 7 days-post-injection) [163]. Gold content peaked at approximately 4h post-injection and

continued to accumulate in tissues until 7 days-post-injection (DPI), with major accumulation in the liver and spleen. Terminal deoxynucleotidyl transferase dUTP nick end labeling (TUNEL) staining revealed a dose-dependent increase in apoptotic cells within the liver, alongside an upregulation of inflammatory markers. These results indicate that PEGylated AuNPs can induce acute liver toxicity and immunoinflammatory responses upon accumulation, even when surface-functionalized to enhance biocompatibility. This highlights a key challenge in nanoparticle engineering: improving circulation time via PEGylation may inadvertently promote accumulation in vital organs, exacerbating toxicity.

In contrast, Simpson et al. reported markedly different outcomes using ultrasmall (1.2-nm) glutathione-coated NPs administered subcutaneously (SC) [164]. Inductively coupled plasma mass spectrometer (ICP-MS) analysis indicated near-complete clearance of gold from blood within 1-week, and from most organs within 4-weeks, except for minimal residual levels in the liver and spleen. Hematological parameters remained stable across most dosing groups, with minor perturbations only at the highest administered dose (60 μM). Importantly, no histological evidence of renal damage was observed. These results suggest that very small AuNPs with alternative surface chemistries, such as glutathione instead of PEG, may offer more favorable clearance profiles and reduced systemic toxicity.

Finally, Ramapabanasi et al. administered 14-nm AuNSs IV in rats across three dose levels (0.9-, 9- and 90-μg) once weekly for 7-weeks to simulate chronic exposure[165]. Neutron activation analysis revealed that the liver and spleen retained the highest concentrations of gold by the end of the dosing period.

However, no significant alterations in hematological markers or serum biochemistry were observed between treated and control groups. Histopathological examination of the heart, kidneys, liver, lungs and spleen also failed to reveal any tissue damage, indicating that repeated low-dose exposure to 14-nm PEGylated AuNPs did not result in overt systemic toxicity under the study conditions.

Taken together, these findings underscore a fundamental issue in the field of nanoparticle toxicology: despite decades of investigation, there remains no unified or predictive framework to reliably assess the safety of AuNPs across different sizes, formulations or delivery routes. The evidence from preclinical studies is highly heterogenous, some report measurable immune and hepatic stress even at moderate doses, while others show negligible toxicity despite prolonged systemic exposure or repeated administration. Surface chemistry, administration route, particle size, and co-delivery with drugs all appear to interact in complex, context-dependent ways, defying oversimplified generalizations about biocompatibility or safe size ranges.

In this context, the current body of literature does not provide a definitive verdict on AuNP safety. Instead, it reveals a landscape of variability, emphasizing the need for harmonized regulatory criteria, robust long-term studies, and clearer interpretive frameworks that can bridge preclinical outcomes with clinical risk assessment. These unanswered questions will be further examined in the following section, where we evaluate the existing regulatory standards, including those of

the FDA and ISO, and explore the challenges of aligning them with the nuanced and sometimes contradictory data emerging from nanoparticle toxicity research.

3.1.2. Unanswered questions

Although previous studies have proposed multiple mechanisms through which AuNRs may elicit toxicity, especially upon systemic distribution and accumulation in vital organs, the conclusions across the literature remain fragmented. Some reports indicate that biodistribution and clearance are primarily governed by NP size, aligning with our own observations of size-dependent clearance from the retina (*Chapter 2*). Other studies emphasize the critical role of surface conjugation in modulating systemic immune responses and tissue accumulation. This divergence highlights a core uncertainty: given the wide variability in particle parameters (e.g., size, coating, concentration) and delivery routes (e.g., intravenous, subcutaneous, intraperitoneal), it remains unclear whether our formulations of AuNRs will produce systemic or organ-specific toxicity following IVT administration.

One important consideration arises from the work of Kim et al. [160], who observed that systemically delivered 20-nm AuNPs distributed to the retina, whereas 100-nm particles did not. While their study did not assess systemic toxicological outcomes, it raises a critical point: nanoparticles may cross the BRB in either direction. This suggests that IVT-administered AuNRs, though delivered locally to the eye, might eventually escape into systemic circulation, thereby exposing peripheral organs to potential AuNR related toxicity. To date, no studies

have examined the systemic biodistribution or toxicity of AuNRs following IVT injection, a major knowledge gap that limits our ability to assess long-term safety.

Moreover, the parameters that might influence systemic toxicity following IVT delivery remain poorly defined. These include AuNR concentration, particle size, surface functionalization, days post injection (DPI), and biological variables such as sex. Each of these factors could plausibly alter NP retention, clearance, and immune reactions systemically, yet few—if any—studies have rigorously examined them in the context of ocularly delivered NPs.

Ambiguity extends to local retinal toxicity as well, Sandrian et al. [125], observed increased neutrophil recruitment following IVT delivery of Thy-conjugated AuNRs potentially indicating an acute inflammatory response. However, their analysis was limited to 24 hours post-injection, and it is unclear whether the inflammation was mild due to the initial introduction of foreign particles into the ocular space. Bakri et al. [166], reported no retinal toxicity up to six months following IVT delivery of AuNRs in rabbits, based solely on H&E staining. However, their study lacked the quantitative delivery metrics, or functional assays, weakening the reliability of their safety claims. Kim et al. assessed retinal toxicity following IV administration and particle diffusion to the retina, using TUNEL staining and H&E morphological analysis. Their results indicated no significant differences between AuNP and control groups [160].

According to ISO standards (ISO/TR 10993-22:2017 [167]), nanomaterials may exhibit distinct toxicological behaviors, including genotoxicity and systemic distribution, necessitating risk assessments that go beyond standard cytotoxicity

testing. The guidance specifically cautions that metallic nano-objects, including gold, can cross cellular membranes, interact directly with DNA, and generate free radicals that lead to DNA strand breaks or chromosomal missegregation, especially during cell division. Moreover, ISO identifies both direct genotoxicity (via DNA contact) and indirect genotoxicity (via oxidative stress and inflammation) as valid mechanisms by which NPs may induce mutagenic or clastogenic changes. As such, it recommends using a combination of *in-vitro* and *in-vivo* models to assess genetic toxicity. This is particularly when particles are administered using routes that enable systemic access. such as IVT injections, which—though localized—carry the possibility of limited NP migration to systemic circulation. AuNRs have yielded conflicting genotoxic outcomes in literature, with both positive and negative outcomes reported depending on size, conjugation and cell type.

The FDA's Nanotechnology Guidance for Industry [168] does not mandate hematological testing, but recommends case-by-case risk assessments based on the nanomaterial's structure, biodistribution and administration route. Furthermore, it states that the potential for toxicity must be rigorously examined. Given the evidence for particles to enter the retina via systemic administration, it is incumbent that the possibility of particles to enter systemic circulation following IVT delivery be thoroughly examined. The FDA also defers to broader preclinical safety standards which emphasize evaluation of systemic and genetic toxicity when novel materials are introduced, especially via injectable routes. Hematologic and serum biochemistry panels, combined with organ histopathology, are standard tools to

monitor for subclinical toxicities that may occur from prolonged nanoparticle exposure.

Given that our approach involves intentional injection of AuNRs into the vitreous cavity, our study addresses two core requirements of regulatory and scientific rigor: (1) establishing biocompatibility and systemic safety of the particles over time, and (2) probing potential genotoxic effects using tissue-level biomarkers. These assessments conform to regulatory expectations and are critical for clinical translation of the PRP towards human use. To facilitate this, we have developed the following hypotheses for evaluation:

2a) IVT-delivered AuNRs do not cause severe systemic toxicity

2b) Higher concentrations of AuNR increase the risk of systemic toxicity (concentration effect)

2c) Small size AuNRs increase the risk of systemic toxicity (size effect)

2d) Non-targeting (bare) AuNRs increase the risk of systemic toxicity (conjugation effect)

2e) The systemic toxicity risk of IVT AuNRs does not increase with DPI (DPI effect)

2f) The systemic toxicity risk does not differ between sex (sex effect)

2g) IVT Thy-AuNRs do not increase the number of caspase III positive cells in the retina (apoptotic activity)

These hypotheses aim to establish a comprehensive toxicity profile for IVT-delivered AuNRs and provide the foundational data necessary for interpreting their risk under regulatory frameworks.

3.2. Methods

3.2.1. Blood collection

We employed the lateral rib cardiac stick technique for terminal blood collection, a method recognized for its reliability in yielding high-volume, high-quality samples. Prior to insertion, the syringe plunger was carefully pre-drawn to reduce negative pressure during aspiration, thereby minimizing the risk of red blood cell lysis due to shear stress. The needle was inserted perpendicularly at the elbow crease of the forelimb, specifically targeting an intercostal space along the lateral thoracic wall where anatomical resistance is minimal. This approach facilitated smooth and consistent needle entry into the cardiac region.

Collected blood was promptly transferred into pre-labeled collection tubes, with strict attention paid to minimizing turbulence during transfer to avoid hemolysis or coagulation artifacts. When serum separator tubes were used, samples were left undisturbed at room temperature for approximately 30-minutes to allow complete clot formation prior to centrifugation and serum isolation. This protocol ensured sample integrity across both hematological and biochemical assays. Samples were shipped in coolers containing gel packs to a CRO for analysis.

3.2.2. Blood and serum sample analysis

Serum chemistry analysis was performed on serum samples sent to IDEXX BioAnalytics (N. Grafton, MA., USA) and run on an automated chemistry analyzer (Beckman Coulter AU680, Brea, CA, USA) validated for murine serum samples. All testing methodologies used analyte-specific reagents measured

spectrophotometrically or potentiometrically. Hematology analysis was performed on K2 EDTA whole-blood samples which were sent to IDEXX BioAnalytics (N. Grafton, MA., USA) and run on an automated hematology analyzer (Sysmex XT-iV, Kobe, Hyogo, Japan) validated for murine samples using a murine-gated algorithm. The testing methodology included impedance and redundant laser flow optical flow cytometric principles for RBC and platelet counts, SLS spectrophotometry for hemoglobin measurement, and flow cytometric principles for WBC counts and differential analysis. When serum sample volume was lower than the minimum volume required for sample analysis, they were diluted with distilled water at a ratio of either 1:1 or 1:2, and the results were corrected based on the dilution factor.

3.2.3. Caspase III histology and cell quantification

We collected eyes from mice that were either injected with 25-nm Thy-AuNRs or PBS at 128 DPI (n=4 retinas each). Eyes were immersed in 4% PFA for 24 hours, prior to being transferred into vials containing 70% ethanol solution. Eyes were then sent to StageBio (Mount Jackson, VA, USA) where they were embedded in paraffin wax, prior to sectioning and activated caspase-III-TRITC immunohistology. A custom-developed algorithm was utilized to detect caspase III positive cells for quantification and analysis. In brief, our algorithm detected an arc tracing the retina along the dark inner plexiform layer (IPL) band, flattened the retina along the arc into a rectangular image, segmented the ganglion cell layer (GCL), inner nuclear layer (INL), the outer nuclear layer (ONL) from the rectangular image and detected cells for each layer through blob-detection.

3.3. Study design and statistical analysis

Hypotheses 2a-2b

We assessed whether IVT delivered AuNRs cause systemic toxicity and concurrently evaluated the effect of AuNR concentration on systemic toxicity. We administered two concentrations of 25-nm Thy-AuNRs, for the standard concentration we administered 0.5 µL per eye (4 nM; n=8 retinas), 0.5 µL per eye in the high concentration (HC-AuNRs) group (15 nM; n=8 retinas), and we injected 0.5 µL per eye of phosphate buffered saline (PBS) as a sham injection (n=8 retinas). We collected blood samples at 128 DPI for all groups. A schematic representation of this overall design is shown in Figure 32.

Our CBC panel included the following:

- **CBC panel:** neutrophil count, white blood cell count (WBC), red blood cell count (RBC), hemoglobin (HGB), reticulocyte count, lymphocyte count, monocyte count, eosinophil count, mean corpuscular volume (MCV), basophil count, mean corpuscular hemoglobin count (MCHC), platelet count.
- **Serum biochemistry panel**: alkaline phosphatase (ALP), aspartate aminotransferase (AST), alanine transaminase (ALT), creatinine kinase (CK), albumin, total protein, globulin, blood urea nitrogen (BUN), cholesterol, glucose, calcium, phosphorus, bicarbonate total carbon dioxide (bicarbonate TCO_2)

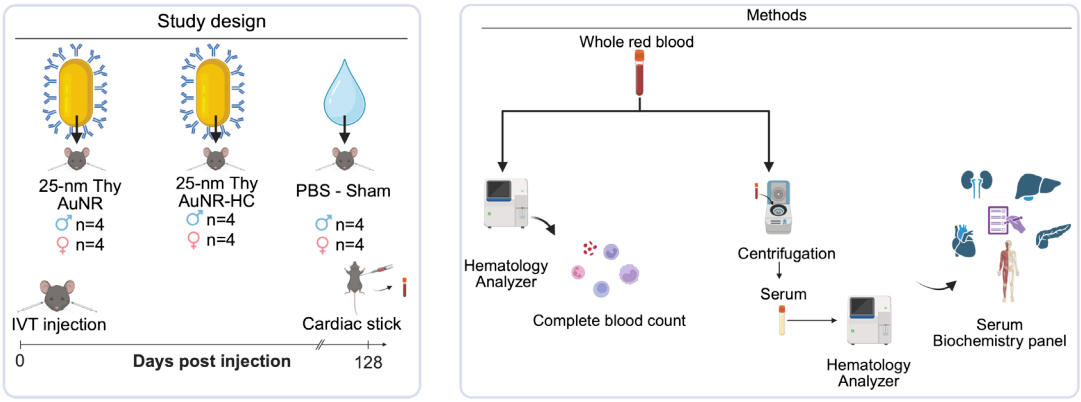

Figure 32 Schematic diagram for the study design to evaluate hypothesis 2a and 2b, the effect of IVT injection and concentration on systemic toxicity

Statistical Analysis

For each of the 13 serum biochemistry markers and the 12 CBC parameters, we evaluated fixed effects of two main predictors: the injected solution type (PBS, AuNRs or HC-AuNRs) and age. Sex was included as a random effect in the linear mixed effects (LME) models. To assess the normality of each response variable, we applied four statistical tests, Kolmogrov-Smirnov, Anderson-Darling, Jarque-Bera, and Lilliefors, and selected the test with the highest p-value to represent the most conservative outcome. Age was expressed as the deviation in weeks from the control group's mean age to standardize its effects across groups.

Model selection followed a hierarchical approach, beginning with the simplest LME model (injected solution only as a fixed effect) and progressing to more complex models that incorporated all predictor variables, including sex as a random effect. At each step, a more complex model was retained only if it provided

a statistically significant improvement in log-likelihood over the simpler model ($p < 0.05$). This strategy allowed us to identify a parsimonious model that adequately explained the data, rejecting unnecessarily complex models that did not offer additional explanatory power.

From the final selected model for each response variable, we determined the significance of each fixed-effect predictor based on its p-value. The critical p-value thresholds, adjusted for multiple comparisons using a Bonferroni correction, were set to 0.003 for CBC outcomes, and 0.002 for the serum biochemistry outcomes. Effect sizes were quantified using Cohen's d, calculated as the ratio of the estimated fixed effect to the standard deviation of the model intercept. For the random effect of sex, its contribution was considered significant only if including it in the model significantly improved the model fit compared to an otherwise identical model lacking the random effect.

Hypotheses 2c-2f

To investigate the effects of AuNR size, surface conjugation, and delivery parameters, including injectate type (PBS vs. AuNRs) and sex, on systemic toxicity. We conducted an IVT injection study using four treatment groups: 10-nm Thy-AuNRs, 25-nm Thy-AuNRs, 25 nm bare-AuNRs, and a PBS sham control. Blood samples were collected at 2, 8 and 32 DPI (n=12 retinas per time point). A schematic overview of the study design is illustrated in Figure 33.

We evaluated a comprehensive panel of hematological and serum biochemical parameters to capture systemic effects. These included:

- **CBC parameters:** neutrophil count, reticulocyte count, WBC, absolute reticulocyte count, RBC,HGB, lymphocyte count, HCT, basophil count, MCH, MCHC, and platelet count.
- **Serum biochemistry:** ALP, AST, ALT, CK, amylase, lipase concentration, albumin, TB, TP, GLOB, conjugated bilirubin, BUN, creatinine, cholesterol, calcium, phosphorus, bicarbonate TCO_2, chloride, potassium, the ALB/GLOB ratio, sodium, the BUN/creatinine ratio, LDH, unconjugated bilirubin, the NA/K ratio, triglycerides, and uric acid.

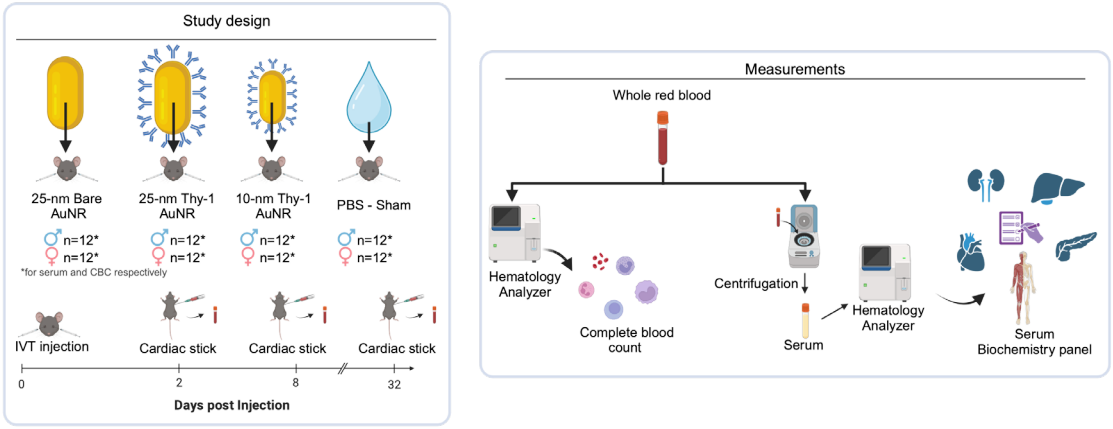

Figure 33 Schematic diagram of study design to evaluate hypotheses 2b-2f, the effects of size, conjugation, DPI and sex on systemic toxicity

Data quality control

Before statistical modeling, we applied a stringent data quality criterion to ensure robust inference. Any hematological or biochemical parameter showing two or fewer unique values out of twelve samples within any experimental group (defined by DPI × treatment) was excluded from further analysis. Parameters removed on this basis included: Total Bilirubin, Bilirubin-Conjugated, Creatinine, Chloride, Potassium, Sodium, BUN/Creatinine ratio, Bilirubin-Unconjugated, and

NA/K ratio. The filtering step mitigates the risk of compromised conclusions from parameters lacking sufficient variability for valid statistical inference.

Statistical Modeling

To evaluate systemic toxicity, we used a generalized linear model (GLM) framework to assess the effects of AuNR treatment (including size and conjugation), DPI and sex on each hematological and serum biochemistry outcome. Age was not included as a primary predictor, due to collinearity with DPI. However, for any parameter where DPI emerged as a statistically significant predictor, we subsequently tested whether this significance remained after including age as a predictor in the model. If DPI lost its significance after adjusting for age, we interpreted the result as a likely age-related effect and annotated with a dagger (†) instead of an asterisk (*) to denote this distinction.

Model comparison was initially conducted between our base GLM and more complex formulations (e.g., incorporating alternative link functions or random effects). These alternative models offered only moderate improvements in fit and did not alter the significance status of key predictors or did not apply to the covariates. Consequently, we selected the simpler model structure a standard GLM with identity link and applied a Bonferroni correction to control for multiple comparisons and limit type-I error inflation. The critical p-value thresholds, adjusted for multiple testing using a Bonferroni correction, were set to 0.003 for CBC outcomes and 0.002 for serum biochemistry outcomes.

Samples with moderate to severe hemolysis (graded '++' or higher) were excluded from the dataset due to unknown artifacts such hemolysis introduces to several analytes. Based on this exclusion criterion, 8 out of 96 serum samples were removed. Where appropriate, we also calculated Cohen's d to report effect sizes for statistically significant predictors.

Hypothesis 2g

To evaluate potential long-term retinal toxicity, we tested the hypothesis that IVT delivery of AuNRs does not induce apoptotic cell death in retinal tissues. Specifically, we injected 25-nm Thy-AuNRs and collected eyes at 128 DPI for histological analysis (n=8 retinas). Apoptosis was assessed via immunolabeling for active caspase III, a well-established marker of cell death. We caspase III positive cells across distinct retinal layers and compared the results to sham-injected controls (n=8 retinas) to determine any treatment associated increase in cell death. A schematic overview of this experimental design is provided in Figure 34.

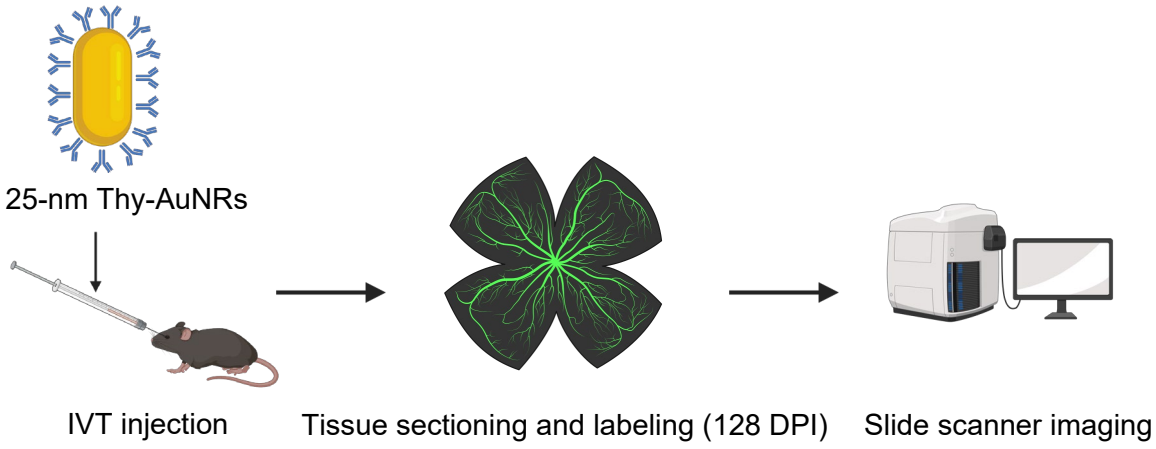

Figure 34 Schematic of study design evaluating hypothesis 2g, caspase III activity in retinas post-AuNR exposure for 128 DPI

3.4. Results

Hypothesis 2a: IVT delivered AuNRs do not cause severe systemic toxicity

Hypothesis 2b: Higher concentrations of AuNRs increase the risk of systemic toxicity

To evaluate these hypotheses, we administered 25-nm Thy-AuNRs via IVT injection at two concentrations, 4 nM (n=8 mice) and 15 nM (n=8 mice), with PBS-injected mice (n=8 mice) serving as controls. We employed LME modeling to assess the impact of concentration, the injectate (AuNRs vs. PBS), age and sex, on systemic toxicity outcomes. The full set of results, including significance levels provided in Table 1 and Table 2, and effect sizes are visualized in Figure 35.

Table 1 Effect of HC-AuNRs on serum biochemistry measures, LME model showing covariates: AuNR, HC-AuNR, age and sex. Columns display predictor variables along with their coefficients, 95% confidence intervals, and corresponding p-values. Significance was assessed at $p < 0.003$ after Bonferroni correction for multiple comparisons. Statistically significant results are shown in **bold** with an asterisk. The number of observations was n = 17. 'N/A' means that the model including the predictor variable of age did not explain the data better. Sex was a random-effect variable, so its significance was tested by the likelihood-ratio test between the model involving it and the one without it (see Methods for detail). The asterisk indicates the former model produced a significantly higher log-likelihood than the latter ($p < 0.05$).

Analytes	Intercept	AuNR	HC-AuNR	Age	Sex
ALP (U/L)	84.2 (62.4 to 106.0) p<0.001	10.4 (-0.7 to 21.5) p=0.06	2.3 (-10.3 to 14.9) p=0.70	-0.15 (-3.3 to 3.0] p=0.91	*
AST (U/L)	46.7 (0.6 to 62.7) p<0.001	30.3 (6.5 to 54.1) p=0.01	12.3 (-10.3 to 35.0) p=0.26	N/A	
ALT (U/L)	22 (7.4 to 36.6) p=0.006	24 (2.4 to 45.6) p=0.03	0.33 (-20.3 to 20.9) p=0.97	N/A	
Creatine kinase (U/L)	143 (36.4 to 249.6) p=0.01	125 (-33.1 to 283.1) p=0.11	203.5 (39.3 to 367.6) p=0.01	-41.9 (-78.3 to -5.5) p=0.02	
Albumin (g/dL)	3.3 (3.2 to 3.4) p<0.001	0.02 (-0.11 to 0.14] p=0.78	-0.11 (-0.24 to 0.02) p=0.10	-0.05 (-0.08 to -0.02) **p=0.002***	
Total Protein (g/dL)	5.7 (5.5 to 5.9) p<0.001	-0.01 (-0.28 to 0.25) p=0.91	-0.22 (-0.50 to 0.06) p=0.11	-0.07 (-0.14 to -0.01) p=0.02	
Globulin (g/dL)	2.5 (2.3 to 2.6) p<0.001	-0.03 (-0.27 to 0.21) p=0.79	-0.15 (-0.38 to 0.08) p=0.18	N/A	
BUN (mg/dL)	32 (29.7 to 34.3) p<0.001	-0.6 (-4.0 to 2.8) p=0.70	-1.7 (-4.9 to 1.5) p=0.28	N/A	
Cholesterol (mg/dL)	86.1 (64.2 to 108.1) p<0.001	-3.1 (-18.0 to 11.7) p=0.65	-5.0 (-21.7 to 11.8) p=0.53	-6.4 (-10.6 to -2.2) p=0.005	*
Glucose (mg/dL)	274.5 (225.6 to 323.4) p<0.001	-73.7 (-146.2 to -1.2) p=0.04	-21.3 (-90.5 to 47.8) p=0.51	N/A	
Calcium (mg/dL)	10.8 (10.5 to 11.2) p<0.001	-0.01 (-0.49 to 0.46) p=0.95	-0.52 (-0.97 to -0.06) p=0.02	N/A	
Phosphorus (mg/dL)	11.1 (10.4 to 11.7) p<0.001	0.25 (-0.57 to 1.07) p=0.51	-0.53 (-1.37 to 0.32) p=0.20	0.19 (0.006 to 0.38) p=0.04	
Bicarbonate TCO2 (mmol/L)	21.2 (18.6 to 23.7) p<0.001	-1.4 (-5.2 to 2.4) p=0.45	-1.7 (-5.3 to 2.0) p=0.33	N/A	

Table 2 Effect of HC-AuNRs on complete blood count measures, results presented similar to table 1. Significance was assessed at $p < 0.002$ after Bonferroni correction for multiple comparisons.

Analyte	Intercept	AuNR	HC-AuNR	Age	Sex
Neutrophil (/μL)	578.4 (139.8 to 1017.0) p=0.01	78.4 (-541.9 to 698.6) p=0.79	550.6 (-69.6 to 1170.9) p=0.07	N/A	
WBC (K/μL)	8.5 (6.7 to 10.3) p<0.001	-0.9 (-3.5 to 1.7) p=0.48	-2.3 (-4.9 to 0.3) p=0.08	N/A	
Reticulocyte (K/μL)	347.5 (321.5 to 373.5) p<0.001	-27.1 (-63.9 to 9.6) p=0.13	-25.4 (-62.1 to 11.4) p=0.16	N/A	
RBC (M/μL)	10.8 (10.6 to 11.1) p<0.001	0.16 (-0.23 to 0.55) p=0.4077	-0.393 (-0.780 to -0.005) p=0.0475	N/A	
HGB (g/dL)	15 (14.7 to 15.4) p<0.001	0.12 (-0.37 to 0.62) p=0.60	-0.488 (-0.978 to 0.003) p=0.05	N/A	
Lymphocyte (/μL)	7319.3 (5843.9 to 8794.6) p<0.001	-866.5 (-2952.9 to 1219.9) p=0.39	-2597.5 (-4683.9 to -511.1) p=0.01	N/A	
Monocyte (/μL)	451.3 (349.9 to 552.6) p<0.001	-31.4 (-174.7 to 111.9) p=0.65	-234.6 (-377.9 to -91.3) **p=0.002**	N/A	
Eosinophil (/μL)	114.1 (33.4 to 194.9) p=0.007	-26.5 (-140.7 to 87.7) p=0.63	45.2 (-69.0 to 159.5) p=0.41	N/A	
MCV (fL)	53.6 (52.3 to 55.0) p<0.001	-0.6 (-2.5 to 1.3) p=0.50	0.4 (-1.5 to 2.3) p=0.68	N/A	
Basophil (/μL)	18.5 (11.0 to 26.0) p<0.001	-10.6 (-21.3 to 0.0) p=0.05	-7.3 (-17.9 to 3.4) p=0.17	N/A	
MCHC (g/dL)	25.9 (25.4 to 26.5) p<0.001	0.21 (-0.59 to 1.01) p=0.58	-0.11 (-0.91 to 0.69) p=0.77	N/A	
Platelet (K/μL)	963.6 (767.3 to 1160.0) p<0.001	-4.6 (-282.3 to 273.0) p=0.97	-254.8 (-532.4 to 22.9) p=0.07	N/A	

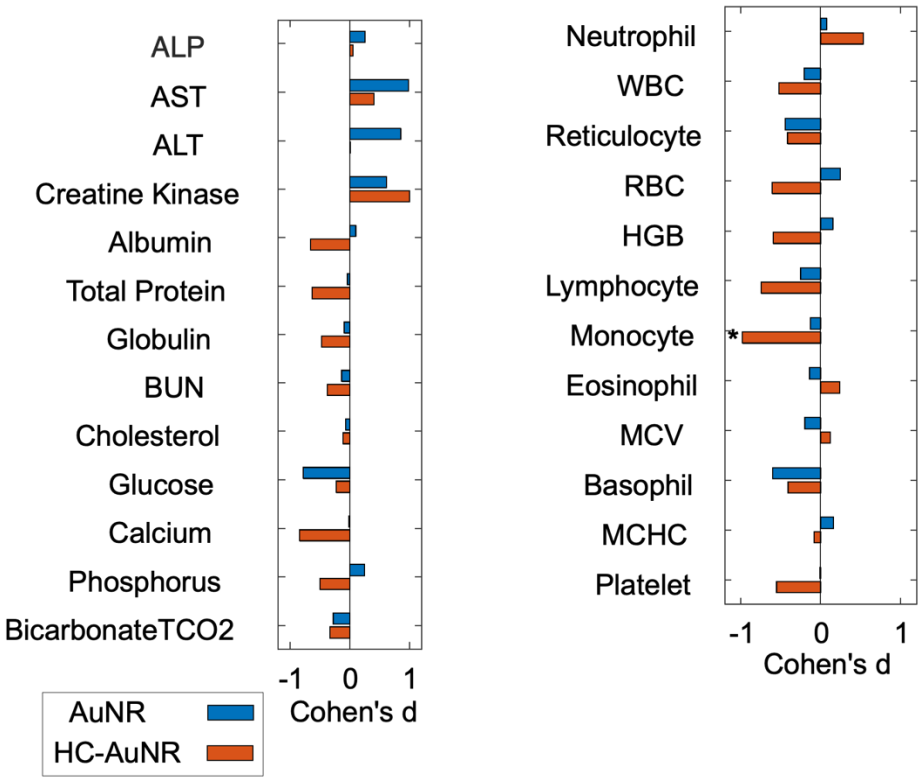

Figure 35 Bar graph displaying Cohen's d values indicating effect size on serum biochemistry measures and CBC between HC-AuNRs and AuNR groups.

In the high-concentration AuNR group, monocyte levels were significantly reduced by 235 cells/μL compared to controls (95% CI: 91 to 378, p = 0.002, Cohen's d = -0.98). This represents a large effect size, suggesting that AuNR concentration had a substantial impact on circulating monocyte counts. No other hematological or serum biochemistry parameters showed statistically significant changes attributable to AuNR concentration. However, a significant age-related effect was observed for albumin levels (p = 0.002), indicating that the variation in albumin was more likely due to natural aging than treatment.

Hypothesis 2c-2f: To test the hypothesis that (2c) smaller-sized AuNRs increase the risk of systemic toxicity, (2d) non-targeting (bare) AuNRs increase the risk of systemic toxicity, (2e) the systemic toxicity risk of IVT-delivered AuNRs does not increase with DPI, and (2f) systemic toxicity risk does not differ between sexes, we administered IVT injections of either 25-nm Thy-AuNRs, 10-nm Thy-AuNRs, or PBS (sham control). Blood samples were collected at 2,8, and 32 DPI, with n= 12 males and n=12 females per time point. A GLM model was applied to assess the influence of nanoparticle presence, size, conjugation state (Thy vs. bare), DPI, and sex on complete blood count (CBC) and serum biochemistry parameters. The full statistical outcomes are presented in Table 3 and Table 4.

Table 3 Summary of generalized linear regression results from the serum biochemistry analysis. Columns display predictor variables along with their coefficients, 95% confidence intervals, and corresponding p-values. Significance was assessed at $p < 0.002$ after Bonferroni correction for multiple comparisons. Statistically significant results are shown in **bold** with an asterisk; a dagger symbol (†) is used in place of an asterisk where the DPI effect may reflect aging (see study design). The effect of AuNR treatment was evaluated against PBS controls; size comparisons were made between 10 nm and the default 25 nm AuNRs (identical aspect ratios); conjugation was tested between bare and Thy-1 functionalized AuNRs. DPI was modeled as $\log_2(\text{DPI}/2)$, yielding values of 0, 2, and 4 for DPIs of 2, 8, and 32, respectively. The effect of sex was assessed by comparing females to males. The analysis was based on 88 total response measurements per parameter.

Analyte	Intercept	AuNR	AuNR size	AuNR conjugation	DPI	Sex
ALB/GLOB ratio	1.5 (1.4 to 1.6) p<0.001	0.01 (-0.10 to 0.10) p=0.84	-0.01 (-0.10 to 0.10) p=0.78	-0.1 (-0.10 to 0.02) p=0.15	-0.03 (-0.04 to -0.01) **p=0.002***	0.3 (0.3 to 0.4) p<0.001*
Albumin (g/dL)	3.2 (3.1 to 3.3) p<0.001	0.03 (-0.10 to 0.13) p=0.53	-0.02 (-0.12 to 0.10) p=0.72	-0.1 (-0.20 to 0.01) p=0.72	-0.01 (-0.04 to 0.01) p=0.16	0.2 (0.1 to 0.2) p<0.001*
ALP (U/L)	79.0 (72 to 86) p<0.001	-4 (-11 to 4) p=0.33	3.0 (-4 to 11) p=0.38	7.0 (-1 to 14) p=0.08	-2.0 (-4.0 to -0.3) p=0.01	43.0 (38 to 49) p<0.001*
ALT (U/L)	22.0 (-44 to 90) p=0.51	-0.3 (-74.4 to 74.0) p=0.99	-16.0 (-90 to 56) p=0.68	-10.0 (-85 to 65) p=0.79	11 (-5 to 27) p=0.1849	70.0 (17 to 123) p=0.009
Amylase (U/L)	751.0 (536 to 965) p<0.001	-0.3 (-238.0 to 237.4) p=0.99	-5.0 (-243 to 232) p=0.96	134.0 (-103 to 371) p=0.26	30 (-21 to 82) p=0.24	-138.0 (-308 to 31) p=0.10
AST (U/L)	199.0 (106 to 291) p<0.001	-88 (-194 to 17) p=0.09	-15.0 (-120 to 90) p=0.77	11.0 (-95 to 118) p=0.83	-4 (-27 to 19) p=0.75	85.0 (10 to 160) p=0.02
Bicarbonate TCO2 (mmol/L)	21.0 (19 to 22) p<0.001	0.11 (-2.00 to 2.00) p=0.89	1.0 (-1 to 2) p=0.37	1.0 (-1 to 3) p=0.26	-0.2 (-1.0 to 0.1) p=0.18	-2.0 (-3.0 to -0.4) p=0.007
BUN (mg/dL)	29.0 (27 to 31) p<0.001	0.2 (-2.2 to 3.0) p=0.89	-2.0 (-4.0 to 0.1) p=0.20	-2.0 (-4 to 1) p=0.12	0.1 (-0.5 to 0.6) p=0.83	-3.0 (-5 to -1) p<0.001
Calcium (mg/dL)	11.0 (10 to 11) p<0.001	-0.02 (-0.30 to 0.21) p=0.8557	0.04 (-0.20 to 0.30) p=0.74	-0.1 (-0.3 to 0.2) p=0.61	0.05 (-0.004 to 0.100) p=0.07	-0.5 (-1.0 to -0.3) p<0.001*
Cholesterol (mg/dL)	89.0 (83 to 96) p<0.001	0.02 (-7.10 to 7.12) p=0.99	4.0 (-3 to 11) p=0.31	5.0 (-3 to 12) p=0.20	3 (1 to 4) **p<0.001***	-22.0 (-27 to -17) p<0.001*
Creatine kinase (U/L)	1162.0 (311 to 2012) p=0.009	-883 (-1825 to 60) p=0.06	64.0 (-876 to 1004) p=0.89	242.0 (-700 to 1182) p=0.61	65 (-140 to 270) p=0.53	608.0 (-63 to 1280) p=0.07
Globulin (g/dL)	2.2 (2.1 to 2.3) p<0.001	0.01 (-0.10 to 0.10) p=0.80	0.005 (-0.100 to 0.102) p=0.92	0.01 (-0.10 to 0.10) p=0.86	0.02 (0.003 to 0.050) p=0.02	-0.3 (-0.4 to -0.3) p<0.001*
LDH (U/L)	524.0 (294 to 753) p<0.001	-221 (-475 to 33) p=0.08	-41.0 (-294 to 213) p=0.75	-26.0 (-280 to 228) p=0.84	24 (-31 to 80) p=0.38	212.0 (31 to 393) p=0.02
Lipase (U/L)	11.0 (-136 to 157) p=0.10	-7 (-169 to 155) p=0.92	0.4 (-161.1 to 162.0) p=0.99	114.0 (-47 to 275) p=0.16	18 (-17 to 53) p=0.31	65.0 (-51 to 180) p=0.27
Phosphorus (mg/dL)	12.0 (11 to 12) p<0.001	-1 (-2.0 to -0.4) p=0.003	0.2 (-0.4 to 1.0) p=0.54	0.2 (-0.5 to 1.0) p=0.61	-0.03 (-0.20 to 0.10) p=0.64	-0.1 (-0.5 to 0.4) p=0.71
Total Protein (g/dL)	5.0 (5 to 6) p<0.001	0.05 (-0.12 to 0.21) p=0.59	-0.01 (-0.20 to 0.20) p=0.86	-0.1 (-0.3 to 0.1) p=0.29	0.01 (-0.03 to 0.04) p=0.65	-0.2 (-0.3 to -0.1) p=0.005
Triglycerides (mg/dL)	141.0 (125 to 157) p<0.001	3 (-15 to 21) p=0.74	0.02 (-18.00 to 18.00) p=0.99	4.0 (-14 to 21) p=0.69	2 (-2 to 6) p=0.29	-47.0 (-60 to -34) p<0.001*
Uric Acid (mg/dL)	4.0 (4 to 5) p<0.001	-0.05 (-0.63 to 0.53) p=0.86	0.3 (-0.3 to 1.0) p=0.36	1.0 (0.3 to 2.0) **p = 0.001***	-0.002 (-0.130 to 0.124) p=0.97	-1.0 (-1.0 to -0.5) p<0.001*

Cholesterol levels exhibited a modest statistically significant increase of approximately 3% per doubling of DPI ($p<0.001$, Cohen's $d= 0.36$) following IVT injection, independent of the injectate (AuNRs or PBS). This effect remained significant even after adjusting for age, indicating that the increase is unlikely to be solely attributable to normal aging processes. Additionally, DPI was associated with a reduction in the ALB/GLOB decreasing by approximately 2% per doubling of DPI ($p = 0.002$) again irrespective of the injectate. Adjusting for age did not change this association, suggesting that factors beyond aging may be contributing to altered protein homeostasis following IVT injection.

Uric acid levels were slightly elevated, by approximately 22%, in animals receiving 25-nm bare-AuNRs ($p = 0.001$, Cohen's $d= 0.32$) indicating a potential conjugation-dependent response in purine metabolism or renal handling. Lastly, we observed sex differences across multiple parameters, consistent with prior previous reports of sex-based variability in systemic biomarker profiles [169,170].

Table 4 Summary of generalized linear regression results for complete blood count (CBC) parameters. The format follows that of Table 1, with coefficients, 95% confidence intervals, and p-values shown for each predictor. Statistical significance was defined as $p < 0.003$ following Bonferroni correction for multiple comparisons. A dagger symbol (†) is used in place of an asterisk where the DPI effect may reflect aging (see study design). Each parameter was evaluated across a total of 96 response measurements.

Parameter	Intercept	AuNR	AuNR size	AuNR conjugation	DPI	Sex
Basophil (/μL)	10 (5 to 14) p<0.001	-7 (-11 to -2) p=0.005	2.0 (-3 to 7) p=0.41	0.04 (-5.0 to 5.0) p=0.98	1.3 (0.3 to 2.4) p=0.009	6.0 (3 to 10) p<0.001*
Eosinophil (/μL)	122 (83 to 160) p<0.001	-20 (-63 to 23) p=0.35	-8.0 (-51 to 35) p=0.70	2.0 (-41 to 45) p=0.92	-5.0 (-15 to 4) p=0.27	22.0 (-9 to 52) p=0.16
HGB (g/dL)	15 (15 to 16) p<0.001	0.01 (-0.50 to 0.51) p=0.96	0.03 (-0.48 to 0.51) p=0.90	0.3 (-0.2 to 1.0) p=0.23	-0.1 (-0.20 to 0.02) p=0.12	0.3 (-0.1 to 1.0) p=0.15
Lymphocyte (/μL)	5492 (4421 to 6564) p<0.001	-483 (-1672 to 706) p=0.42	302.0 (-887 to 1491) p=0.61	1266.0 (78 to 2455) p=0.03	82.0 (-176 to 339) p=0.53	661.0 (-179 to 1502) p=0.12
MCHC (g/dL)	25 (24.5 to 25.5) p<0.001	0.3 (-0.2 to 1.0) p=0.25	0.02 (-1 to 1) p=0.94	0.1 (-0.5 to 1.0) p=0.70	-0.02 (-0.20 to 0.10) p=0.66	2.0 (1.6 to 2.4) p<0.001*
MCV (fL)	56 (55 to 57) p<0.001	-1 (-3 to -0.3) p=0.01	0.3 (-1.0 to 1.4) p=0.66	0.3 (-1.0 to 1.4) p=0.66	0.2 (-0.1 to 0.4) p=0.21	-3.0 (-4 to -2) p<0.001*
Monocyte (/μL)	291 (170 to 412) p<0.001	-56 (-191 to 79) p=0.41	55.0 (-80 to 190) p=0.42	62.0 (-73 to 196) p=0.36	71.0 (42 to 101) **p<0.001†**	65.0 (-30 to 160) p=0.18
Neutrophil (/μL)	989 (756 to 1223) p<0.001	-196 (-455 to 63) p=0.13	12.0 (-247 to 270) p=0.92	56.0 (-202 to 315) p=0.66	52.0 (-5 to 108) p=0.07	-273.0 (-456 to -90) p=0.003*
Platelet count (K/μL)	715 (562 to 867) p<0.001	36 (-133 to 205) p=0.67	-42.0 (-211 to 128) p=0.62	75.0 (-94 to 244) p=0.38	33.0 (-3 to 70) p=0.07	74.0 (-46 to 193) p=0.22
RBC (M/μL)	11 (10 to 11) p<0.001	0.14 (-0.21 to 0.50) p=0.43	-0.1 (-0.4 to 0.3) p=0.77	0.1 (-0.2 to 0.5) p=0.51	-0.1 (-0.200 to 0.001) p=0.05	-0.04 (-0.30 to 0.21) p=0.74
Reticulocyte (%)	3 (2.5 to 3) p<0.001	-0.05 (-0.30 to 0.21) p=0.72	0.1 (-0.2 to 0.4) p=0.42	0.1 (nan to nan) p=0.48	-0.005 (-0.100 to 0.050) p=0.84	-0.1 (-0.2 to 0.1) p=0.49
WBC (K/μL)	7 (6 to 8) p<0.001	-1 (-2 to 1) p=0.27	0.4 (-1.0 to 2.0) p=0.60	1.4 (0.02 to 3.0) p=0.047	0.2 (-0.1 to 0.5) p=0.18	0.5 (-0.5 to 1.4) p=0.33

CBC analysis revealed a gradual 25% increase in monocyte levels ($p < 0.001$) which was attributed to aging, consistent with previous reported age-related shifts in hematologic profiles [171]. Additionally we observed statistically significant sex-related differences, across multiple CBC parameters, aligning with established literature documenting sex-specific hematological baselines in murine models [169,170].

Hypothesis 2g: IVT AuNRs do not increase the number of caspase III positive cells in the retina

To test whether IVT AuNRs induce retinal apoptosis, we performed caspase-III-immunofluorescence and quantified the number of caspase III positive cells in three retinal layers: the GCL, INL and ONL. Animals received either 25-nm Thy-AuNRs, or PBS (sham injection), and caspase III positive cells were quantified in retinal sections.

We observed no meaningful increase in caspase III positive cell counts in Thy-AuNR-injected retinas relative to PBS controls across all three layers. Effect sizes, assessed using Cohen's d, were < 0.25 for both the INL and ONL—well below the threshold for clinical relevance in biomedical research. Importantly, given the large sample size (~10^4 cells), even statistically significant differences in means would not reflect meaningful biological effects when the effect size remains this small. These findings indicate that IVT administration of 25-nm Thy-AuNRs does

not induce detectable retinal apoptosis. Representative images and quantitative results are shown in Figure 36 and in Figure 37.

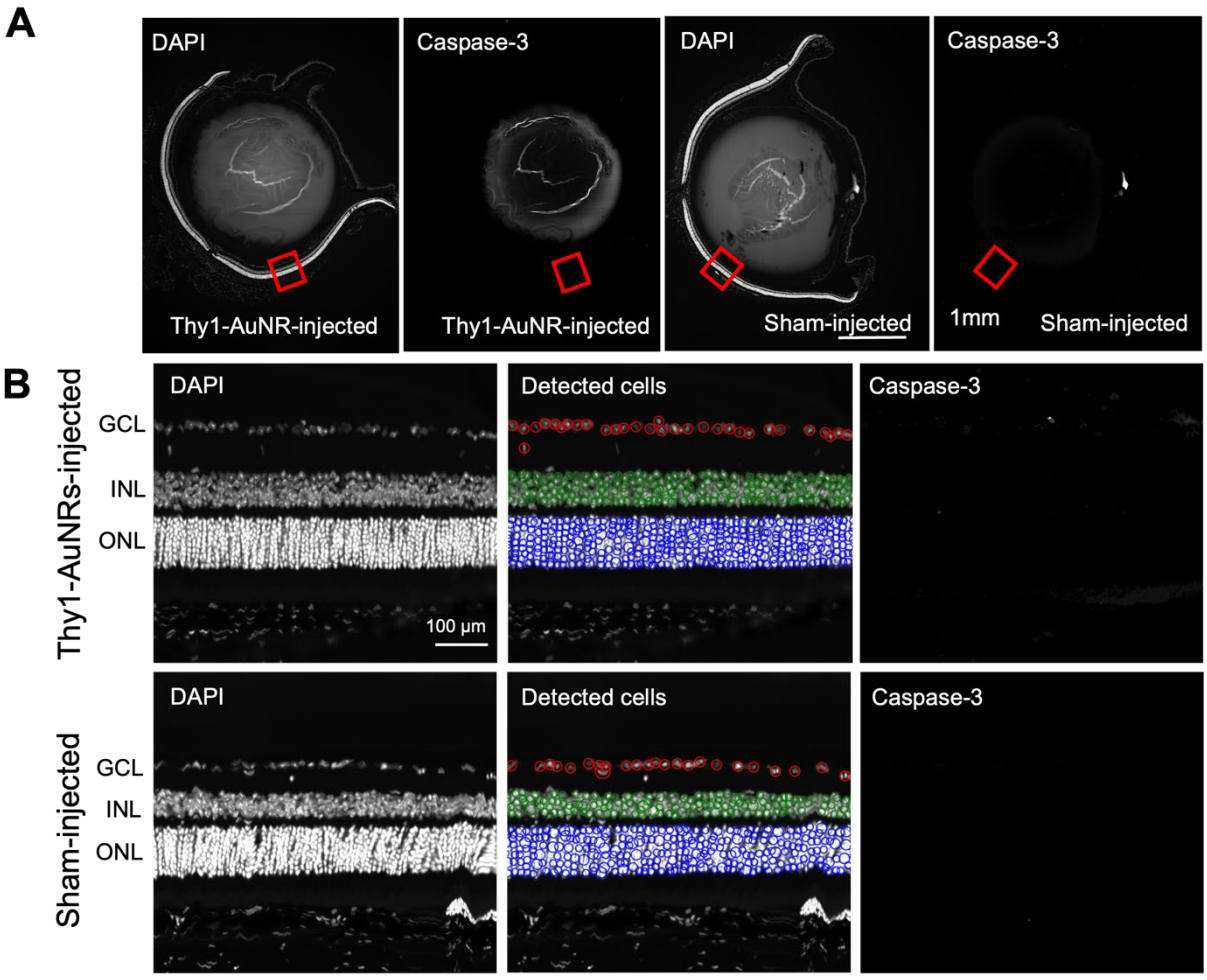

Figure 36 Representative fluorescent image of caspase III immunohistology conducted on retinal tissue sections. 25-nm Thy-AuNR groups were compared to sham-injected groups, eyes were collected at 128 DPI (A) whole retina images displaying the ROI shown in image (B). (B) cross sections showing cellular details for 2 channels (DAPI and caspase-3), middle column displays the cell detection conducted by our custom algorithm (see study design for more details).

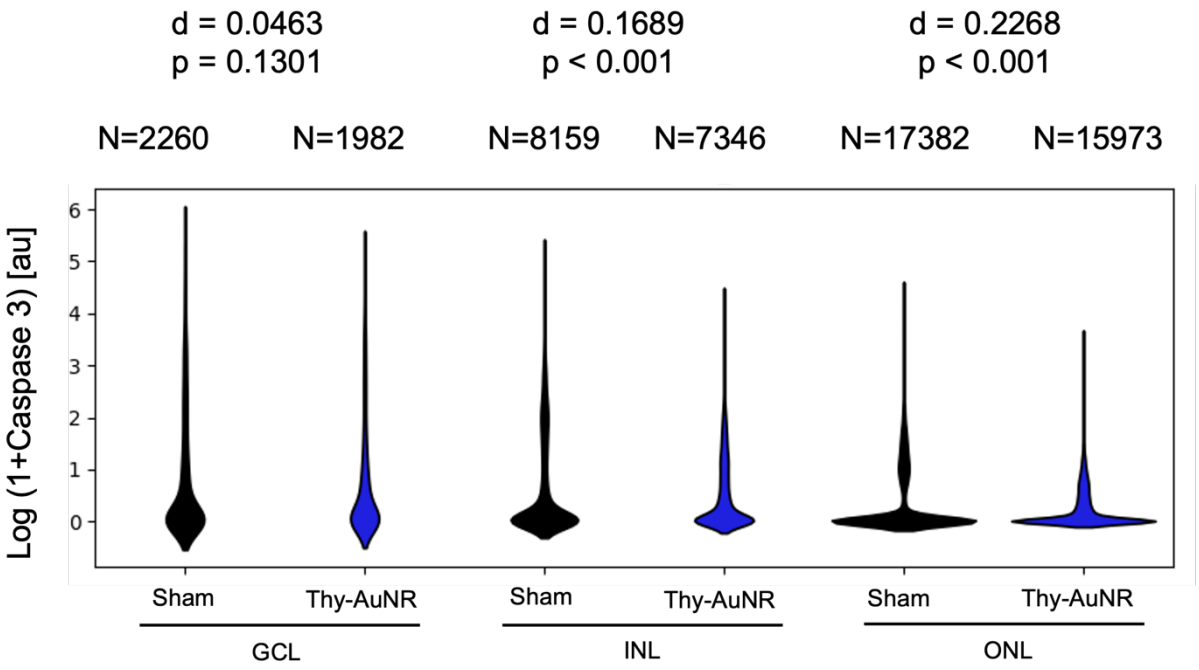

Figure 37 Violin plots displaying the statistical results and log transformed data for fluorescent intensity in the caspase III channel. Cohen's d values are displayed alongside p-values, and total number of cells for each respective layer.

3.5. Discussion

Effect of AuNR concentration

We conducted two complementary assessments of systemic toxicity using complete blood counts (CBC) and serum biochemical analyses. The first set of analyses evaluated the impact of gold-nanorod (AuNR) concentration following IVT injection, while the second assessed the effects of AuNR physiochemical parameters—including size, surface conjugation, and days post injection (DPI).

Our analysis revealed that AuNR concentration exerted a statistically significant effect on circulating monocyte levels with the high concentration group (15 nM) exhibiting a reduction of -235/μL compared to controls (95% CI: 91-378, p

= 0.002), corresponding to a large effect size (Cohen's d = - 0.98). Among all hematological parameters tested, monocytes emerged as the most sensitive indicator of AuNR exposure, suggesting their central role in nanoparticle clearance or trafficking. This aligns with the established role of monocytes/macrophages in phagocytosis of engineered nanomaterials. This reduction in monocytes may indicate an inflammatory response [172–174].

However, other inflammatory markers, including white blood cell count (WBCs), neutrophils, lymphocytes, eosinophils, basophils, and platelet, were not significantly altered by AuNR concentration following a single IVT dose. This observed decline in circulating monocyte levels may reflect increased monocyte recruitment into sites of inflammation, such as the retina, or direct immunomodulatory effects of the nanoparticles on monocytic lineage cells. However, the absence of changes in other leukocyte populations makes the latter explanation less likely. Instead, the hypothesis of monocyte trafficking is more consistent with previous findings and the established immunological response to engineered nanomaterials.

No significant alterations were detected in serum biochemical markers of organ function (e.g., ALT, AST, BUN, creatinine), suggesting that acute or systemic organ toxicity was not induced at either tested concentration. This stands in contrast to previous studies demonstrating dose-dependent systemic toxicity from systemically delivered AuNPs, particularly in the kidneys, liver and spleen. For example, Zhang et al.[161], reported WBC elevation in response to AuNPs, indicative of systemic inflammation, while Cho et al.[175] observed upregulation of

inflammatory cytokines following systemic nanoparticle distribution and organ sequestration.

Our findings are further supported by the study from Sandrian et al. [125], who observed increased ocular neutrophil infiltration following IVT injection of Thy-AuNRs, suggesting local inflammatory responses. While their study was limited to a short 24-hour time point, our data collected at 128 DPI may reflect the long-term consequences of persistent AuNR presence in the ocular compartment. Given the previously estimated 98-day half-life of 25-nm Thy-AuNRs in the retina, the chronic presence of nanoparticles, particularly at higher concentrations, could provoke sustained low-grade inflammation.

Although Sandrian et al. did not specify the concentration of their injected AuNR formulation, the absence of systemic organ toxicity in our study, paired with a significant monocyte reduction, supports the possibility of monocyte migration toward a site of chronic inflammation, likely the retina. This concentration-dependent effect is further reinforced by the lack of significant monocyte reduction in the moderate concentration group (4 nM), highlighting a potential threshold effect.

An alternative explanation involving AuNR induced immunosuppression or selective monocyte suppression cannot be completely ruled out, although it remains less consistent with our overall leukocyte profile. Further investigation is warranted to validate the inflammatory trafficking hypothesis, including direct assessment of monocyte infiltration and inflammatory cytokine expression within the ocular environment.

In summary, these findings suggest a concentration-dependent, systemic immunological response to IVT-injected AuNRs, with implications for monocyte redistribution and possible chronic retinal inflammation at high nanoparticle doses. Follow-up studies examining ocular inflammatory markers and tissue histopathology are needed to further elucidate the downstream consequences of AuNR exposure and to guide future nanomaterial design for intraocular use.

Effect of conjugation

To evaluate the role of surface conjugation, we compared systemic responses following IVT injection of 25-nm Thy-AuNRs and 25-nm bare-AuNRs (lacking Thy conjugation). A marginal but statistically significant elevation in uric acid (22% increase, Cohen's d= 0.3) was observed in the bare-AuNR group. Interestingly, Lasagna-Reeves et al. [176], reported a similar 22% increase in uric acid levels after intraperitoneal (IP) administration of AuNPs at 400 μg/kg/day, although the increase in their study did not reach significance ($p > 0.05$). In our case, the change followed a single IVT dose (150 μg/kg), suggesting that bare-AuNRs may have entered systemic circulation despite the localized administration route.

Renal toxicity is typically assessed using BUN, creatinine, and the BUN/creatinine ratio [161,176,177]. Additional indicators such as uric acid, chloride and bicarbonate TCO_2, while less specific, can provide broader context for renal and electrolyte balance [176,178]. In our dataset, all remined unaltered except uric acid, supporting the interpretation of a minimal systemic impact with only a subtle renal-related response.

The hypothesis that conjugation reduces systemic toxicity risk (through reducing systemic distribution) is supported by two findings: (1) elevated uric acid was only observed in the bare-AuNR group, and (2) bare-AuNRs showed significantly lower two-photon luminescence (TPL) signal intensity compared to Thy-AuNRs (*see Chapter 2*). These results suggest that surface conjugation, such as Thy-antibodies, helps anchor AuNRs in the retina and prevents their redistribution to the systemic circulation.

Our results align with prior work showing that surface chemistry shapes the toxicity profile of AuNPs. For example, Simpson et al. reported hematological stability with glutathione-coated ultrasmall AuNPs [164], while Zhang et al. observed size dependent changes in WBC and liver enzymes (ALT and AST) [161]. In Simpson's case, both ultrasmall size and glutathione coating likely contributed to rapid renal clearance and biocompatibility. These comparisons highlight that nanoparticle size and surface chemistry are interdependent variables shaping *in-vivo* distribution: sub-5.5 nm particles are cleared renally, whereas larger particles (like our ~25 nm × 119 nm AuNRs) persist systemically unless conjugated to targeting antibodies or ligands.

Because both bare- and Thy- AuNRs were synthesized using the same protocols, surfactant residues are unlikely to explain the observed uric acid increase. Surfactant-related toxicity has been reported [125,179,180], but our design controls for this variable, pointing instead to conjugation as the decisive factor.

An alternative explanation for the uric acid increase is that bare AuNRs triggered purine release as a downstream product of DNA degradation. However,

this scenario is unlikely since DNA damage sufficient to elevate uric acid would also be expected to alter additional organ-health biomarkers, which we did not observe. To fully rule out renal damage, comprehensive histological evaluation of the kidney will be necessary, potentially incorporating assays such as lipid peroxidation, TUNEL or Caspase-III staining, alongside microstructural assessment.

Taken together, our findings underscore the role of surface conjugation in mitigating systemic redistribution and toxicity following IVT injection. In the context of ocular drug delivery, this has important implications: non-conjugated nanoparticles may more easily cross into systemic circulation, while surface-modified particles achieve better localization and safety. This challenges the assumption that the murine BRB prevents ocularly delivered particles from entering systemic circulation. Kim et al. showed a size-dependent permeability to intravenously delivered AuNSs [160], and our results suggest that conjugation is an equally decisive factor when delivery is ocular. This shifts the design focus for ocular nanomedicines: strategies should both minimize systemic exposure through conjugation and actively examine downstream systemic effects to ensure overall biocompatibility.

Effect of DPI

Doubling of DPI led to a modest 2% reduction in the ALB/GLOB ratio, regardless of whether AuNRs or PBS were injected. While statistically significant, this effect is small and remains well within normal physiological limits (typically 1.0-2.0). Furthermore, the absence of changes in other liver-associated markers (e.g.,

ALT, AST, ALP) suggests that the decline in ALB/GLOB does not reflect hepatic dysfunction. Instead, it may indicate a mild shift in protein turnover or immune status over time post-injection, independent of injectate composition.

Cholesterol levels increased slightly but significantly (~ 3% per doubling of DPI, Cohen's d = 0.36). This trend persisted even after adjusting for age as a covariate (*see methods*), indicating that it is unlikely to be purely age-related. However, given the well-known fluctuations of cholesterol with age, this finding should be interpreted cautiously. For context, Mazzacara et al. reported a 75-100% increase in cholesterol levels in 4- to- 12 month-old female mice compared to 2-month old females, highlighting the magnitude of age-related variation [170]. Importantly, AuNR presence did not independently affect cholesterol levels, supporting the interpretation that this is a time-dependent, non-toxic phenomenon.

We also observed a 25% increase in circulating monocytes with advancing DPI, consistent with age-associated immune shifts. After adjusting for age as a covariate, the DPI effect on monocytes was no longer significant, indicating it was primarily an aging effect. Duong et al. documented a 67% increase in monocyte levels in adults versus young mice, emphasizing this age-related trend [171]. In our dataset, monocyte changes were not attributable to AuNR exposure, except in the high-concentration group (*see prior section for effect of concentration*), where reductions appeared nanoparticle-related rather than age related.

Viewed in context, these small but consistent DPI-related shifts in ALB/GLOB ratio and cholesterol likely reflect a mild physiological response to the IVT procedure itself, rather than AuNR induced toxicity. Although AuNR presence

was modeled as a covariate, these effects were observed regardless of injectate, suggesting they stem from the injection process or sustained intraocular presence of exogenous material rather than particle-specific properties. Overall, biomarker levels remained relatively stable over time following IVT injection.

Albumin levels and globulin levels were not independently significant; rather, the ratio between them was influenced by DPI, decreasing by ~2% per doubling. Values started higher at low DPI and gradually declined. Albumin is a negative acute-phase protein, whereas globulins rise in response to inflammation; thus, the declining ratio may indicate a mild systemic response to IVT injection rather than hepatic involvement. This conclusion is reinforced by the lack of DPI (or AuNR-related) effects on hepatic serum biomarkers (ALT, AST, ALP, BUN, creatinine, BUN/creatinine ratio, TBIL, and TP; Table 3). Interestingly, TP represents the sum of ALB and GLOB, and its stability indicates that while the ratio shifted, total protein levels remain unchanged.

The modest DPI-associated rise in cholesterol, while statistically significant, remained within physiological ranges and is unlikely to indicate hepatic dysfunction. Lipid metabolism is liver-regulated, but the absence of AuNR-related effects suggests this change reflects mild systemic or environmental factors, such as reduced activity in longer-DPI mice, rather than hepatic injury, Hepatic assays could be used to confirm the lack of nanoparticle-induced toxicity.

Effect of sex

We observed differences in several parameters between male and female mice, highlighting the importance of considering sex as a biological variable in systemic toxicity assessments. These sex-based differences (Table 3 and Table 4) broadly align with previously reported values in the literature. In the CBC data, HCT, MCV, MCH, MCHC, and basophil counts all showed significant variations by sex. Notably, basophil counts were lower in females by approximately 6% (Cohen's d = 0.26), consistent with prior findings.

Chen et al.[181] examined the effects of intravenously (IV) administered AuNPs of varying sizes (4.4-, 22.5-, 29.3-, and 36.1-nm), on hematological parameters and biochemical parameters at 28 DPI. Their findings indicated sex-dependent alterations in a wide range of markers including WBC, RBC, HGB, HCT, MCH, MCHC, ALT, AST, creatinine, albumin, and total bilirubin. Interestingly, the toxicity profile varied by both nanoparticle size and sex: smaller AuNPs (4.4- and 22.5-nm) induced more profound liver damage in males, while intermediate and larger AuNPs (22.5-, 29.3- and 36.1-nm) produced more kidney toxicity in females. The largest AuNPs (36.1-nm) also affected spleen indices in both sexes.

In contrast to these findings, our study did not identify AuNR-induced perturbations in hematological or serum biochemical parameters across sexes. The sex-related differences we observed appear to reflect normal physiological variation rather than an interaction with AuNR exposure.

Effect on retinal apoptosis:

We assessed apoptotic activity in the retina using activated caspase III immunolabeling in mice at 128 DPI following IVT injection of either PBS (sham), or 25-nm Thy-AuNRs. The results indicated no clinically relevant difference in the number of caspase III positive cells between AuNR and PBS IVT injected animals (Cohen's $d < 0.25$), suggesting that 25-nm Thy-AuNRs did not induce significant retinal apoptotic toxicity at this timepoint. Our earlier findings demonstrated a reduction in circulating monocyte counts following high-concentration AuNR exposure, suggesting plausible recruitment of monocytes to ocular tissues.

Given that this effect persisted at 128 DPI, it is consistent with a sustained inflammatory response. Chronic inflammation in the retina is a well-documented trigger of apoptosis. However, this inflammatory effect was not observed in animals treated with the moderate concentration of 25-nm Thy-AuNRs, nor did we observe an increase in caspase-III positive cells in these animals. Together, these results suggest that targeted AuNR delivery via Thy-conjugation mitigates both ocular inflammatory responses and retinal apoptotic risk, even after prolonged intraocular residence.

These observations align with previous reports of ocular biocompatibility of AuNPs. Bakri et al.[166], demonstrated no morphological abnormalities up to 6 months after IVT delivery of AuNRs in rabbits. Similarly, Song et al.[130], assessed apoptosis in mouse retinas using terminal deoxynucleotidyl transferase-mediated dUTP nick-end labeling (TUNEL) after IVT injection of gold nano disks (AuNDs), and similarly found no significant difference between AuND- and vehicle-treated

groups. Kim et al. [160] showed that intravenously delivered AuNPs traversed the BRB, and accumulated in retinal layers without affecting retinal morphology nor apoptosis, as assessed by H&E and TUNEL staining, respectively, up to 7 DPI.

Our findings contribute to this body of evidence by extending the assessment window to 128 DPI and by including a quantitative apoptosis assay. While most previous studies have focused on short-term outcomes or morphological metrics, our data provide additional insight into the long-term retinal safety of IVT-delivered AuNRs.

Nevertheless, the inflammation observed following administration of high-concentration AuNRs, combined with pro-apoptotic consequences of chronic inflammation, suggests a potential for retinal toxicity at higher doses and longer durations. Thus, careful optimization of AuNR dose, conjugation strategy, and particle design will be essential to ensuring both efficacy and biocompatibility in future clinical translation of a plasmonic retinal prosthesis.

4. Chapter 4: Outlook

4.1. Implications of delivery and toxicity data in the development of a plasmonic retinal prosthesis

Our delivery and toxicity assessments yielded the following key findings:

Delivery findings:

1a) Intravitreal (IVT) injection effectively delivers AuNRs to the retina via the vitreous humor (VH) and the inner limiting membrane (ILM)

1b) Enzymatic degradation of the ILM did not enhance AuNR diffusion to the retina

1c) Anti-thy conjugation significantly increased retinal accumulation of AuNRs

1d) AuNR size significantly influenced retinal diffusion dynamics

1e) Retinal AuNR content decreased with increasing days post-injection (DPI)

1f) Thy-AuNRs localized to the ganglion cell layer (GCL), the inner plexiform layer (IPL) and the outer plexiform layer (OPL)

Toxicity findings:

2a) IVT AuNRs did not cause severe systemic toxicity

2b) Higher concentrations weakly increased systemic toxicity risk

2c) Size did affect systemic toxicity risk

2d) Bare (non-targeting) AuNRs slightly elevated systemic toxicity risk

2e) Toxicity risk was independent of DPI

2f) Toxicity risk did not differ between sexes

2g) IVT Thy-AuNRs did not increase retinal apoptosis

These findings form a crucial foundation for the development of a minimally invasive, near-infrared (NIR) driven plasmonic retinal prosthesis (PRP). By identifying anti-Thy targeting as a critical determinant of successful intraretinal delivery and demonstrating the sustained retinal presence of AuNRs post-injection, we provide both mechanistic insight and translational validation for AuNR-based bio interfaces. The capacity to target both ganglion and bipolar cells via Thy-antigen expression aligns with trends in subretinal photovoltaic devices, positioning AuNRs as a compelling alternative by enabling photothermal, rather than electrical, stimulation.

Importantly, the tunability of AuNRs in both size and surface chemistry presents opportunities for future optimization of biodistribution, retention, and stimulation efficiency. Collectively, our results support the feasibility of a non-genetic, outpatient-deployable PRP platform with clinically scalable potential.

While ILM degradation did not improve AuNR delivery to the retina in the murine model, this may not generalize to humans, where the ILM is thicker and more structurally complex. In clinical contexts, both pharmacologic vitreolysis and mechanical ILM peeling have been safely implemented to enhance retinal access. Such approaches may prove necessary in scaling this platform to larger animal models or human subjects.

We also showed that 25-nmThy-AuNRs achieved higher retinal accumulation, and lower risk of systemic toxicity than bare AuNRs of the same size. These findings emphasize the importance of targeted delivery for both efficacy and safety. Nonetheless, the antibody conjugation and purification protocols must be

tightly controlled to minimize residual synthesis byproducts, such as surfactants, that have been associated with toxicity. Rigorous purification and characterization will be essential when advancing to preclinical or clinical-grade production.

The estimated half-life of AuNRs in our study was ~100 days, supporting the notion that a PRP based on this platform could maintain function for at least three months post-injection. This contrasts with the high maintenance demands of traditional electrical prostheses, which often fail due to electrode degradation, waning efficiency, or mechanical complications. A PRP based on IVT-delivered AuNRs may require only periodic outpatient dosing, significantly reducing procedural burden and long-term cost. Unlike defunct electronic prosthetic systems, which left users without support, this approach offers a pathway toward sustainable patient care.

The retinal localization of Thy-AuNRs to the ganglion cell layer (GCL), inner plexiform layer (IPL), and outer plexiform layer (OPL), reinforces their specificity for inner retinal neurons with minimal off-target distribution. In a separate study [117], we showed that these AuNRs can modulate bipolar cell activity suggesting that the PRP could restore visual signals that are biologically meaningful.

Our toxicity data confirmed the general safety of IVT injection for AuNR delivery. However, higher concentration led to sustained inflammation persisting to 128 DPI, indicating that the effects of a single high-dose IVT injection may be chronic. This finding highlights the need to carefully balance delivery efficiency and safety.

Interestingly, while size significantly affected retinal accumulation, it was not predictive of systemic toxicity. Smaller AuNRs exhibited lower retinal retention, likely due to increased clearance, a trend observed in prior studies. Given their high absorption cross-section, larger AuNRs may ultimately be better suited for neuromodulation, provided toxicity remains low. Thus, the relationship between particle size, retention, stimulation efficiency, and clearance remain a critical area for further exploration.

Perhaps the most consequential finding from this study is the role of surface conjugation in modulating both retinal delivery and systemic toxicity. The increased risk of toxicity with bare AuNRs highlights the importance of targeted delivery, not just for enhancing efficacy but for ensuring safety and biocompatibility. As the PRP platform advances towards clinical translation, improving targeting will be vital.

We evaluated toxicity up to 128 DPI and found that DPI itself did not predict systemic or ocular toxicity. This is particularly important given that previous AuNR-based ocular studies examined outcomes only up to 7 DPI. Given the kinetics of AuNR migration and accumulation in the retina, this longer time window strengthens the case for safety.

Across both systemic and ocular analyses, DPI had no appreciable influence on toxicity parameters. Apoptotic cell counts in AuNR-treated retinas did not differ from sham-injected controls, further supporting the ocular safety of the AuNR platform. Future work may benefit from assessing ocular toxicity at multiple earlier timepoints to complement our long-term observations and clarify the temporal safety profile.

Finally, the absence of sex-based differences in toxicity outcomes expands the potential applicability of the PRP across patient populations. Nonetheless, given established sex differences in nanoparticle clearance, hematological responses, and organ distribution, future validation efforts must continue to include sex as a variable to ensure robust, generalizable safety profiles. The next section will comment on future directions for the validation of the PRP platform.

4.2. Future directions

The development of a plasmonic retinal prosthesis based on intravitreally injected AuNRs presents a novel paradigm for a minimally invasive, wireless, cell-targeted retinal stimulation. Our findings lay the foundation for this platform, yet several critical areas must be addressed to optimize delivery, enhance efficacy, and ensure translational readiness. Future studies should pursue the following directions:

Optimization of AuNR size and delivery efficiency

We demonstrated enhanced retinal accumulation of 25-nm AuNRs compared to 10-nm counterparts, highlighting size as a key determinant of intravitreal delivery. However, this only represents a narrow segment of the size-performance landscape. Future investigations should systematically examine a broader range of aspect ratios and sizes to identify an optimal configuration that balances physical transport across retinal barriers, membrane binding, and plasmonic resonance properties for effective stimulation.

Inner limiting membrane circumvention in larger models

In mice, enzyme-assisted delivery did not improve inner retinal accumulation, yet in larger animals or humans, robust methods to circumvent the inner limiting membrane may be necessary. Approaches such as pharmacologic loosening of the membrane, transient mechanical disruption, or microneedle-enhanced delivery should be evaluated in species with thicker ILMs (e.g., rabbits or primates) to model the feasibility and safety of human translation.

Refinement of cell-type targeting

Anti-Thy conjugation enabled selective binding to inner retinal neurons, but further refinement is needed to restrict retinal binding specifically to bipolar cells. Using alternative bipolar-specific markers could sharpen spatial precision and enhance the biological relevance of the generated artificial vision signals.

Future studies should investigate Thy-antigen remodeling to determine whether AuNRs are internalized, a process that could elevate ROS and compromise cell viability. This requires precise assessment of membrane binding, intracellular trafficking of AuNRs, and longitudinal ROS quantification across multiple DPIs. Additionally, evaluating the impact of NIR photothermal stimulation on potential disengagement of AuNRs from neuronal membranes will further the safety profile, providing critical data to guide translational, preclinical validation.

Elucidation of clearance kinetics and routes

Currently, nanoparticle persistence is inferred from two-photon luminescence imaging, but direct quantification of ocular clearance remains

limited. OCT based longitudinal imaging in mice can improve interpretability of ocular clearance kinetics by tracking AuNR diffusion through the vitreous within the same animal over multiple timepoints. OCT has previously been used to visualize AuNDs in the vitreous, demonstrating its applicability for monitoring AuNR behavior post-injection.

Future studies should incorporate mass spectrometry-based quantification in ocular tissues and hematological samples to provide absolute AuNR concentrations and directly assess systemic circulation. Additionally, supporting evidence could be obtained by examining splenic accumulation of AuNRs and analyzing excreted materials to corroborate renal and hepatic histology findings. Combined with the OCT measurements, ICP-MS data would provide a robust characterization of AuNR clearance pathways, enhancing our understanding of systemic distribution and clearance dynamics to support clinical translation.

These methods, particularly in larger animals, will clarify whether AuNRs are cleared via anterior chamber pathways or posterior outflow routes, and over what timescale. Conducting these experiments with optimized AuNR parameters, excluding bare AuNRs, can reduce overall animal numbers while maintaining compliance with ethical principles for animal research.

Comprehensive systemic safety profiling

Our hematological and biochemical profiling addressed critical variables relevant to regulatory standards, including sex, time post-injection, and particle characteristics. However, expanding these analyses to include hematological gold

levels, direct organ biodistribution and chronic histopathology would enhance robustness of the safety dataset. Importantly, these assessments should be conducted across multiple doses, conjugates and timepoints to establish a comprehensive and predictive safety model.

Defining dose thresholds for safe and effective use

Concentration emerged as a key determinant of both delivery performance and long-term inflammatory responses. Systematic dose-ranging studies are needed to define an upper threshold that maximizes therapeutic delivery while maintaining ocular and systemic safety. Furthermore, correlating dose with neuromodulatory efficacy will be essential to balance biological effect with toxicity risk.

Expanded timepoint and sex-based toxicity analysis

Our apoptosis data, collected at a moderate dose and late timepoint (128 DPI), suggest minimal retinal toxicity under these conditions. However, a more nuanced understanding will require a matrixed study of apoptosis, and inflammation across multiple doses and DPI values, including early, intermediate, and late stages post-injection. Continued inclusion of sex as a biological variable is critical to maintaining clinical relevance across diverse patient populations.

4.3. Conclusion

This study contributes to the growing body of literature on targeted ocular delivery of nanoparticles and advances our understanding of key ocular barriers. While previous work has demonstrated mouse BRB permeability from systemic

circulation to the retina in a size-dependent manner, our data reveal that bare AuNRs led to secondary systemic effects such as elevated uric acid, suggesting the possibility of nanoparticle redistribution or clearance through the BRB. Although this study did not directly measure AuNRs in blood, organs, or excreted material, future biodistribution investigations will be crucial to address this hypothesis. Our results indicate that surface conjugation, rather than size, is the primary determinant of these effects. These findings can inform future approaches, including ocular cancer ablation or drug-coupled nanoparticle formulations, where targeting moieties may reduce off-target systemic exposure and expand the applications of ocular drug delivery.

Our study is the first to systematically examine systemic toxicity of IVT-delivered AuNRs while varying particle physical and chemical properties. We present a framework for systemic safety profiling in accordance with ISO and FDA standards and provide key recommendations for future validation of IVT AuNR safety. Importantly, the methods described are broadly applicable beyond photothermal neuronal stimulation, including compartmentalized delivery systems and other nanoparticle formulations in the eye or other organs.

Cumulatively, these future directions outline a clear roadmap toward clinical development of the PRP. By refining delivery strategies, optimizing targeting specificity, and completing a regulatory-grade safety profile, this platform holds promise not only for restoring vision in degenerative retinal diseases but also for advancing a broader class of targeted, wireless neuromodulation tools. The data

collected here provide a foundation for studies in higher-order animals and for preparing FDA filing documentation.

Bibliography

1. Yang S, Zhou J, Li D. Functions and Diseases of the Retinal Pigment Epithelium. *Front Pharmacol*. 2021;12. doi:10.3389/fphar.2021.727870

2. Apte RS. Age-Related Macular Degeneration. *N Engl J Med*. 2021;385(6):539-547. doi:10.1056/NEJMcp2102061

3. Wong WL, Su X, Li X, et al. Global prevalence of age-related macular degeneration and disease burden projection for 2020 and 2040: a systematic review and meta-analysis. *Lancet Glob Health*. 2014;2(2):e106-116. doi:10.1016/S2214-109X(13)70145-1

4. Al-Merjan JI, Pandova MG, Al-Ghanim M, Al-Wayel A, Al-Mutairi S. Registered blindness and low vision in Kuwait. *Ophthalmic Epidemiol*. 2005;12(4):251-257. doi:10.1080/09286580591005813

5. Bunker CH, Berson EL, Bromley WC, Hayes RP, Roderick TH. Prevalence of retinitis pigmentosa in Maine. *Am J Ophthalmol*. 1984;97(3):357-365. doi:10.1016/0002-9394(84)90636-6

6. Pascolini D, Mariotti SP. Global estimates of visual impairment: 2010. *Br J Ophthalmol*. 2012;96(5):614-618. doi:10.1136/bjophthalmol-2011-300539

7. Hartong DT, Berson EL, Dryja TP. Retinitis pigmentosa. *Lancet Lond Engl*. 2006;368(9549):1795-1809. doi:10.1016/S0140-6736(06)69740-7

8. Wang AL, Knight DK, Vu TTT, Mehta MC. Retinitis Pigmentosa: Review of Current Treatment. *Int Ophthalmol Clin*. 2019;59(1):263-280. doi:10.1097/IIO.0000000000000256

9. Berson EL, Rosner B, Sandberg MA, et al. Further evaluation of docosahexaenoic acid in patients with retinitis pigmentosa receiving vitamin A treatment: subgroup analyses. *Arch Ophthalmol Chic Ill 1960*. 2004;122(9):1306-1314. doi:10.1001/archopht.122.9.1306

10. Jabbehdari S, Handa JT. Oxidative stress as a therapeutic target for the prevention and treatment of early age-related macular degeneration. *Surv Ophthalmol*. 2021;66(3):423-440. doi:10.1016/j.survophthal.2020.09.002

11. Hussain RM, Shaukat BA, Ciulla LM, Berrocal AM, Sridhar J. Vascular Endothelial Growth Factor Antagonists: Promising Players in the Treatment of Neovascular Age-Related Macular Degeneration. *Drug Des Devel Ther*. 2021;15:2653-2665. doi:10.2147/DDDT.S295223

12. Ahuja AK, Dorn JD, Caspi A, et al. Blind subjects implanted with the Argus II retinal prosthesis are able to improve performance in a spatial-motor task. *Br J Ophthalmol*. 2011;95(4):539-543. doi:10.1136/bjo.2010.179622

13. Dorn JD, Ahuja AK, Caspi A, et al. The Detection of Motion by Blind Subjects With the Epiretinal 60-Electrode (Argus II) Retinal Prosthesis. *JAMA Ophthalmol*. 2013;131(2):183-189. doi:10.1001/2013.jamaophthalmol.221

14. da Cruz L, Dorn JD, Humayun MS, et al. Five-Year Safety and Performance Results from the Argus II Retinal Prosthesis System Clinical Trial. *Ophthalmology*. 2016;123(10):2248-2254. doi:10.1016/j.ophtha.2016.06.049

15. Humayun MS, Dorn JD, da Cruz L, et al. Interim results from the international trial of Second Sight's visual prosthesis. *Ophthalmology*. 2012;119(4):779-788. doi:10.1016/j.ophtha.2011.09.028

16. Stingl K, Bartz-Schmidt KU, Besch D, et al. Subretinal Visual Implant Alpha IMS--Clinical trial interim report. *Vision Res*. 2015;111(Pt B):149-160. doi:10.1016/j.visres.2015.03.001

17. Polikov VS, Tresco PA, Reichert WM. Response of brain tissue to chronically implanted neural electrodes. *J Neurosci Methods*. 2005;148(1):1-18. doi:10.1016/j.jneumeth.2005.08.015

18. Behrend MR, Ahuja AK, Humayun MS, Chow RH, Weiland JD. Resolution of the Epiretinal Prosthesis is not Limited by Electrode Size. *Ieee Trans Neural Syst Rehabil Eng*. 2011;19(4):436-442. doi:10.1109/TNSRE.2011.2140132

19. White J, Knight L, da Cruz L, et al. Effects of the Argus II Retinal Prosthesis System on the Quality of Life of Patients With Ultra-Low Vision Due to Retinitis Pigmentosa: Protocol for a Single-Arm, Mixed Methods Study. *JMIR Res Protoc*. 2021;10(1):e17436. doi:10.2196/17436

20. Ramirez KA, Drew-Bear LE, Vega-Garces M, Betancourt-Belandria H, Arevalo JF. An update on visual prosthesis. *Int J Retina Vitr*. 2023;9(1):73. doi:10.1186/s40942-023-00498-1

21. Seo JM, Kim KH, Goo YS, et al. Vision rehabilitation by electrical retinal stimulation: Review of microelectrode approaches. *Sens Mater*. 2012;24(4):153-164.

22. Stingl K, Zrenner E. Electronic approaches to restitute vision in patients with neurodegenerative diseases of the retina. *Ophthalmic Res*. 2013;50(4):215-220. doi:10.1159/000354424

23. De Rossi F, Guidobaldi M, Turco S, Amore F. Transorbital electrical stimulation in retinitis pigmentosa. Better results joining visual pattern

stimulation? *Brain Stimulat*. 2020;13(5):1173-1174. doi:10.1016/j.brs.2020.05.014

24. Xu H, Zhong X, Pang C, et al. First Human Results With the 256 Channel Intelligent Micro Implant Eye (IMIE 256). *Transl Vis Sci Technol*. 2021;10(10):14. doi:10.1167/tvst.10.10.14

25. Ferlauto L, Airaghi Leccardi MJI, Chenais NAL, et al. Design and validation of a foldable and photovoltaic wide-field epiretinal prosthesis. *Nat Commun*. 2018;9:992. doi:10.1038/s41467-018-03386-7

26. Vagni P, Airaghi Leccardi MJI, Vila CH, et al. POLYRETINA restores light responses in vivo in blind Göttingen minipigs. *Nat Commun*. 2022;13:3678. doi:10.1038/s41467-022-31180-z

27. Menzel-Severing J, Laube T, Brockmann C, et al. Implantation and explantation of an active epiretinal visual prosthesis: 2-year follow-up data from the EPIRET3 prospective clinical trial. *Eye*. 2012;26(4):501-509. doi:10.1038/eye.2012.35

28. Bloch E, Luo Y, da Cruz L. Advances in retinal prosthesis systems. *Ther Adv Ophthalmol*. 2019;11:2515841418817501. doi:10.1177/2515841418817501

29. Ghezzi D. Retinal prostheses: progress toward the next generation implants. *Front Neurosci*. 2015;9:290. doi:10.3389/fnins.2015.00290

30. Mathieson K, Loudin J, Goetz G, et al. Photovoltaic Retinal Prosthesis with High Pixel Density. *Nat Photonics*. 2012;6(6):391-397. doi:10.1038/nphoton.2012.104

31. Lorach H, Goetz G, Smith R, et al. Photovoltaic restoration of sight with high visual acuity. *Nat Med*. 2015;21(5):476-482. doi:10.1038/nm.3851

32. Muqit MMK, Mer YL, Koo LO de, Holz FG, Sahel JA, Palanker D. Prosthetic Visual Acuity with the PRIMA Subretinal Microchip in Patients with Atrophic Age-Related Macular Degeneration at 4 Years Follow-up. *Ophthalmol Sci*. 2024;4(5). doi:10.1016/j.xops.2024.100510

33. Rizzo JF, Wyatt J, Loewenstein J, Kelly S, Shire D. Methods and perceptual thresholds for short-term electrical stimulation of human retina with microelectrode arrays. *Invest Ophthalmol Vis Sci*. 2003;44(12):5355-5361. doi:10.1167/iovs.02-0819

34. Rizzo JF. Update on retinal prosthetic research: the Boston Retinal Implant Project. *J Neuro-Ophthalmol Off J North Am Neuro-Ophthalmol Soc*. 2011;31(2):160-168. doi:10.1097/WNO.0b013e31821eb79e

35. Petoe MA, Titchener SA, Kolic M, et al. A Second-Generation (44-Channel) Suprachoroidal Retinal Prosthesis: Interim Clinical Trial Results. *Transl Vis Sci Technol*. 2021;10(10):12. doi:10.1167/tvst.10.10.12

36. Eggenberger SC, James NL, Ho C, et al. Implantation and long-term assessment of the stability and biocompatibility of a novel 98 channel suprachoroidal visual prosthesis in sheep. *Biomaterials*. 2021;279:121191. doi:10.1016/j.biomaterials.2021.121191

37. Nishida K, Sakaguchi H, Kamei M, et al. Visual Sensation by Electrical Stimulation Using a New Direct Optic Nerve Electrode Device. *Brain Stimulat*. 2015;8(3):678-681. doi:10.1016/j.brs.2015.03.001

38. Chow AY, Chow VY, Packo KH, Pollack JS, Peyman GA, Schuchard R. The artificial silicon retina microchip for the treatment of vision loss from retinitis pigmentosa. *Arch Ophthalmol Chic Ill 1960*. 2004;122(4):460-469. doi:10.1001/archopht.122.4.460

39. Chow AY, Bittner AK, Pardue MT. The artificial silicon retina in retinitis pigmentosa patients (an American Ophthalmological Association thesis). *Trans Am Ophthalmol Soc*. 2010;108:120-154.

40. Zrenner E. Fighting blindness with microelectronics. *Sci Transl Med*. 2013;5(210):210ps16. doi:10.1126/scitranslmed.3007399

41. Duebel J, Marazova K, Sahel JA. Optogenetics. *Curr Opin Ophthalmol*. 2015;26(3):226. doi:10.1097/ICU.0000000000000140

42. Bi A, Cui J, Ma YP, et al. Ectopic expression of a microbial-type rhodopsin restores visual responses in mice with photoreceptor degeneration. *Neuron*. 2006;50(1):23-33. doi:10.1016/j.neuron.2006.02.026

43. Lagali PS, Balya D, Awatramani GB, et al. Light-activated channels targeted to ON bipolar cells restore visual function in retinal degeneration. *Nat Neurosci*. 2008;11(6):667-675. doi:10.1038/nn.2117

44. Doroudchi MM, Greenberg KP, Liu J, et al. Virally delivered channelrhodopsin-2 safely and effectively restores visual function in multiple mouse models of blindness. *Mol Ther J Am Soc Gene Ther*. 2011;19(7):1220-1229. doi:10.1038/mt.2011.69

45. Macé E, Caplette R, Marre O, et al. Targeting channelrhodopsin-2 to ON-bipolar cells with vitreally administered AAV Restores ON and OFF visual responses in blind mice. *Mol Ther J Am Soc Gene Ther*. 2015;23(1):7-16. doi:10.1038/mt.2014.154

46. Cronin T, Vandenberghe LH, Hantz P, et al. Efficient transduction and optogenetic stimulation of retinal bipolar cells by a synthetic adeno-

associated virus capsid and promoter. *EMBO Mol Med*. 2014;6(9):1175-1190. doi:10.15252/emmm.201404077

47. Protection IC on NIR. ICNIRP Guidelines on Limits of Exposure to Incoherent Visible and Infrared Radiation. *Health Phys*. 2013;105(1):74. doi:10.1097/HP.0b013e318289a611

48. Chaffiol A, Caplette R, Jaillard C, et al. A New Promoter Allows Optogenetic Vision Restoration with Enhanced Sensitivity in Macaque Retina. *Mol Ther J Am Soc Gene Ther*. 2017;25(11):2546-2560. doi:10.1016/j.ymthe.2017.07.011

49. Sengupta A, Chaffiol A, Macé E, et al. Red-shifted channelrhodopsin stimulation restores light responses in blind mice, macaque retina, and human retina. *EMBO Mol Med*. 2016;8(11):1248-1264. doi:10.15252/emmm.201505699

50. Lin JY, Knutsen PM, Muller A, Kleinfeld D, Tsien RY. ReaChR: a red-shifted variant of channelrhodopsin enables deep transcranial optogenetic excitation. *Nat Neurosci*. 2013;16(10):1499-1508. doi:10.1038/nn.3502

51. Klapoetke NC, Murata Y, Kim SS, et al. Independent optical excitation of distinct neural populations. *Nat Methods*. 2014;11(3):338-346. doi:10.1038/nmeth.2836

52. GenSight Biologics. *A Phase 1/2a, Open-Label, Non-Randomized, Dose-Escalation Study to Evaluate the Safety and Tolerability of GS030 in Subjects With Retinitis Pigmentosa*. clinicaltrials.gov; 2022. Accessed April 7, 2025. https://clinicaltrials.gov/study/NCT03326336

53. Simon CJ, Sahel JA, Duebel J, Herlitze S, Dalkara D. Opsins for vision restoration. *Biochem Biophys Res Commun*. 2020;527(2):325-330. doi:10.1016/j.bbrc.2019.12.117

54. Li ZY, Kljavin IJ, Milam AH. Rod photoreceptor neurite sprouting in retinitis pigmentosa. *J Neurosci Off J Soc Neurosci*. 1995;15(8):5429-5438. doi:10.1523/JNEUROSCI.15-08-05429.1995

55. Busskamp V, Duebel J, Balya D, et al. Genetic reactivation of cone photoreceptors restores visual responses in retinitis pigmentosa. *Science*. 2010;329(5990):413-417. doi:10.1126/science.1190897

56. Khabou H, Garita-Hernandez M, Chaffiol A, et al. Noninvasive gene delivery to foveal cones for vision restoration. *JCI Insight*. 2018;3(2):e96029, 96029. doi:10.1172/jci.insight.96029

57. van Wyk M, Pielecka-Fortuna J, Löwel S, Kleinlogel S. Restoring the ON Switch in Blind Retinas: Opto-mGluR6, a Next-Generation, Cell-Tailored

Optogenetic Tool. *PLoS Biol*. 2015;13(5):e1002143. doi:10.1371/journal.pbio.1002143

58. Yau KW, Hardie RC. Phototransduction motifs and variations. *Cell*. 2009;139(2):246-264. doi:10.1016/j.cell.2009.09.029

59. Terakita A. The opsins. *Genome Biol*. 2005;6(3):213. doi:10.1186/gb-2005-6-3-213

60. Morshedian A, Fain GL. The evolution of rod photoreceptors. *Philos Trans R Soc Lond B Biol Sci*. 2017;372(1717):20160074. doi:10.1098/rstb.2016.0074

61. Gaub BM, Berry MH, Holt AE, Isacoff EY, Flannery JG. Optogenetic Vision Restoration Using Rhodopsin for Enhanced Sensitivity. *Mol Ther J Am Soc Gene Ther*. 2015;23(10):1562-1571. doi:10.1038/mt.2015.121

62. Cehajic-Kapetanovic J, Eleftheriou C, Allen AE, et al. Restoration of Vision with Ectopic Expression of Human Rod Opsin. *Curr Biol CB*. 2015;25(16):2111-2122. doi:10.1016/j.cub.2015.07.029

63. Berry MH, Holt A, Salari A, et al. Restoration of high-sensitivity and adapting vision with a cone opsin. *Nat Commun*. 2019;10(1):1221. doi:10.1038/s41467-019-09124-x

64. Berry MH, Holt A, Broichhagen J, Donthamsetti P, Flannery JG, Isacoff EY. Photopharmacology for vision restoration. *Curr Opin Pharmacol*. 2022;65:102259. doi:10.1016/j.coph.2022.102259

65. Bipolar origin of synaptic inputs to sustained OFF-ganglion cells in the mudpuppy retina | Journal of Neurophysiology | American Physiological Society. Accessed April 10, 2025. https://journals.physiology.org/doi/abs/10.1152/jn.1988.60.3.1122

66. Nelson R, Kolb H, Freed MA. OFF-alpha and OFF-beta ganglion cells in cat retina. I: Intracellular electrophysiology and HRP stains. *J Comp Neurol*. 1993;329(1):68-84. doi:10.1002/cne.903290106

67. Kim US, Mahroo OA, Mollon JD, Yu-Wai-Man P. Retinal Ganglion Cells—Diversity of Cell Types and Clinical Relevance. *Front Neurol*. 2021;12. doi:10.3389/fneur.2021.661938

68. Reinhard K, Münch TA. Visual properties of human retinal ganglion cells. *PloS One*. 2021;16(2):e0246952. doi:10.1371/journal.pone.0246952

69. Caporale N, Kolstad KD, Lee T, et al. LiGluR restores visual responses in rodent models of inherited blindness. *Mol Ther J Am Soc Gene Ther*. 2011;19(7):1212-1219. doi:10.1038/mt.2011.103

70. Gaub BM, Berry MH, Holt AE, et al. Restoration of visual function by expression of a light-gated mammalian ion channel in retinal ganglion cells or ON-bipolar cells. *Proc Natl Acad Sci U S A*. 2014;111(51):E5574-5583. doi:10.1073/pnas.1414162111

71. Szymański W, Beierle JM, Kistemaker HAV, Velema WA, Feringa BL. Reversible Photocontrol of Biological Systems by the Incorporation of Molecular Photoswitches. *Chem Rev*. 2013;113(8):6114-6178. doi:10.1021/cr300179f

72. Volgraf M, Gorostiza P, Numano R, Kramer RH, Isacoff EY, Trauner D. Allosteric control of an ionotropic glutamate receptor with an optical switch. *Nat Chem Biol*. 2006;2(1):47-52. doi:10.1038/nchembio756

73. Jmjm R, H F, A T, Pmp G. Bioconjugation with Maleimides: A Useful Tool for Chemical Biology. *Chem Weinh Bergstr Ger*. 2019;25(1). doi:10.1002/chem.201803174

74. Gautier A, Juillerat A, Heinis C, et al. An Engineered Protein Tag for Multiprotein Labeling in Living Cells. *Chem Biol*. 2008;15(2):128-136. doi:10.1016/j.chembiol.2008.01.007

75. Sahel JA, Boulanger-Scemama E, Pagot C, et al. Partial recovery of visual function in a blind patient after optogenetic therapy. *Nat Med*. 2021;27(7):1223-1229. doi:10.1038/s41591-021-01351-4

76. Berry MH, Holt A, Levitz J, et al. Restoration of patterned vision with an engineered photoactivatable G protein-coupled receptor. *Nat Commun*. 2017;8(1):1862. doi:10.1038/s41467-017-01990-7

77. Yoo S, Mittelstein DR, Hurt RC, Lacroix J, Shapiro MG. Focused ultrasound excites cortical neurons via mechanosensitive calcium accumulation and ion channel amplification. *Nat Commun*. 2022;13(1):493. doi:10.1038/s41467-022-28040-1

78. Tsui PH, Wang SH, Huang CC. In vitro effects of ultrasound with different energies on the conduction properties of neural tissue. *Ultrasonics*. 2005;43(7):560-565. doi:10.1016/j.ultras.2004.12.003

79. Dalecki D. Mechanical bioeffects of ultrasound. *Annu Rev Biomed Eng*. 2004;6:229-248. doi:10.1146/annurev.bioeng.6.040803.140126

80. O'Brien WD. Ultrasound-biophysics mechanisms. *Prog Biophys Mol Biol*. 2007;93(1-3):212-255. doi:10.1016/j.pbiomolbio.2006.07.010

81. Fomenko A, Neudorfer C, Dallapiazza RF, Kalia SK, Lozano AM. Low-intensity ultrasound neuromodulation: An overview of mechanisms and

emerging human applications. *Brain Stimulat*. 2018;11(6):1209-1217. doi:10.1016/j.brs.2018.08.013

82. Menz MD, Ye P, Firouzi K, et al. Radiation Force as a Physical Mechanism for Ultrasonic Neurostimulation of the Ex Vivo Retina. *J Neurosci Off J Soc Neurosci*. 2019;39(32):6251-6264. doi:10.1523/JNEUROSCI.2394-18.2019

83. Qian X, Lu G, Thomas BB, et al. Noninvasive Ultrasound Retinal Stimulation for Vision Restoration at High Spatiotemporal Resolution. *BME Front*. 2022;2022:9829316. doi:10.34133/2022/9829316

84. Naor O, Hertzberg Y, Zemel E, Kimmel E, Shoham S. Towards multifocal ultrasonic neural stimulation II: design considerations for an acoustic retinal prosthesis. *J Neural Eng*. 2012;9(2):026006. doi:10.1088/1741-2560/9/2/026006

85. RetNet - Retinal Information Network. Accessed April 12, 2025. https://retnet.org/

86. Bainbridge JWB, Smith AJ, Barker SS, et al. Effect of Gene Therapy on Visual Function in Leber's Congenital Amaurosis. *N Engl J Med*. 2008;358(21):2231-2239. doi:10.1056/NEJMoa0802268

87. Hauswirth WW, Aleman TS, Kaushal S, et al. Treatment of leber congenital amaurosis due to RPE65 mutations by ocular subretinal injection of adeno-associated virus gene vector: short-term results of a phase I trial. *Hum Gene Ther*. 2008;19(10):979-990. doi:10.1089/hum.2008.107

88. Maguire AM, Simonelli F, Pierce EA, et al. Safety and Efficacy of Gene Transfer for Leber's Congenital Amaurosis. *N Engl J Med*. 2008;358(21):2240-2248. doi:10.1056/NEJMoa0802315

89. Russell S, Bennett J, Wellman JA, et al. Efficacy and safety of voretigene neparvovec (AAV2-hRPE65v2) in patients with RPE65-mediated inherited retinal dystrophy: a randomised, controlled, open-label, phase 3 trial. *Lancet Lond Engl*. 2017;390(10097):849-860. doi:10.1016/S0140-6736(17)31868-8

90. Carvalho LS, Xu J, Pearson RA, et al. Long-term and age-dependent restoration of visual function in a mouse model of CNGB3-associated achromatopsia following gene therapy. *Hum Mol Genet*. 2011;20(16):3161-3175. doi:10.1093/hmg/ddr218

91. Fischer MD, McClements ME, Martinez-Fernandez de la Camara C, et al. Codon-Optimized RPGR Improves Stability and Efficacy of AAV8 Gene Therapy in Two Mouse Models of X-Linked Retinitis Pigmentosa. *Mol Ther J Am Soc Gene Ther*. 2017;25(8):1854-1865. doi:10.1016/j.ymthe.2017.05.005

92. Pawlyk BS, Bulgakov OV, Sun X, et al. Photoreceptor rescue by an abbreviated human RPGR gene in a murine model of X-linked retinitis pigmentosa. *Gene Ther*. 2016;23(2):196-204. doi:10.1038/gt.2015.93

93. Acland GM, Aguirre GD, Ray J, et al. Gene therapy restores vision in a canine model of childhood blindness. *Nat Genet*. 2001;28(1):92-95. doi:10.1038/ng0501-92

94. Beltran WA, Cideciyan AV, Lewin AS, et al. Gene therapy rescues photoreceptor blindness in dogs and paves the way for treating human X-linked retinitis pigmentosa. *Proc Natl Acad Sci U S A*. 2012;109(6):2132-2137. doi:10.1073/pnas.1118847109

95. Kleinlogel S, Vogl C, Jeschke M, Neef J, Moser T. Emerging Approaches for Restoration of Hearing and Vision. *Physiol Rev*. 2020;100(4):1467-1525. doi:10.1152/physrev.00035.2019

96. Eom K, Kim J, Choi JM, et al. Enhanced infrared neural stimulation using localized surface plasmon resonance of gold nanorods. *Small Weinh Bergstr Ger*. 2014;10(19):3853-3857. doi:10.1002/smll.201400599

97. Wells J, Kao C, Mariappan K, et al. Optical stimulation of neural tissue in vivo. *Opt Lett*. 2005;30(5):504-506. doi:10.1364/ol.30.000504

98. Wells J, Konrad P, Kao C, Jansen ED, Mahadevan-Jansen A. Pulsed laser versus electrical energy for peripheral nerve stimulation. *J Neurosci Methods*. 2007;163(2):326-337. doi:10.1016/j.jneumeth.2007.03.016

99. Izzo AD, Suh E, Pathria J, Walsh JT, Whitlon DS, Richter CP. Selectivity of neural stimulation in the auditory system: a comparison of optic and electric stimuli. *J Biomed Opt*. 2007;12(2):021008. doi:10.1117/1.2714296

100. Richter CP, Bayon R, Izzo AD, et al. Optical stimulation of auditory neurons: effects of acute and chronic deafening. *Hear Res*. 2008;242(1-2):42-51. doi:10.1016/j.heares.2008.01.011

101. Shapiro MG, Homma K, Villarreal S, Richter CP, Bezanilla F. Infrared light excites cells by changing their electrical capacitance. *Nat Commun*. 2012;3(1):736. doi:10.1038/ncomms1742

102. Richter CP, Matic AI, Wells JD, Jansen ED, Walsh JT. Neural stimulation with optical radiation. *Laser Photonics Rev*. 2011;5(1):68-80. doi:10.1002/lpor.200900044

103. Wells J, Kao C, Konrad P, et al. Biophysical mechanisms of transient optical stimulation of peripheral nerve. *Biophys J*. 2007;93(7):2567-2580. doi:10.1529/biophysj.107.104786

104. Katz EJ, Ilev IK, Krauthamer V, Kim DH, Weinreich D. Excitation of primary afferent neurons by near-infrared light in vitro. *Neuroreport*. 2010;21(9):662-666. doi:10.1097/WNR.0b013e32833add3a

105. Hutter E, Fendler JH. Exploitation of Localized Surface Plasmon Resonance. *Adv Mater*. 2004;16(19):1685-1706. doi:10.1002/adma.200400271

106. Stewart ME, Anderton CR, Thompson LB, et al. Nanostructured plasmonic sensors. *Chem Rev*. 2008;108(2):494-521. doi:10.1021/cr068126n

107. Baffou G, Quidant R. Thermo-plasmonics: using metallic nanostructures as nano-sources of heat. *Laser Photonics Rev*. 2013;7(2):171-187. doi:10.1002/lpor.201200003

108. Paviolo C, Haycock JW, Cadusch PJ, McArthur SL, Stoddart PR. Laser exposure of gold nanorods can induce intracellular calcium transients. *J Biophotonics*. 2014;7(10):761-765. doi:10.1002/jbio.201300043

109. Eom K, Im C, Hwang S, et al. Synergistic combination of near-infrared irradiation and targeted gold nanoheaters for enhanced photothermal neural stimulation. *Biomed Opt Express*. 2016;7(4):1614-1625. doi:10.1364/BOE.7.001614

110. Carvalho-de-Souza JL, Treger JS, Dang B, Kent SBH, Pepperberg DR, Bezanilla F. Photosensitivity of neurons enabled by cell-targeted gold nanoparticles. *Neuron*. 2015;86(1):207-217. doi:10.1016/j.neuron.2015.02.033

111. Eom K, Hwang S, Yun S, Byun KM, Jun SB, Kim SJ. Photothermal activation of astrocyte cells using localized surface plasmon resonance of gold nanorods. *J Biophotonics*. 2017;10(4):486-493. doi:10.1002/jbio.201600280

112. Nakatsuji H, Numata T, Morone N, et al. Thermosensitive Ion Channel Activation in Single Neuronal Cells by Using Surface-Engineered Plasmonic Nanoparticles. *Angew Chem Int Ed Engl*. 2015;54(40):11725-11729. doi:10.1002/anie.201505534

113. Caterina MJ. Transient receptor potential ion channels as participants in thermosensation and thermoregulation. *Am J Physiol Regul Integr Comp Physiol*. 2007;292(1):R64-76. doi:10.1152/ajpregu.00446.2006

114. Albert ES, Bec JM, Desmadryl G, et al. TRPV4 channels mediate the infrared laser-evoked response in sensory neurons. *J Neurophysiol*. 2012;107(12):3227-3234. doi:10.1152/jn.00424.2011

115. Watanabe H, Vriens J, Suh SH, Benham CD, Droogmans G, Nilius B. Heat-evoked activation of TRPV4 channels in a HEK293 cell expression system and in native mouse aorta endothelial cells. *J Biol Chem*. 2002;277(49):47044-47051. doi:10.1074/jbc.M208277200

116. Güler AD, Lee H, Iida T, Shimizu I, Tominaga M, Caterina M. Heat-evoked activation of the ion channel, TRPV4. *J Neurosci Off J Soc Neurosci*. 2002;22(15):6408-6414. doi:10.1523/JNEUROSCI.22-15-06408.2002

117. Nie J, Eom K, AlGhosain HM, et al. Intravitreally Injected Plasmonic Nanorods Activate Bipolar Cells with Patterned Near-Infrared Laser Projection. *ACS Nano*. 2025;19(12):11823-11840. doi:10.1021/acsnano.4c14061

118. Peynshaert K, Devoldere J, De Smedt SC, Remaut K. In vitro and ex vivo models to study drug delivery barriers in the posterior segment of the eye. *Adv Drug Deliv Rev*. 2018;126:44-57. doi:10.1016/j.addr.2017.09.007

119. Le Goff MM, Bishop PN. Adult vitreous structure and postnatal changes. *Eye*. 2008;22(10):1214-1222. doi:10.1038/eye.2008.21

120. Peynshaert K, Devoldere J, Forster V, et al. Toward smart design of retinal drug carriers: a novel bovine retinal explant model to study the barrier role of the vitreoretinal interface. *Drug Deliv*. 24(1):1384-1394. doi:10.1080/10717544.2017.1375578

121. Ochakovski GA, Bartz-Schmidt KU, Fischer MD. Retinal Gene Therapy: Surgical Vector Delivery in the Translation to Clinical Trials. *Front Neurosci*. 2017;11. doi:10.3389/fnins.2017.00174

122. Junnuthula V, Sadeghi Boroujeni A, Cao S, et al. Intravitreal Polymeric Nanocarriers with Long Ocular Retention and Targeted Delivery to the Retina and Optic Nerve Head Region. *Pharmaceutics*. 2021;13(4):445. doi:10.3390/pharmaceutics13040445

123. Elbedwehy AM, Wu J, Na HK, et al. ROS-responsive charge reversal mesoporous silica nanoparticles as promising drug delivery system for neovascular retinal diseases. *J Controlled Release*. 2024;373:224-239. doi:10.1016/j.jconrel.2024.07.022

124. Ottonelli I, Bighinati A, Adani E, et al. Optimization of an Injectable Hydrogel Depot System for the Controlled Release of Retinal-Targeted Hybrid Nanoparticles. *Pharmaceutics*. 2023;15(1):25. doi:10.3390/pharmaceutics15010025

125. Gabriele Sandrian M, Wollstein G, Schuman JS, et al. Inflammatory response to intravitreal injection of gold nanorods. *Br J Ophthalmol*. 2012;96(12):1522-1529. doi:10.1136/bjophthalmol-2012-301904

126. Roh YJ, Rho CR, Cho WK, Kang S. The Antiangiogenic Effects of Gold Nanoparticles on Experimental Choroidal Neovascularization in Mice. *Invest Ophthalmol Vis Sci*. 2016;57(15):6561-6567. doi:10.1167/iovs.16-19754

127. Kim JH, Kim MH, Jo DH, Yu YS, Lee TG, Kim JH. The inhibition of retinal neovascularization by gold nanoparticles via suppression of VEGFR-2 activation. *Biomaterials*. 2011;32(7):1865-1871. doi:10.1016/j.biomaterials.2010.11.030

128. Batabyal S, Gajjeraman S, Bhattacharya S, Wright W, Mohanty S. Nano-enhanced optical gene delivery to retinal degenerated mice. *Curr Gene Ther*. 2019;19(5):318-329. doi:10.2174/1566523219666191017114044

129. Wilson AM, Mazzaferri J, Bergeron É, et al. In Vivo Laser-Mediated Retinal Ganglion Cell Optoporation Using KV1.1 Conjugated Gold Nanoparticles. *Nano Lett*. 2018;18(11):6981-6988. doi:10.1021/acs.nanolett.8b02896

130. Song HB, Wi JS, Jo DH, et al. Intraocular application of gold nanodisks optically tuned for optical coherence tomography: inhibitory effect on retinal neovascularization without unbearable toxicity. *Nanomedicine Nanotechnol Biol Med*. 2017;13(6):1901-1911. doi:10.1016/j.nano.2017.03.016

131. Edelhauser HF, Rowe-Rendleman CL, Robinson MR, et al. Ophthalmic Drug Delivery Systems for the Treatment of Retinal Diseases: Basic Research to Clinical Applications. *Invest Ophthalmol Vis Sci*. 2010;51(11):5403-5420. doi:10.1167/iovs.10-5392

132. Sakurai E, Ozeki H, Kunou N, Ogura Y. Effect of Particle Size of Polymeric Nanospheres on Intravitreal Kinetics. *Ophthalmic Res*. 2000;33(1):31-36. doi:10.1159/000055638

133. Raju HB, Hu Y, Padgett KR, Rodriguez JE, Goldberg JL. Investigation of nanoparticles using magnetic resonance imaging after intravitreal injection. *Clin Experiment Ophthalmol*. 2012;40(1):100-107. doi:10.1111/j.1442-9071.2011.02651.x

134. Koo H, Moon H, Han H, et al. The movement of self-assembled amphiphilic polymeric nanoparticles in the vitreous and retina after intravitreal injection. *Biomaterials*. 2012;33(12):3485-3493. doi:10.1016/j.biomaterials.2012.01.030

135. Cehajic-Kapetanovic J, Milosavljevic N, Bedford RA, Lucas RJ, Bishop PN. Efficacy and Safety of Glycosidic Enzymes for Improved Gene Delivery to the Retina following Intravitreal Injection in Mice. *Mol Ther Methods Clin Dev*. 2018;9:192-202. doi:10.1016/j.omtm.2017.12.002

136. Barnstable CJ, Dräger UC. Thy-1 antigen: a ganglion cell specific marker in rodent retina. *Neuroscience*. 1984;11(4):847-855. doi:10.1016/0306-4522(84)90195-7

137. Beale R, Osborne NN. Localization of the Thy-1 antigen to the surfaces of rat retinal ganglion cells. *Neurochem Int*. 1982;4(6):587-595. doi:10.1016/0197-0186(82)90049-3

138. Hombrebueno JR, Luo C, Guo L, Chen M, Xu H. Intravitreal Injection of Normal Saline Induces Retinal Degeneration in the C57BL/6J Mouse. *Transl Vis Sci Technol*. 2014;3(2):3. doi:10.1167/tvst.3.2.3

139. Da Costa R, Röger C, Segelken J, Barben M, Grimm C, Neidhardt J. A Novel Method Combining Vitreous Aspiration and Intravitreal AAV2/8 Injection Results in Retina-Wide Transduction in Adult Mice. *Invest Ophthalmol Vis Sci*. 2016;57(13):5326-5334. doi:10.1167/iovs.16-19701

140. Zhou G, Williams RW. Mouse models for the analysis of myopia: an analysis of variation in eye size of adult mice. *Optom Vis Sci Off Publ Am Acad Optom*. 1999;76(6):408-418. doi:10.1097/00006324-199906000-00021

141. Olesiak-Banska J, Waszkielewicz M, Obstarczyk P, Samoc M. Two-photon absorption and photoluminescence of colloidal gold nanoparticles and nanoclusters. *Chem Soc Rev*. 2019;48(15):4087-4117. doi:10.1039/C8CS00849C

142. Denk W, Strickler JH, Webb WW. Two-photon laser scanning fluorescence microscopy. *Science*. 1990;248(4951):73-76. doi:10.1126/science.2321027

143. Sheik-Bahae M, Said AA, Wei TH, Hagan DJ, Van Stryland EW. Sensitive measurement of optical nonlinearities using a single beam. *IEEE J Quantum Electron*. 1990;26(4):760-769. doi:10.1109/3.53394

144. Wang H, Huff TB, Zweifel DA, et al. In vitro and in vivo two-photon luminescence imaging of single gold nanorods. *Proc Natl Acad Sci*. 2005;102(44):15752-15756. doi:10.1073/pnas.0504892102

145. Li JL, Gu M. Surface plasmonic gold nanorods for enhanced two-photon microscopic imaging and apoptosis induction of cancer cells. *Biomaterials*. 2010;31(36):9492-9498. doi:10.1016/j.biomaterials.2010.08.068

146. Naso MF, Tomkowicz B, Perry WL, Strohl WR. Adeno-Associated Virus (AAV) as a Vector for Gene Therapy. *Biodrugs*. 2017;31(4):317-334. doi:10.1007/s40259-017-0234-5

147. Goldenberg DT, Giblin FJ, Cheng M, et al. Posterior vitreous detachment with microplasmin alters the retinal penetration of intravitreal bevacizumab

(Avastin) in rabbit eyes. *Retina Phila Pa*. 2011;31(2):393-400. doi:10.1097/IAE.0b013e3181e586b2

148. Hisatomi T, Tachibana T, Notomi S, et al. INCOMPLETE REPAIR OF RETINAL STRUCTURE AFTER VITRECTOMY WITH INTERNAL LIMITING MEMBRANE PEELING. *Retina Phila Pa*. 2017;37(8):1523-1528. doi:10.1097/IAE.0000000000001388

149. Young RW. The renewal of photoreceptor cell outer segments. *J Cell Biol*. 1967;33(1):61-72. doi:10.1083/jcb.33.1.61

150. Bairati A, Orzalesi N. THE ULTRASTRUCTURE OF THE PIGMENT EPITHELIUM AND OF THE PHOTORECEPTOR-PIGMENT EPITHELIUM JUNCTION IN THE HUMAN RETINA. *J Ultrastruct Res*. 1963;41:484-496. doi:10.1016/s0022-5320(63)80080-5

151. Hanna C, Bicknell DS, O'brien JE. Cell turnover in the adult human eye. *Arch Ophthalmol Chic Ill 1960*. 1961;65:695-698. doi:10.1001/archopht.1961.01840020697016

152. Bonnin EA, Fornasiero EF, Lange F, Turck CW, Rizzoli SO. NanoSIMS observations of mouse retinal cells reveal strict metabolic controls on nitrogen turnover. *BMC Mol Cell Biol*. 2021;22(1):5. doi:10.1186/s12860-020-00339-1

153. Neufeld AH, Gachie EN. The inherent, age-dependent loss of retinal ganglion cells is related to the lifespan of the species. *Neurobiol Aging*. 2003;24(1):167-172. doi:10.1016/s0197-4580(02)00059-3

154. Steinman RM, Hawiger D, Nussenzweig MC. Tolerogenic Dendritic Cells*. *Annu Rev Immunol*. 2003;21(Volume 21, 2003):685-711. doi:10.1146/annurev.immunol.21.120601.141040

155. Macpherson AJ, Lamarre A. BLySsful interactions between DCs and B cells. *Nat Immunol*. 2002;3(9):798-800. doi:10.1038/ni0902-798

156. MacLennan I, Vinuesa C. Dendritic cells, BAFF, and APRIL: innate players in adaptive antibody responses. *Immunity*. 2002;17(3):235-238. doi:10.1016/s1074-7613(02)00398-9

157. Bergtold A, Desai DD, Gavhane A, Clynes R. Cell Surface Recycling of Internalized Antigen Permits Dendritic Cell Priming of B Cells. *Immunity*. 2005;23(5):503-514. doi:10.1016/j.immuni.2005.09.013

158. Elliott AD. Confocal Microscopy: Principles and Modern Practices. *Curr Protoc Cytom*. 2020;92(1):e68. doi:10.1002/cpcy.68

159. Perry VH, Morris RJ, Raisman G. Is Thy-1 expressed only by ganglion cells and their axons in the retina and optic nerve? *J Neurocytol*. 1984;13(5):809-824. doi:10.1007/BF01148495

160. Kim JH, Kim JH, Kim KW, Kim MH, Yu YS. Intravenously administered gold nanoparticles pass through the blood-retinal barrier depending on the particle size, and induce no retinal toxicity. *Nanotechnology*. 2009;20(50):505101. doi:10.1088/0957-4484/20/50/505101

161. Zhang XD, Wu D, Shen X, et al. Size-dependent in vivo toxicity of PEG-coated gold nanoparticles. *Int J Nanomedicine*. 2011;6:2071-2081. doi:10.2147/IJN.S21657

162. Isoda K, Tanaka A, Fuzimori C, et al. Toxicity of Gold Nanoparticles in Mice due to Nanoparticle/Drug Interaction Induces Acute Kidney Damage. *Nanoscale Res Lett*. 2020;15:141. doi:10.1186/s11671-020-03371-4

163. Cho WS, Cho M, Jeong J, et al. Acute toxicity and pharmacokinetics of 13 nm-sized PEG-coated gold nanoparticles. *Toxicol Appl Pharmacol*. 2009;236(1):16-24. doi:10.1016/j.taap.2008.12.023

164. Simpson CA, Salleng KJ, Cliffel DE, Feldheim DL. In vivo toxicity, biodistribution, and clearance of glutathione-coated gold nanoparticles. *Nanomedicine Nanotechnol Biol Med*. 2013;9(2):257-263. doi:10.1016/j.nano.2012.06.002

165. Rambanapasi C, Zeevaart JR, Buntting H, et al. Bioaccumulation and Subchronic Toxicity of 14 nm Gold Nanoparticles in Rats. *Mol Basel Switz*. 2016;21(6):763. doi:10.3390/molecules21060763

166. Bakri SJ, Pulido JS, Mukherjee P, Marler RJ, Mukhopadhyay D. Absence of histologic retinal toxicity of intravitreal nanogold in a rabbit model. *Retina Phila Pa*. 2008;28(1):147-149. doi:10.1097/IAE.0b013e3180dc9360

167. 14:00-17:00. ISO 10993-11:2017. ISO. Accessed February 1, 2024. https://www.iso.org/standard/68426.html

168. Research C for DE and. Drug Products, Including Biological Products, that Contain Nanomaterials - Guidance for Industry. April 21, 2022. Accessed May 27, 2025. https://www.fda.gov/regulatory-information/search-fda-guidance-documents/drug-products-including-biological-products-contain-nanomaterials-guidance-industry

169. Zhou X, Hansson GK. Effect of sex and age on serum biochemical reference ranges in C57BL/6J mice. *Comp Med*. 2004;54(2):176-178.

170. Mazzaccara C, Labruna G, Cito G, et al. Age-Related Reference Intervals of the Main Biochemical and Hematological Parameters in C57BL/6J,

129SV/EV and C3H/HeJ Mouse Strains. *PloS One*. 2008;3(11):e3772. doi:10.1371/journal.pone.0003772

171. Duong L, Pixley FJ, Nelson DJ, Jackaman C. Aging Leads to Increased Monocytes and Macrophages With Altered CSF-1 Receptor Expression and Earlier Tumor-Associated Macrophage Expansion in Murine Mesothelioma. *Front Aging*. 2022;3:848925. doi:10.3389/fragi.2022.848925

172. Chen YS, Hung YC, Liau I, Huang GS. Assessment of the In Vivo Toxicity of Gold Nanoparticles. *Nanoscale Res Lett*. 2009;4(8):858-864. doi:10.1007/s11671-009-9334-6

173. Chen H, Dorrigan A, Saad S, Hare DJ, Cortie MB, Valenzuela SM. In vivo study of spherical gold nanoparticles: inflammatory effects and distribution in mice. *PloS One*. 2013;8(2):e58208. doi:10.1371/journal.pone.0058208

174. Shi C, Pamer EG. Monocyte recruitment during infection and inflammation. *Nat Rev Immunol*. 2011;11(11):762-774. doi:10.1038/nri3070

175. Cho WS, Cho M, Jeong J, et al. Acute toxicity and pharmacokinetics of 13 nm-sized PEG-coated gold nanoparticles. *Toxicol Appl Pharmacol*. 2009;236(1):16-24. doi:10.1016/j.taap.2008.12.023

176. Lasagna-Reeves C, Gonzalez-Romero D, Barria MA, et al. Bioaccumulation and toxicity of gold nanoparticles after repeated administration in mice. *Biochem Biophys Res Commun*. 2010;393(4):649-655. doi:10.1016/j.bbrc.2010.02.046

177. Chernoff N, Hill D, Lang J, et al. The Comparative Toxicity of 10 Microcystin Congeners Administered Orally to Mice: Clinical Effects and Organ Toxicity. *Toxins*. 2020;12(6):403. doi:10.3390/toxins12060403

178. Heydrnejad MS, Samani RJ, Aghaeivanda S. Toxic Effects of Silver Nanoparticles on Liver and Some Hematological Parameters in Male and Female Mice (Mus musculus). *Biol Trace Elem Res*. 2015;165(2):153-158. doi:10.1007/s12011-015-0247-1

179. Chithrani BD, Ghazani AA, Chan WCW. Determining the size and shape dependence of gold nanoparticle uptake into mammalian cells. *Nano Lett*. 2006;6(4):662-668. doi:10.1021/nl052396o

180. Cheung KL, Chen H, Chen Q, et al. CTAB-coated gold nanorods elicit allergic response through degranulation and cell death in human basophils. *Nanoscale*. 2012;4(15):4447-4449. doi:10.1039/c2nr30435j

181. Chen J, Wang H, Long W, et al. Sex differences in the toxicity of polyethylene glycol-coated gold nanoparticles in mice. *Int J Nanomedicine*. 2013;8:2409. doi:10.2147/IJN.S46376